CHARACTERIZATION OF ULTRAWIDEBAND PROPAGATION IN AIRCRAFT AND OUTDOOR INDUSTRIAL ENVIRONMENTS

by

SIMON CHIU

B.A.Sc., University of British Columbia, 2006

A THESIS SUBMITTED IN PARTIAL FULFILLMENT OF
THE REQUIREMENTS FOR THE DEGREE OF

MASTER OF APPLIED SCIENCE

in

The Faculty of Graduate Studies

(Electrical and Computer Engineering)

THE UNIVERSITY OF BRITISH COLUMBIA

(Vancouver)

April 2009

Abstract

The channel modeling committees of the IEEE 802.15.3a and 802.15.4a task groups devoted considerable effort to developing ultrawideband (UWB) wireless channel models applicable to systems that operate between 3.1 and 10.6 GHz under both line-of-sight (LOS) and non-line-of-sight (NLOS) conditions in residential, office, outdoor, industrial and body-centric environments at ranges up to 15 m. However, there has been increasing demand for deploying wireless systems in other unconventional environments that have not yet been well characterized. In this thesis, we present four major contributions concerning two such environments: the passenger cabin of a typical midsize airliner and outdoor industrial. First, we have characterized UWB path gain and time dispersion over the range 3.1-10.6 GHz within the empty passenger cabin of a Boeing 737-200 aircraft based on several hundred measured complex channel frequency responses (CFRs). We found that: (1) the coverage pattern takes the form of chevron-shaped contours with path gain decreasing least rapidly along the aisle seats and most rapidly along the window seats, and (2) there is significant advantage to using higher portions of the UWB band for short-range applications and reserving lower portions of the band for longer range applications in such environments. Second, we have characterized the shape of the UWB channel impulse response (CIR) and the fading statistics experienced by individual multipath components (MPCs) over the range 3.1-10.6 GHz within the Boeing 737-200 aircraft based upon 3300 measured CFRs. We have also modified the channel simulator developed by IEEE 802.15.4a to generate UWB CIRs that are representative of those that we observed within the cabin. Third, we have characterized the effect of human presence on path gain and time dispersion over the range 3.1-6.1 GHz within the passenger cabin of the Boeing 737-200 aircraft with and without volunteers in the passenger seats based on a few hundred measured CFRs. We found that human presence has substantially effects on RF propagation within the aircraft and that it should be considered when characterizing the performance of in-cabin wireless systems. Lastly, we present a range-extended VNA-based UWB channel sounder suitable for characterizing UWB propagation in outdoor industrial environments.

Table of Contents

List of Tables

List of Figures

List of Abbreviations

AoA	:	Angle-of-arrival
APDP	:	Averaged power delay profile
CDF	:	Cumulative distribution function
CIR	:	Channel impulse response
CFR	:	Channel frequency response
IFT	:	Inverse Fourier transform
LOS	:	Line-of-sight
MB-OFDM	:	Multiband orthogonal frequency division multiplexing
MPC	:	Multipath component
NLOS	:	Non-line-of-sight
PDP	:	Power delay profile
p-to-mp	:	Point-to-multipoint
p-to-p	:	Peer-to-peer
RMS	:	Root-mean-square
SV	:	Saleh-Valenzuela
UWB	:	Ultrawideband
VNA	:	Vector network analyzer

Acknowledgments

This work was supported by grants from Bell Canada (through its Bell University Laboratories R&D program), Nokia Canada, Omnex Controls Systems, and the Natural Sciences and Engineering Research Council of Canada.

I am grateful to the management and staff of the BCIT Aerospace Technology Campus at Vancouver International Airport for providing our research group with access to their Boeing 737-200 aircraft (a donation from the WestJet Airlines) during the course of this study. I owe particular thanks to Jack Baryluk, Grant Johnson and Lusia Kurk.

I would like to thank my colleagues James Chuang, Sunny Xin, Weiwen Liu and Anthony Liu, Claire Chuang, Wadah Muneer and Arghavan Emami for their support during my Master program.

I would like to thank Robert White, Shahzad Bashir, Ivan Chan, Alex Lee, Chris Pang, Cecilia Yeung, and Chad Woodworth for their considerable assistance during the data collection phase of this study. I would also like to thank Faye Limbo and Johnty Wang for their efforts in gathering volunteers.

I would like to thank my parents, siblings and all of my friends for their continuing love and support. I would also like to thank my lovely girlfriend, Cherry Wu, for everything.

Lastly, I would like to thank Dr. Michelson for his guidance, suggestions and patience over the past years.

Co-Authorship Statement

A version of Chapters 2, 3 and 4 in this thesis has already been or will be submitted to IEEE transactions for publication,

[1] S. Chiu, J. Chuang and D. G. Michelson, "UWB radiowave propagation within the passenger cabin of a Boeing 737-200 aircraft."

[2] S. Chiu, J. Chuang and D. G. Michelson, "Characterization of UWB channel impulse responses within the passenger cabin of a Boeing 737-200 aircraft."

[3] S. Chiu and D. G. Michelson, "Effects of human presence on UWB radiowave propagation within the passenger cabin of a midsize airliner."

[4] S. Chiu and D. G. Michelson, "A range-extended UWB channel sounder for characterizing outdoor industrial environments."

In the first and second manuscripts, Mr. Chuang contributed greatly to the data collection and data analysis of the preliminary data during the early stages. He also provided useful suggestions and insights in the later phases of the two projects.

All the projects above were identified and initiated by Dr. Michelson. In all of the projects, Dr. Michelson was either in charge of or took part in: (1) acquiring access to the Boeing 737-200 aircraft of British Columbia Institute of Technology, (2) recruiting volunteers to facilitate data collection, (3) planning of the measurement campaigns aboard the passenger cabin of the Boeing 737-200 aircraft, and (4) organizing, writing and editing of the manuscripts.

Chapter 1
Introduction

Since the pioneering efforts of the channel modeling committees of the IEEE 802.15.3a and 802.15.4a task groups, researchers have devoted considerable effort to developing ultrawideband (UWB) wireless channel models applicable to systems that operate between 3.1 and 10.6 GHz under both line-of-sight (LOS) and non-line-of-sight (NLOS) conditions in residential, office, outdoor, industrial and body-centric environments at ranges up to 15 m [1]-[3]. The propagation channel must be accurately modeled as the results affect coverage, reliability, and the manner in which UWB systems are deployed, and many important design issues, including: (1) selection of the number and placement of the fingers in rake receivers used to implement temporal diversity in spread spectrum systems, and (2) the selection of the guard-time and the design of cyclic prefixes used to mitigate multipath fading in Multiband Orthogonal Frequency Division Multiplexing (MB-OFDM) systems. Because unclustered CIR models tend to overestimate link capacity if the MPCs are indeed clustered, it is useful to determine the extent to which clustering occurs [4]. The shape of the CIR also affects the performance of UWB ranging and positioning algorithms because it determines how well the algorithm will be able to detect the first arriving MPC. As UWB-based wireless systems are increasingly proposed for use in more extreme environments, channel models that accurately describe the propagation channel of these environments must be proposed. In this thesis, we have considered the characterization of UWB propagation within both the passenger cabin of a typical mid-size airliner and typical outdoor industrial environments.

On February 14, 2002, a Report and Order by United States' Federal Communications Commission (FCC) allowed the unlicensed transmission of UWB signals in the range 3.1-10.6 GHz if certain power restrictions are fulfilled. Since then, interest from the industry and academia regarding UWB transmission has heightened. Two major non-profit industrial alliances, WiMedia Alliance and UWB Forum, were formed in support of the two major UWB schemes, MB-OFDM and direct sequence

spread spectrum (DS-SS). Two dedicated task groups, IEEE 802.15.3a and IEEE 802.15.4a, were also formed to regulate the PHY layer designs as well as the development of a standardized channel model that can be used as a fair comparison of different proposals in the future [5].

In recent years, there has been considerable interest in deploying personal wireless communications technology aboard passenger aircraft. The European Union's WirelessCabin project provided important guidance concerning the provisioning and delivery of in-cabin wireless services using conventional wireless technologies with satellite-based backhaul [6],[7]. Other past work has included: (1) systems engineering studies and field trials involving conventional wireless technologies such as cellular telephones, wireless LAN and Bluetooth wireless technology [8]-[10], (2) software-based simulation of wireless propagation within aircraft interiors [11][13], and (3) direct measurement of the channel response within aircraft interiors, *e.g.*, [14]-[18]. For airlines, UWB wireless technology operating within the frequency band between 3.1 and 10.6 GHz holds great promise for: (1) enabling deployment of high data rate (up to 480 Mbps) in-flight entertainment (IFE) and network access services within aircraft passenger cabins (over ranges of up to 10 m) using WiMedia UWB or similar technology and (2) facilitating operations and maintenance through deployment of sensor networks and precise positioning systems using ZigBee UWB or similar technology. However, with its confined volume, cylindrical structure, and high density of occupancy, the passenger cabin of a jet aircraft is fundamentally different from those environments considered previously.

In outdoor industrial environments, wireless devices are increasingly used for preventive maintenance, Supervisory Control and Data Acquisition (SCADA), Real-Time Control (RTC), dispatch, asset tracking and inventory control to increase productivity, avoid damage to machinery and prevent injury to personnel [23]-[25]. A few examples of outdoor industrial environments include train yards, construction sites, seaports, oil refineries, utility plants, chemical plants, *etc.* At the time of this writing, outdoor UWB communications is limited to the usage between mobile devices in the 3.1-10.6 GHz range [2]. Provided that regulatory issues can be dealt with, UWB wireless technology will be of particular interest for future systems in outdoor industrial

environments for the aforementioned applications. As described in [26], one of the most promising applications for UWB is sensor networks. In such applications, the data rates are typically less than 1 Mbit/s and the good ranging and geolocation capabilities of UWB are especially useful [3].

This remainder of this thesis is organized as follows. In Chapter 2, we collected several hundred UWB CFRs over the range 3.1-10.6 GHz with the transmitting and receiving antennas at various locations within the passenger cabin of a Boeing 737-200 aircraft. In reducing the measurement data, we have sought: (1) to characterize the distance and frequency dependence and the location variability of path gain in order to better understand the factors that affect coverage and reliability, (2) to characterize time dispersion within the aircraft, including the rms delay spread and the number of significant paths above a given threshold, in order to better understand the nature of the propagation environment, and (3) to consider the implications of our results for the deployment and testing of UWB wireless systems in aircraft passenger cabins.

In Chapter 3, we characterize the shape and structure of the UWB CIR, and the fading statistics and correlation properties of individual MPCs within the passenger cabin with the intent of developing a UWB CIR simulation model useful in analysis and design. Our results are based upon over 3300 CFRs that we measured over the range 3.1-10.6 GHz aboard a Boeing 737-200 aircraft with an omnidirectional transmitting antenna mounted near the cabin ceiling and an omnidirectional receiving antenna mounted at selected locations throughout the cabin. So that we could assess the spatial statistics of the UWB CIR, *i.e.*, the spatial average and the spatial correlation, we collected the CIRs across a 300-mm-by-300-mm spatial sampling grid with 50-mm spacing.

In Chapter 4, we present a more complete description of the effect of human presence on wireless propagation in aircraft passenger cabins than those presented in [19]-[21]. We collected a few hundred UWB CFRs over the frequency range of 3.1-6.1 GHz with the transmitting antenna mounted at either the cabin ceiling or headrest level along the centerline of the forward part of the cabin and the receiving antenna at the headrest or armrest level at selected locations throughout the cabin with three degrees of occupancy: empty, partially filled and completely filled. We then determined the manner in which human presence affects the distance and frequency dependence of path gain, the form of

the channel impulse response, the distance and frequency dependence of rms delay spread, and the number of significant paths below a given threshold within the passenger cabin of a typical mid-size airliner. We selected the frequency range 3.1-6.1 GHz, which corresponds closely to Band Groups 1 and 2 as defined by the WiMedia Alliance, because it is more likely that the lower portion of the UWB band will be used for point-to-multipoint coverage over large portions of the aircraft passenger cabin while the higher portions of the band are used to implement short-range peer-to-peer links [22].

In Chapter 5, we describe a range-extended VNA-based UWB channel sounder suitable for the characterization of UWB radiowave propagation over the range of 3.1-6.1 GHz in outdoor industrial environments. We also describe the proposed setup for data collection and methods for data reduction. For the same reason as for the human presence work, we selected the frequency range 3.1-6.1 GHz because it corresponds closely with Band Groups 1 and 2 as defined by the WiMedia Alliance. Also, attenuation is lower at lower frequencies and thus it is more likely that the lower portion of the UWB band will be used for coverage over longer distances.

Finally, in Chapter 6, we summarize our key findings and their implications, assess the limitations of the present work and offer recommendations for future work.

1.1 References

[1] A. F. Molisch, J. R. Foerster and M. Pendergrass, "Channel models for ultrawideband personal area networks," *IEEE Wireless Commun.*, vol. 10, no. 6, pp. 14-21, Dec. 2003.

[2] A. F. Molisch, "Ultrawideband propagation channels: Theory, measurement, and modeling", *IEEE Trans. Veh. Technol.*, vol. 54, no.5, pp. 1528–1545, Sep. 2005.

[3] A. F. Molisch et al., "A comprehensive standardized model for ultrawideband propagation channels," *IEEE Trans. Antennas Propag.*, vol. 54, no. 11, pp. 3151-3165, Nov. 2006.

[4] C. C. Chong and S. K. Yong, "A generic statistical-based UWB channel model for high-rise apartments," *IEEE Trans. Antennas Propag.*, vol. 53, no. 8, pp. 2389-2399, Aug. 2005.

[5] A. F. Molisch *et al.*, "IEEE 802.15.4a channel model – final report," IEEE 802.15-04-0662-00-004a, Nov. 2004.

[6] N. R. Diaz and M. Holzbock, "Aircraft cabin propagation for multimedia communications," in *Proc. EMPS 2002*, 25-26 Sep. 2002, pp. 281-288.

[7] A. Jahn *et al.*, "Evolution of aeronautical communications for personal and multimedia services," *IEEE Commun. Mag.*, vol. 41, no. 7, pp. 36-43, Jul. 2003.

[8] C. P. Niebla, "Topology and capacity planning for wireless heterogeneous networks in aircraft cabins," in *Proc. IEEE PIMRC '05*, 11-14 Sep. 2005, pp. 2088-2092.

[9] S. Fisahn, M. Camp, N. R. Diaz, R. Kebel and H. Garbe, "General analysis of leaky section cables for multi-band aircraft cabin communications with different measurement techniques," in *Ultra-Wideband Short-Pulse Electromagnetics 7*, 12-16 Jul. 2004, pp. 509-516.

[10] G. A. Breit, H. Hachem, J. Forrester, P. Guckian, K. P. Kirchoff and B. J. Donham, "RF propagation characteristics of in-cabin CDMA mobile phone networks," in *Proc. Digital Avionics Syst. Conf. 2005*, 30 Oct.-3 Nov. 2005, pp. 9.C.5-1--9.C.5-12.

[11] G. Hankins, L. Vahala and J. H. Beggs, "Propagation prediction inside a B767 in the 2.4 GHz and 5 GHz radio bands," in *2005 IEEE AP-S Int. Symp. Dig.*, 3-8 Jul. 2005, pp. 791-794.

[12] N. R. Díaz, B. S. Pérez and F. P. Fontán, "In-cabin deterministic channel modeling: a satellite to aircraft link extension," in *Proc. CNES Workshop on Earth-Space Propagation 2006*, 25-27 Sep. 2006.

[13] R. Bhagavatula, R. W. Heath and S. Vishwanath, "Optimizing MIMO antenna placement and array configuration for multimedia delivery in aircraft," in *Proc. IEEE VTC 2007 – Spring*, 22-25 Apr. 2007, pp. 425-429.

[14] N. R. Díaz, "Narrowband measurements in an Airbus A319 for in-cabin wireless personal communications via satellite," in *Proc. ASMS 2003*, 10-11 Jul. 2003.

[15] N. R. Diaz and J. E. J. Esquitino, "Wideband channel characterization for wireless communications inside a short haul aircraft," in *Proc. IEEE VTC 2004 - Spring*, 17-19 May 2004, pp. 223-228.

[16] J. Chuang, N. Xin, H. Huang, S. Chiu and D. G. Michelson, "UWB radiowave propagation within the passenger cabin of a Boeing 737-200 Aircraft," in *Proc. IEEE VTC 2007 – Spring*, 22-25 Apr. 2007, pp. 496-500.

[17] A. Kaouris, M. Zaras, M. Revithi, N. Moraitis and P. Constantinou, "Propagation measurements inside a B737 aircraft for in-cabin wireless networks," in *Proc. IEEE VTC 2008 - Spring*, 11-14 May 2008, pp. 2932-2936.

[18] J. Jemai *et al.*, "UWB channel modeling within an aircraft cabin," in *Proc. IEEE ICUWB 2008*, 10-12 Sep. 2008, pp. 5-8.

[19] G. A. Breit, H. Hachem, J. Forrester, P. Guckian, K. P. Kirchoff and B. J. Donham, "RF propagation characteristics of in-cabin CDMA mobile phone networks," in *Proc. Digital Avionics Syst. Conf. 2005*, 30 Oct.-3 Nov. 2005, pp. 9.C.5-1--9.C.5-12.

[20] M. Youssef and L. Vahala, "Effects of passengers and internal components on electromagnetic propagation prediction inside Boeing aircrafts," in *2006 IEEE AP-S Int. Symp. Dig.*, 9-14 Jul. 2006, pp. 2161-2164.

[21] M. P. Robinson, J. Clegg and A. C. Marvin, "Radio frequency electromagnetic fields in large conducting enclosures: effects of apertures and human bodies on

propagation and field-statistics," *IEEE Trans. Electromagn. Compat.*, vol. 48, no. 2, pp. 304-310, May 2006.

[22] ECMA International, "High rate – ultra wide band (UWB) background," Available: www.ecma-iternational.org/activities/communicaitons/tg20_UWB_Background.pdf

[23] M. Ward, T. Thorpe, A. Price and C. Wren, "Implementation and control of wireless data collection on construction sites" *Journal of Information Technology in Construction*, vol. 9, Aug. 2004.

[24] K. A. Remley et al., "Measurements to support broadband modulated-signal radio transmissions for the public-safety sector," *National Institute of Standards and Technology*, Technical Note 1546, April 2008.

[25] K. A. Remley, G. Koepke, C. L. Holloway, C. Grosvenor and D. G. Camell, "Radio communications for emergency responders in high-multipath outdoor environments," in *Proceedings of 2008 International Symposium on Advanced Radio Technologies*, June 2008.

[26] I. Guvenc, H. Arslan, S. Gezici and H. Kobayashi, "Adaptation of multiple access parameters in time hopping UWB cluster based wireless sensor networks," in *Proc. Int. Conf. Mobile Ad-hoc Sensor Syst.*, Oct. 2004, pp. 235-244.

Chapter 2

UWB Radiowave Propagation within the Passenger Cabin of a Boeing 737-200 Aircraft[1]

2.1 Introduction

In recent years, there has been considerable interest in deploying personal wireless communications technology aboard passenger aircraft. The European Union's WirelessCabin project provided important guidance concerning the provisioning and delivery of in-cabin wireless services using conventional wireless technologies with satellite-based backhaul [1],[2]. Other past work has included: (1) systems engineering studies and field trials involving conventional wireless technologies such as cellular telephones, wireless LAN and Bluetooth [3]-[5], (2) software-based simulation of wireless propagation within aircraft interiors [6]-[8], and (3) direct measurement of the channel response within aircraft interiors, *e.g.*, [9]-[13].

For airlines, ultrawideband (UWB) wireless technology operating within the frequency band between 3.1 and 10.6 GHz holds great promise for: (1) enabling deployment of high data rate (up to 480 Mbps) in-flight entertainment (IFE) and network access services within aircraft passenger cabins (over ranges of up to 10 m) using WiMedia UWB or similar technology and (2) facilitating operations and maintenance through deployment of sensor networks and precise positioning systems using ZigBee UWB or similar technology. Compared to wired systems, in-cabin wireless offers considerable potential for weight savings and lower reconfiguration costs. Compared to conventional wireless technologies, UWB-based wireless systems occupy a particularly small footprint, radiate little RF energy, and consume little power.

Although pulse-based UWB systems may generate peak powers sufficient to generate significant intermodulation distortion (IMD) products and interfere with aircraft avionics

[1] A version of this chapter has been submitted for publication: S. Chiu, J. Chuang and D. G. Michelson, "UWB radiowave propagation within the passenger cabin of a Boeing 737-200 aircraft."

and navigation systems [14], modern UWB devices based upon spread spectrum or MB-OFDM technologies operate at extremely low peak power levels. A recent NASA study has concluded that modern UWB devices are unlikely to cause interference to aircraft systems [15],[16]. Because the USB Implementer's Forum (USB-IF) and the Bluetooth Special Interest Group (Bluetooth SIG) have announced plans to use WiMedia UWB as the air interface technology for Wireless USB and Bluetooth HS, respectively, it seems likely that many passengers will soon carry UWB-enabled personal electronic devices (PEDs) aboard with the expectation of using them in flight.

Resolution of many airlink issues such as antenna placement, development of link budgets, coverage and capacity planning, development of test and validation strategies, and assessment of mutual interference requires knowledge of the characteristics of the UWB wireless channel. Past efforts to develop measurement-based models of the UWB propagation channel have focused on residential, office, industrial, outdoor and body-centric environments, *e.g.*, [17]-[19]. With its confined volume, cylindrical structure, and high density of occupancy, the passenger cabin of a jet aircraft is fundamentally different from those environments considered previously. To the best of our knowledge, ours is the first study to characterize the UWB propagation channel within such an environment. In this paper, we focus on the manner in which path loss and time dispersion vary with transmitter-receiver separation across the passenger cabin of a typical mid-size airliner.

During the course of this study, we collected several hundred UWB channel frequency responses (CFRs) over the range 3.1-10.6 GHz with the transmitting and receiving antennas at various locations within the passenger cabin of a Boeing 737-200 aircraft. In reducing the measurement data, we have sought: (1) to characterize the distance and frequency dependence and the location variability of path gain in order to better understand the factors that affect coverage and reliability, (2) to characterize time dispersion within the aircraft, including the rms delay spread and the number of significant paths above a given threshold, in order to better understand the nature of the propagation environment, and (3) to consider the implications of our results for the deployment and testing of UWB wireless systems in aircraft passenger cabins. We have not considered either the effect of human presence, which given the high density of occupancy within the aircraft is likely to be considerable, or the fine structure of the UWB channel impulse response, but are doing so in follow-on studies.

The remainder of this paper is organized as follows: In Section 2.2, we describe our VNA-based UWB channel sounder, our procedure for calibrating it, our data collection procedure and our measurement database. In Section 2.3, we present the results of our investigation of the distance and frequency dependence of path gain. In Section 2.4, we present the results of our investigation of time dispersion. Finally, in Section 2.5, we summarize our key findings and their implications.

2.2 Measurement Setup

2.2.1 UWB Channel Sounder Configuration

Our UWB channel sounder consists of an Agilent E8362B vector network analyzer (VNA), 4-m FLL-400 SuperFlex and 15-m LMR-400 UltraFlex coaxial cables, a pair of Electro-metrics 6865 omnidirectional UWB biconical antennas, tripods and fixtures suitable for mounting the antennas at various locations throughout the aircraft, and a laptop-based instrument controller equipped with a GPIB interface. During data collection, a MATLAB script running on the laptop controlled the VNA and logged the received data.

In order to meet RF emission limits imposed upon us by the Research Ethics Boards at the University of British Columbia and the British Columbia Institute of Technology for the human presence study to be conducted as a follow-on to the present work, we set the transmit power to 5 dBm. We set the intermediate frequency bandwidth of the VNA to 3 kHz which reduced the resulting displayed average noise level (DANL) to -107.2 dBm. The minimum sweep time was automatically set to 2 seconds. The system link budget is given in Table 2.1 for the bottom, mid-point and top of the UWB frequency range: 3.1, 6.85 and 10.6 GHz. As configured, the channel sounder can resolve channel impulse responses (CIRs) with an SNR ≥ 25 dB at transmitter-receiver separation distances of up to 15 m assuming average transmit and receive antenna gains of 0 dBi and a distance exponent of 2.

Table 2.1. Link budget for UWB channel sounder.

Links	Values		
	3.1 GHz	6.85 GHz	10.6 GHz
Transmitted Power	5 dBm	5 dBm	5 dBm
Transmit Cable Gain	-4.5 dB	-7.0 dB	-9.1 dB
Transmit Antenna Gain	0 dBi	0 dBi	0 dBi
Path Gain at 15 m*	-65.8 dB	-72.7 dB	-76.5 dB
Receive Antenna Gain	0 dBi	0 dBi	0 dBi
Receive Cable Gain	-4.5 dB	-7.0 dB	-9.1 dB
Received Power	-69.8 dBm	-81.7 dBm	-89.7 dBm
Receiver Sensitivity	-107.2 dBm	-107.2 dBm	-107.2 dBm
System Margin	37.4 dB	25.5 dB	17.5 dB

*Calculated using a path loss exponent of 2.

During data collection, we configured the VNA to sweep from 3.1 to 10.6 GHz over 6401 frequencies. The frequency sampling interval of 1.1716 MHz corresponds to a maximum unambiguous excess delay of 853 ns or a maximum observable distance of 256 m. The frequency span of 7.5 GHz gives us a temporal resolution of 133 ps or a spatial resolution of 40 mm.

2.2.2 UWB Channel Sounder Calibration

Before measurement data can be collected, the channel sounder must be calibrated so that systematic variations in the amplitude and phase of the measured frequency response due to factors other than the propagation channel can be removed. The process involves two steps. The first step is to use the VNA's built-in calibration routines, which are based upon a standard 12-term error model, to compensate for amplitude and phase distortions up to the point where the cables attach to the transmitting and receiving antennas. Care must be taken to ensure that the distortions for which the error correction model is compensating do not change appreciably during the measurement session, *e.g.*, due to significant cable flexion and torsion, so that the error correction process will not introduce its own distortions. Appropriate cable handling and management techniques are the most effective way to avoid such problems.

The second step, which is much more difficult, is to compensate for the distortions introduced by the antennas themselves. Because the radiation patterns of practical UWB antennas vary with both direction and frequency, individual multipath components (MPCs) arriving at the receiving antenna from different directions will be distorted in different ways. The measured channel response includes elements of the response of

both: (1) the *propagation channel* and (2) the transmitting and receiving antennas. The result is often referred to as the response of the *radio channel*. In order to perfectly de-embed the propagation channel response from the radio channel response, one would need to measure the frequency-dependent double-directional channel response that accounts for the angle-of-departure (AoD) and angle-of-arrival (AoA) of each ray and the frequency-dependent three-dimensional radiation pattern of each antenna [18]. Implementing the required measurement setup within the confines of the aircraft passenger cabin would be problematic, however.

The antenna calibration problem is simplified considerably if we can assume that the environment is rich with scatterers so that the physical MPCs arrive from all possible directions and each resolvable MPC includes many physical MPCs. Because the directivity of any antenna averaged over all directions is unity for all frequencies, the measured CFR will be independent of the radiation patterns of the transmitting and receiving antennas. In such cases, after appropriate account has been taken for the return loss of the antennas and the amplitude of any line-of-sight (LOS) components, the measured channel response will be equivalent to the propagation channel response.

Although the confined nature of the aircraft passenger cabin makes it unlikely that scattering is truly isotropic, the dense single cluster form of the CIRs that we observed within that environment suggests that the density of scatterers within the cabin is very high and the AoA distribution is very wide. While our results strictly characterize the radio channel, it is not unreasonable to assume that the scattering is sufficiently broad that the effective gain of the transmitting and receiving antennas over all directions and frequencies is unity. In that case, the measured channel response is a useful approximation to the propagation channel response.

2.2.3 Measurement Plan

We collected our CFR measurements within the passenger cabin of a Boeing 737-200 aircraft. The cabin, which can seat over 100 passengers, is 3.54 m in width, 2.2 m in height and 21 m in length of which 18 m actually includes passenger seating. Plan and cross-sectional views of the passenger cabin are shown in Figure 2.1 and Figure 2.2, respectively. Other modern mid-sized airliners, such as the CRJ series from Bombardier,

the A320 family from AirBus Industries and the ARJ21 family from ACAC, have similar cross-sections, as shown in Table 2.2. Only the lengths of the passenger cabins, which range from 12 to 43 m, are appreciably different.

In our measurement campaign, we considered two wireless system configurations: point-to-multipoint (p-to-mp) and peer-to-peer (p-to-p). In the p-to-mp configuration, we mounted the transmitting antenna on the ceiling along the centerline of the aircraft in the manner of an access point, as shown in Figure 2.1(a) and Figure 2.2. In the p-to-p configuration, we mounted the transmitting antenna on the headrest, armrest and footrest level of a passenger seat in the manner of personal electronic devices such as phones or headsets, computers or PDAs, or such devices stored in carry-on baggage, respectively, as shown in Figure 2.1(b) and Figure 2.2. In both cases, we mounted the receiving antenna at the headrest, armrest and footrest level of selected passenger seats throughout the aircraft using custom-built mounting adapters. The p-to-p configuration yielded nine unique combinations of transmitting and receiving antenna positions.

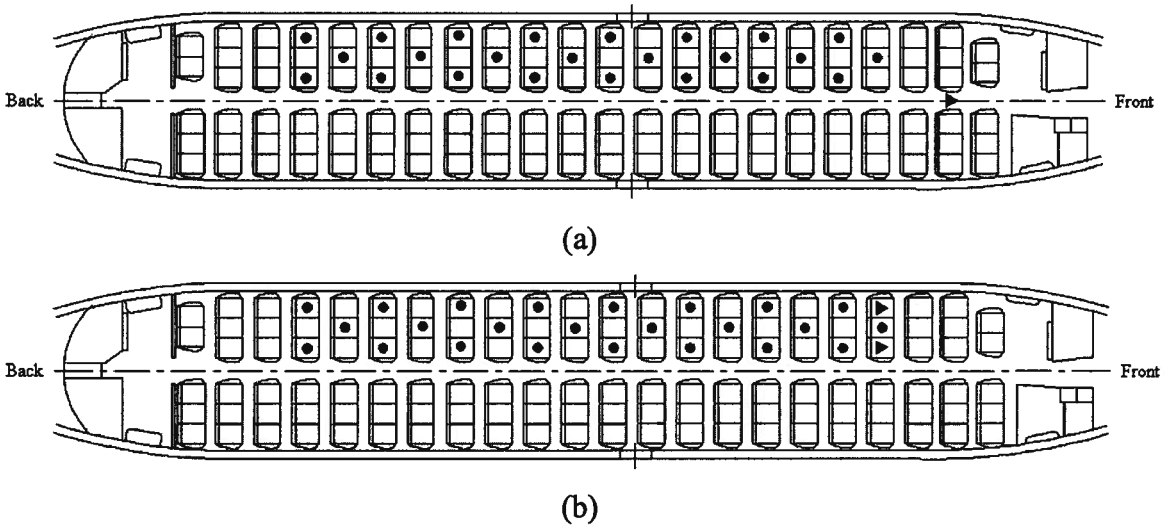

Figure 2.1. Locations at which the transmitting antenna (▶) and receiving antenna (●) were deployed within the Boeing 737-200 aircraft during the channel measurements in (a) point-to-multipoint and (b) peer-to-peer configurations.

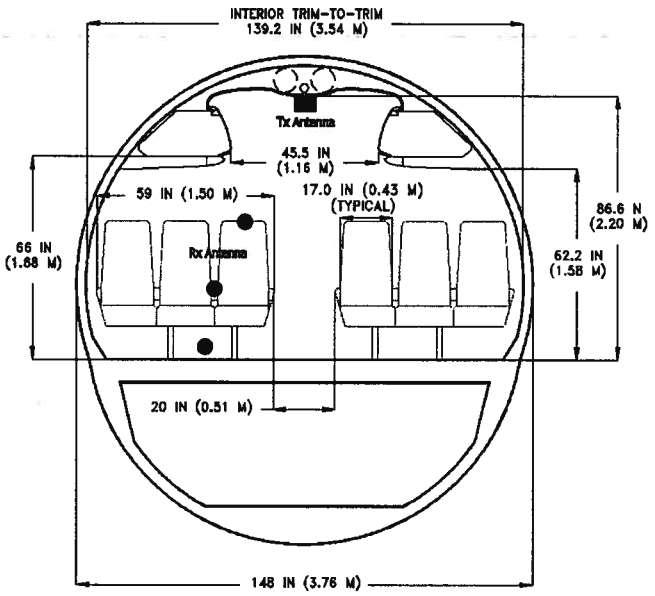

Figure 2.2. Cross-sectional view of the passenger cabin showing the positions at which the transmitting and receiving antennas were deployed in the point-to-multipoint configuration. In the peer-to-peer configuration, the transmitting antenna was also mounted on a passenger seat at the headrest, armrest or footrest.

Table 2.2. Dimensions of modern mid-sized airliner passenger cabins.

Manufacturer	Cabin Width (m)	Cabin Height (m)	Cabin Length (m)
Bombardier CRJ	2.53	1.85	12.34 – 21.16
Embraer E-Jet	2.74	2.00	19.43 – 21.20
ACAC ARJ21	3.14	2.03	18.43
Boeing 737	3.54	2.20	21.00 – 24.13
Boeing 757	3.54	2.20	36.09 – 43.21
AirBus A320	3.70	2.22	27.50

Before collecting production data, we conducted development runs in order to become familiar with the environment, identify any issues with the measurement equipment or data collection procedures and identify models against which the measurement data could be reduced. During our development runs for the p-to-mp configuration, we verified the static nature of the channel and the consistency of our measurements by demonstrating that consecutive CFR measurements over a given path within the cabin were essentially identical. This allowed us to take just one sweep per location during production runs and thereby dramatically reduce the number of measurements needed to characterize the passenger cabin.

We introduced further redundancy checks into our measurement database by collecting channel response data at every other seat on both sides of the aircraft from row 4 to row 19, *i.e.*, at 53 different seats, for each of three transmitting antenna locations at rows 2, 11 and 16. The results confirmed our expectation that: (1) the distance dependence of path gain is relatively independent of the transmitting antenna location and (2) the responses measured on both sides of the bilaterally symmetric passenger cabin are essentially identical. Once we had verified that the expected symmetries and similarities appeared in the results, we were able to take advantage of them to further reduce the number of measurements required to characterize the aircraft. For example, in our production runs, we placed the transmitting antenna at a single location on the cabin ceiling and limited our collection of measurement data to the port side of the cabin, as suggested by the layout depicted in Figure 2.1.

2.2.4 Measurement Database

During our development runs for the p-to-mp configuration, we considered three transmitter locations and over 50 receiver locations. For selected paths, we collected multiple sweeps in order to verify the static nature of the channel. This yielded over 200 CFRs. During our production runs, we collected measurements at the headrest, armrest and footrest of 24 seats on the port side of the cabin yielding 72 CFRs. In total, we collected almost 300 CFRs in the p-to-mp configuration.

During our production runs for the p-to-p configurations, we placed the transmitting antenna locations at the window and aisle seat of row 4. For each transmitter location, we used nine different transmitter/receiver combinations, yielding 396 CFRs. During our development runs, we collected another set of 198 CFRs on the starboard side of the cabin in order to verify the symmetry of the environment. In total, we collected almost 600 CFRs in the p-to-p configuration.

2.3 Path Gain in the Aircraft Environment

In UWB systems, both the distance and frequency dependence of path gain must be accounted for. The IEEE 802.15.4a channel modeling committee adopted the UWB path gain model given by

$$G_p(d,f) = G_{p0}\left(\frac{d}{d_0}\right)^{-n}\left(\frac{f}{f_c}\right)^{-2\kappa}, \tag{2.1}$$

where G_p is the path gain, d is the distance from the transmitter to the receiver, f is the carrier frequency, G_{p0} is a constant that represents the path gain at d_0 and f_c , the reference distance and frequency, respectively, and n and κ are the distance and frequency exponents, respectively. Although the 4a modeling committee assumed that path gain is separable in distance and frequency they acknowledge that further study is required to determine how true this is in practice [19].

The path gain at a given distance and frequency can be estimated from measured data using

$$G_p(d,f) = \frac{P_r(d,f)}{P_t}\frac{1}{G_t(f)G_r(f)}, \tag{2.2}$$

where P_t is the transmitted power, Pr is the received power at a given distance and frequency, and G_t and G_r are the effective gains of the transmitting and receiving antennas given the nature of the scattering in the environment, as described in Section 2.2.2. Fitting the model given by equation (2.1) to the values of $G_p(d, f)$ for many locations yields estimates of G_{p0}, n and κ.

2.3.1 The Distance Dependence of Path Gain

The manner in which path gain decreases with distance determines the maximum range that can be achieved by a wireless link. For UWB-based wireless systems, path gain is an especially important consideration given the relatively low power levels that such systems are permitted to radiate. The p-to-mp path gain model that we present here will allow system designers to predict the coverage and reliability of UWB-based wireless systems within the passenger cabin. Our p-to-p path gain model will allow

designers to assess the potential for interference between UWB-based PEDs used aboard the aircraft.

Following [20], we took the average of the measured complex CFRs across the entire span from 3.1 to 10.6 GHz in order to obtain the distance-dependent path gain,

$$G_p(d) = \frac{1}{M}\sum_{i=1}^{M} G_p(d, f_i), \tag{2.3}$$

where M is the number of frequency steps. Path gain decreases with increasing transmitter-receiver separation due to the combined effects of spatial spreading and obstruction by cabin fixtures and seating. In decibels, the path gain with respect to distance at the reference frequency f_c is

$$G_p(d) = G_{p0} - 10n\log_{10}\left(\frac{d}{d_o}\right) + X_\sigma, \tag{2.4}$$

where d_0 = 1 m is the reference distance, f_c = 6.85 GHz is the reference frequency, n is the distance exponent and X_σ is a zero-mean Gaussian random variable with a standard deviation of σ that accounts for location variability. We determined the distance exponent n and the intercept point G_{p0} by applying regression analysis to the measured data. We estimated σ by subtracting the regression line from the measured values of path gain and fitting the results to a Gaussian distribution. The results are presented in Table 2.3, which gives a complete summary of the path gain parameters that apply to the model given by equation (2.1) for both the p-to-mp and p-to-p configurations.

Table 2.3. Large-scale UWB parameters for the aircraft passenger cabin environment.

System Configuration	Path Type	G_{p0} [dB]	Distance exponent, n	Location variability, σ [dB]	Frequency exponent, κ	RMS delay spread exponent, γ
Point to Multipoint	All	-41.5	2.29	2.52	0.78	1.35
	C-to-H	-39.8	2.19	1.39	0.43	1.30
	C-to-A	-41.8	2.30	1.98	0.86	1.45
	C-to-F	-43.9	2.27	1.22	1.06	1.17
Peer to Peer	All	-41.0	2.49	1.81	1.06	1.83
	H-to-H	-41.7	2.12	1.27	0.91	0.89
	H-to-A	-41.9	2.26	1.07	0.99	1.89
	H-to-F	-42.8	2.43	1.03	1.16	1.75
	A-to-H	-41.2	2.37	1.12	1.04	1.60
	A-to-A	-42.5	2.43	1.56	1.20	1.85
	A-to-F	-41.6	2.64	1.31	1.19	1.90
	F-to-H	-38.6	2.65	0.73	1.02	2.04
	F-to-A	-39.7	2.68	1.40	1.10	2.04
	F-to-F	-37.4	3.01	1.02	0.79	2.92

Note: C = Ceiling, H = Headrest, A = Armrest, F = Footrest

In free space environments, the distance exponent n is equal to 2 as a direct consequence of spatial spreading. In conventional environments which are distinguished by a dense concentration of scatterers, the distance exponent for UWB signals is often less than 2 because additional energy is contributed by scattered components of the received signal [19],[21]. For example, in industrial environments, distance exponents of only 1.2 have been observed [19]. Within the aircraft passenger cabin environment, one might expect that the distance exponent to be similar. As shown in Table 2.3, however, the measured distance exponent is often higher than the free space value. This is likely due to the abundance of RF absorbers within the cabin, *e.g.*, seats, overhead compartments, *etc.*

Figure 2.3(a) shows how path gain in the p-to-mp configuration varies with respect to distance for the different receiving antenna mounting positions. As expected, the path gains observed at the headrest positions are always greater than those observed at the corresponding armrest and footrest positions. Because of the direct LOS paths at all inboard armrest positions, the observed path gains at these positions are higher than those observed at outboard armrest positions and are comparable to those observed at headrest positions. In addition, some headrest positions are not entirely LOS because the paths are obstructed by the overhead compartments. If we consider only the case where the receiving antenna is placed on the headrest of an aisle seat, i.e., the positions where the highest path gains are observed, then the distance exponent drops to 1.84 with an intercept of -40.3 dBm and location variability of 0.45 dB.

Figure 2.3(b) shows how path gain varies with distance for the p-to-p configuration. The headrest-to-headrest data is marked separately because it is the only p-to-p path type that has a LOS path between the transmitting and receiving antennas. The observed values of path gain for other path types are all very comparable. Similar to the p-to-mp case, the distance exponent is a function of the receiving antenna position, *i.e.*, the distance exponent increases as the receiving antenna is lowered from headrest to footrest. Unlike the p-to-mp case, however, the location of the receiver, whether it is on an aisle or a window seat does not matter.

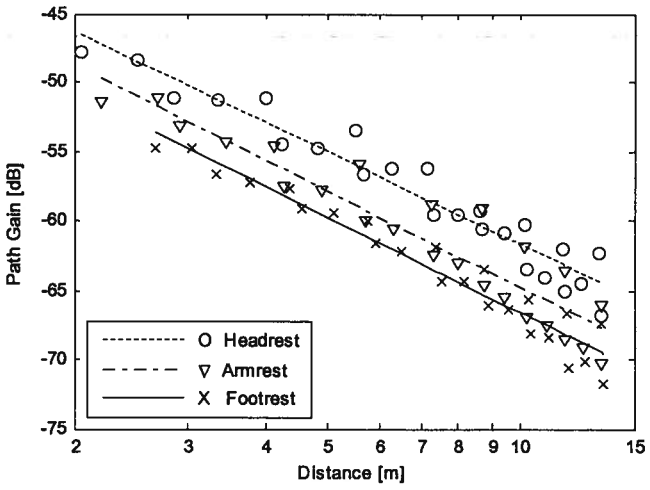

(a)

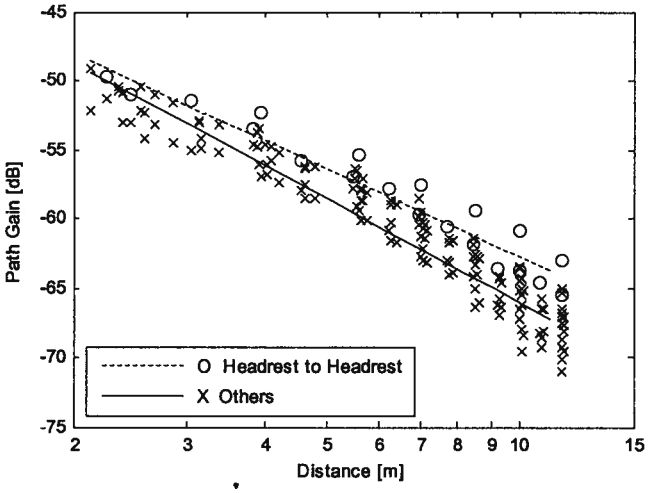

(b)

Figure 2.3. The measured distance dependent path gain and the corresponding regression line for (a) point-to-multipoint to the indicated position and (b) peer-to-peer configurations. For clarity, only the data points that correspond to transmitter location at the window seat are shown in (b). The regression lines, however, are for both transmitter locations at the window and aisle seats.

2.3.2 A Simplified Three Dimensional Point-to-Multipoint Coverage Model

The cylindrical geometry of the aircraft and the regular layout of the passenger seats combine to give rise to a regular coverage pattern throughout the passenger cabin. Figure 2.4(a) shows the two-dimensional coverage within the passenger cabin based on path

gain data collected with the transmitting antenna mounted at the ceiling and the receiving antenna mounted at the headrest position at various locations throughout the aircraft, as described previously. The chevron shaped contours in the coverage pattern are mainly due to shadowing by the overhead compartments.

The structure of the coverage pattern presented in Figure 2.4(a) suggests that one can devise an expression for path gain (in dB) that accounts for the position of the receiving antenna in three dimensions. Let

$$G_p(d) = G_{p0} - 10n_{LOS}\log_{10}\left(\frac{d}{d_o}\right) - G_S + X_\sigma, \tag{2.5}$$

where: (1) the first two terms give the LOS path gain experienced by a receiving antenna mounted on the headrest of an aisle seat at a distance d, and n_{LOS} is the distance exponent applicable to this configuration, (2) G_S accounts for shadowing due to furnishings and fixtures within the aircraft as the antenna is moved toward the window seat or lowered below the headrest, and (3) X_σ accounts for the location variability that remains.

Depending on the location (row and seat) and mounting position (headrest, armrest, or footrest) of the receiving antenna, shadowing may be due to the overhead compartments, the passenger seats, or a combination of both. Here, we propose to express the depth of shadowing (in dB) below the headrest and outboard of the aisle as

$$G_S(d_x, d_z) = \alpha d_x + \beta d_z, \tag{2.6}$$

where d_x is the distance from the edge of the aisle passenger seat to the antenna and d_z is the distance from the top of the passenger seat to the antenna. We estimated the coefficients α and β by: (1) calculating the difference between: (a) the path gain experienced at each of the locations and mounting positions at which we collected data and (b) the path gain experienced at the headrest on the aisle seat in the corresponding row and then (2) fitting a plane to the result over all locations and mounting positions. We found that $\alpha = 4.02$ dB/m and $\beta = 3.98$ dB/m, respectively, yielded the best fit. The similarity of the two parameters suggests that the extent of shadowing by the overhead compartments is very similar to that of the passenger seats. The resulting coverage pattern is given in Figure 2.4(b). The more detailed path gain model given by equations (2.5) and (2.6) offers a more concise description of coverage in the cabin than the simplified path-specific models given by equation (2.4) and the parameters in Table 2.3

while its residual location variability of σ = 1.1 dB is slightly less than that associated with the simplified path-specific models.

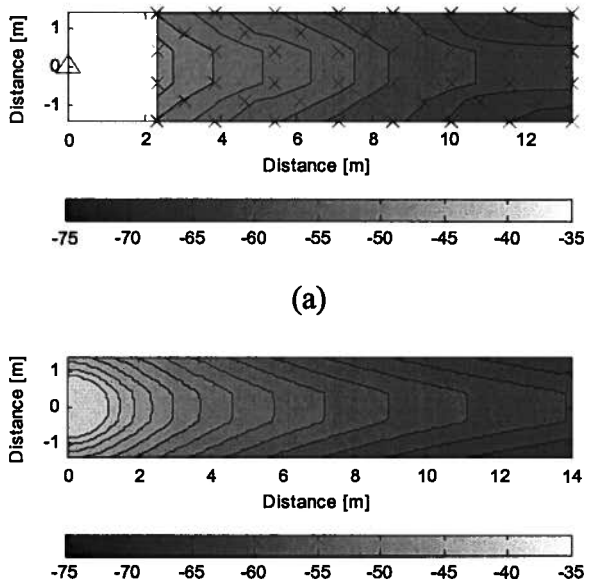

(a)

(b)

Figure 2.4. UWB path gain (in dB) within the passenger cabin with the transmitting antenna (Δ) mounted at the ceiling (0, 0) and receiving antenna (×) mounted on the headrest at various locations: (a) measured data with contours and (b) simplified regression model with contours.

2.3.3 The Frequency Dependence of Path Gain

The IEEE 802.15.4a channel modeling committee has recommended that the frequency dependence of path gain be modeled as

$$\sqrt{G_p(f)} \propto f^{-\kappa}. \tag{2.7}$$

The tendency for path gain to either increase or decrease with frequency over ultra wide bandwidths has several important consequences: First, the coverage of a system may be severely degraded at the highest frequency in its range compared to the lowest frequency. Second, a substantial difference between the path gain in the upper and lower portions of a sub-band may severely degrade the performance of systems that utilize Multiband Orthogonal Frequency Division Multiplexing (MB-OFDM). Finally, depending on the value of κ, the channel may either act as an integrator or a differentiator, severely

distorting the transmitted waveform and degrading the performance of coherent receivers [22].

If the environment is free space and the gains of the transmitting and receiving antennas do not vary with frequency, path gain decreases with frequency and the frequency exponent $\kappa = 1$. In practical environments, additional frequency dependence can be introduced by: (1) diffraction across blocking objects, (2) scattering from rough surfaces, (3) wall penetration, where the material reflection coefficients are frequency-dependent, (4) frequency-selective reflection from metallic objects of specific geometric shapes such as railings and gratings, and (5) vector superposition of overlapping signal waveforms in a dense multipath channel, altering the frequency content of individual MPCs [22].

The characteristics of the antennas also play an important role in determining the value of the frequency exponent κ. If constant gain is assumed but the apertures of the transmitting and receiving antennas are actually constant with frequency, path gain will appear to increase with frequency and $\kappa = -1$. If constant gain is assumed but the aperture of either of the antennas is actually constant with frequency, then path gain will appear to be flat with frequency and $\kappa = 0$. In practical UWB measurement environments, the antenna pattern often narrows (and gain increases) with frequency. If the path is non-line-of-sight (NLOS) and the AoA distribution is isotropic, $\kappa = 1$ regardless of the free space characteristics of the antenna. However, as the AoA distribution narrows, the effective gain of the receiving antenna will increase as a function of frequency. If uniform directivity has been assumed, κ will appear to drop. For this reason, we have taken particular care when interpreting the values of κ that we obtained by reducing measurement data.

We estimated the values of κ for different path types and presented the results in Table 2.3. We observe that for channels with a stronger LOS component, the frequency exponent drops below the value expected in an isotropic scattering environment and we observe $0.4 < \kappa < 0.9$. This is likely because, in a LOS channel, most of the energy departs and arrives along the broadside of the antennas, and rays observe the combined peak gains of the antennas. In such a case, the effect of antenna gains increasing with frequency roughly cancels that of the effective aperture of the receiving antenna decreasing with frequency, and we observe, more or less, only the frequency dependence

of the channel. In a channel without a strong LOS component, the effect of the receiving antenna aperture dominates the CFR, resulting in values of κ more typical of an isotropic scattering environment and we observe $0.9 < \kappa < 1.2$.

We assessed the effect of carrier frequency on system coverage and isolation as follows. Using an in-cabin link operating at 3.1 GHz over a 10-m distance as a reference, we determined the distance at which in-cabin links at 10.6 GHz would experience the same path gain as the 3.1 GHz reference. As the frequency increases from 3.1 to 10.6 GHz, coverage in p-to-mp configurations is reduced by half and in p-to-p configurations, by almost two-thirds. Next, we determined the reduction in path gain (or increase in isolation) at 10.6 GHz at a transmitter-receiver separation distance of 10-m compared to the 3.1 GHz reference. Isolation in the p-to-mp and p-to-p configurations, respectively, increased by 8.3 dB and 11.3 dB. The detailed results are given in Table 2.4. We conclude that there appears to be significant advantage to using higher portions of the UWB band for short-range p-to-p links and reserving lower portions of the band for longer range p-to-mp links within the aircraft passenger cabin.

Table 2.4. Fraction of coverage and increase in isolation at 10.6 GHz compared to in-cabin links at 3.1 GHz.

System Configuration	Path Type	Fraction of Coverage [%]	Increase in Isolation [dB]
Point to Multipoint	All	48	8.3
	C-to-H	65	4.6
	C-to-A	45	9.2
	C-to-F	36	11.3
Peer to Peer	All	40	11.3
	H-to-H	40	9.7
	H-to-A	39	10.6
	H-to-F	36	12.4
	A-to-H	39	11.1
	A-to-A	34	12.8
	A-to-F	38	12.7
	F-to-H	44	10.9
	F-to-A	41	11.7
	F-to-F	57	8.4

Note: C = Ceiling, H = Headrest, A = Armrest, F = Footrest

2.4 Time Dispersion in the Aircraft Environment

Our first step in characterizing time dispersion within the aircraft passenger cabin was to convert our measured CFRs into CIRs. Following [20], we applied a Kaiser window with $\beta = 7$ to the CFR in order to suppress dispersion of energy between delay bins. We then applied an inverse Fourier transform (IFT) directly to the complex baseband of the CFR without any zero padding to yield a CIR. The result can be expressed in the form of a power delay profile (PDP),

$$P_h(\tau_k) = \left|h(\tau_k)\right|^2 = \sum_k a_k \delta(\tau - \tau_k), \tag{2.8}$$

where a_k is the amplitude (expressed in units of power gain) of the resolvable MPC at delays τ_k, and we have ignored the effect of frequency dependent path gain on the shape of individual MPCs. If the MPC amplitudes are scaled so that their sum is unity, the PDP is said to be normalized.

Measured PDPs typical of those observed over LOS and NLOS channels in the aircraft are shown in Figure 2.5(a) and (b), respectively. The high density of MPCs in the PDPs suggests that the density of scatterers within the passenger cabin is also high. In the p-to-mp configuration, the channel response generally has a LOS component whenever the receiving antenna is placed at the headrest or on the inboard armrest of an aisle seat. In the p-to-p configuration, the channel response generally does not have a LOS component unless both the transmitting and receiving antennas are placed at the headrest. When the PDP has a LOS component, we define its start as the first MPC that arrives within 10 dB of, and 10 ns, before the peak MPC. When only scattered components are present, the first arriving components of the PDP generally exhibit a slow rise to a maximum value then a slow decay. For such NLOS channels, we define the start of the PDP as the first MPC that arrives within 10 dB of, and 50 ns, before the peak MPC. We remove the propagation delay by setting the start time of the first arriving MPC to zero. These criteria are based upon those described in [23].

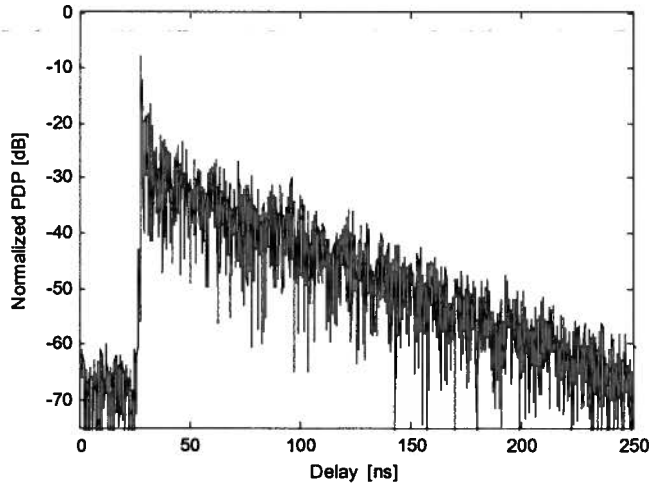

(a)

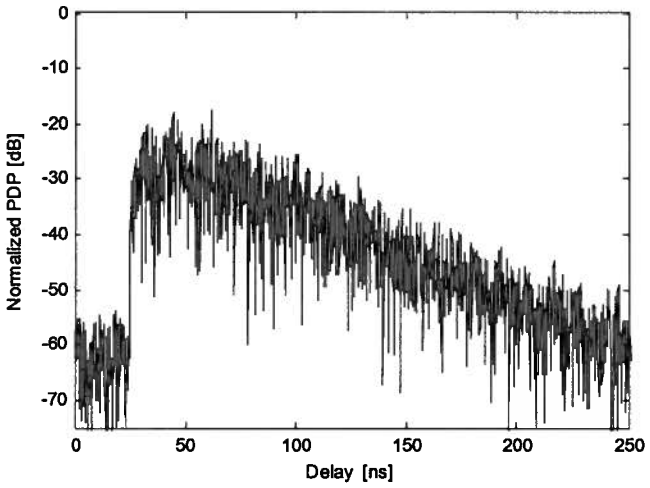

(b)

Figure 2.5. Typical normalized power delay profiles for (a) LOS channel (ceiling-to-headrest) at row 14 and (b) NLOS channel (ceiling-to-footrest) at row 12.

2.4.1 Delay Spread

The normalized first-order moment of a PDP gives the mean excess delay,

$$\tau_{mean} = \frac{\sum_k P_h(\tau_k)\tau_k}{\sum_k P_h(\tau_k)}, \tag{2.9}$$

while the square root of the second central moment of a PDP gives the rms delay spread,

$$\tau_{rms} = \sqrt{\tau_{mean}^2 - (\tau_{mean})^2}, \tag{2.10}$$

where

$$\tau_{mean}^2 = \frac{\sum_k P_h(\tau_k)\tau_k^2}{\sum_k P_h(\tau_k)}. \tag{2.11}$$

In the aircraft environment, the PDP may include both: (1) scattered components that give rise to the dense single cluster that accounts for the bulk of the energy in the response and (2) impulses that appear near the leading edge of the PDP and which are the result of either LOS transmission or specular reflection from the cabin floor, ceiling or bulkhead. Before we estimated the rms delay spread, we removed all MPCs with amplitudes that are more than 25 dB below the peak scattered component. This ensures that: (1) only significant MPCs are considered and (2) the shape of the PDP is not unduly biased by the initial LOS component.

The rms delay spread generally increases with transmitter-receiver separation distance d, as shown in Figure 2.6. We model the distance dependence as proportional to d^{γ} where values of γ for various transmitter/receiver configurations are given in Table 2.3. The magnitudes of the rms delay spreads that we observed are about one-quarter of the values reported in [10] for a similar environment. However, those measurements were collected using a conventional wideband channel sounder with an effective measurement bandwidth of just 120 MHz; our much smaller rms delay spread is a consequence of our much larger measurement bandwidth of 7.5 GHz [24]. The range of rms delay spreads that we observed within the aircraft passenger cabin (between 12 and 38 ns) are comparable to the mean values previously obtained for residential environments [20] and smaller than those observed in industrial environments [25].

From the results presented in Figure 2.6, it is apparent that the rms delay spread experienced over in-cabin wireless channels tends to be lower in the LOS case than in the NLOS case. One could attribute such a reduction to an increase in the rate at which the amplitude of scattered components drop as delay increases, an increase in the amplitude of the LOS component, or both. In the LOS case, the relationship between the actual delay spread, τ_{rms}, and the rms delay spread of *the scattered components* alone, T_{rms}, is given by

$$\tau_{rms}^2 = \frac{T_{rms}^2}{1+K}\left(1+\frac{K\exp(-\Delta\tau/\tau_0)}{1+K}\right). \tag{2.12}$$

where K is the ratio of the power in the LOS spike and scattered components, $\Delta\tau$ is the temporal resolution, and τ_0 is the decay time constant of the scattered components [26]. Although both K and τ_0 can affect τ_{rms}, we found that τ_0 averaged over all measurement locations for LOS and NLOS channels are 25.4 ns and 27.0 ns, respectively, or essentially the same. Thus, the difference between τ_{rms} for the LOS and NLOS cases in Figure 2.6(a) is almost completely due to the presence or absence of a LOS component.

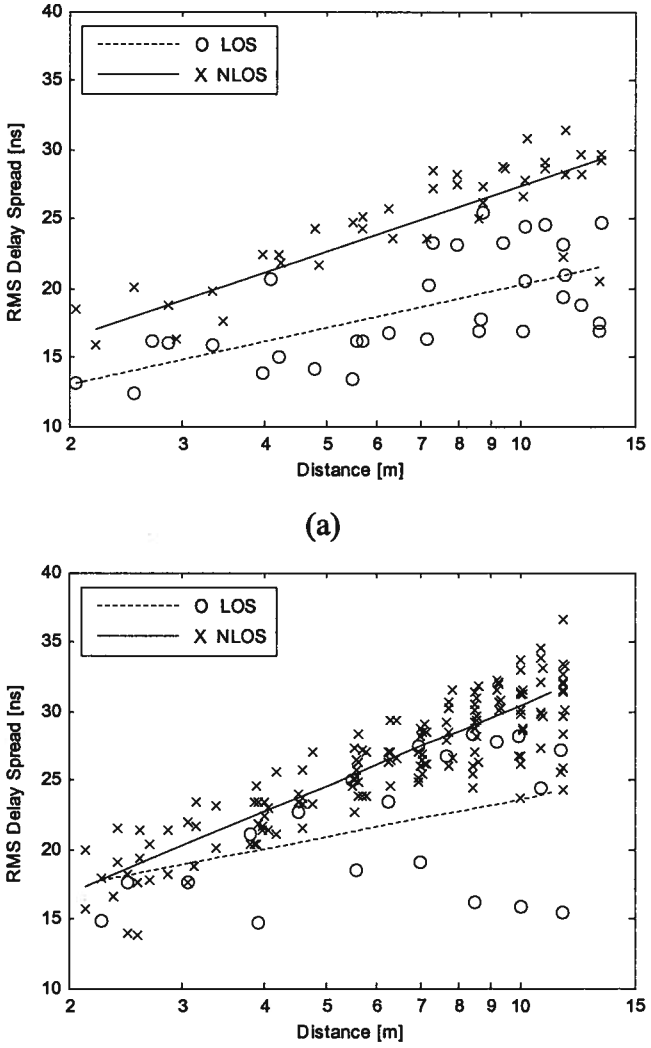

Figure 2.6. The rms delay spread with respect to distance for (a) point-to-multipoint and (b) peer-to-peer configurations. For clarity, the plot in (b) shows only the data points collected with the transmitter located at the window seat.

2.4.2 Number of Significant Paths

We define a significant path as a resolvable MPC that exceeds a given threshold of 5, 10, 15 and 20 dB below the strongest MPC. CDFs of the number of significant paths observed in the PDP for both the p-to-mp and p-to-p configurations are presented in Figure 2.7. The number of significant paths that we observed for each of the path types (p-to-mp or p-to-p) and the percentage of energy that each set captures as a function of the threshold level are summarized in Table 2.5. Compared to previous results, the aircraft environment has many more significant paths at a given threshold than do residential or office environments [19],[20], but a comparable number to those observed in industrial environments [25].

Table 2.5. Mean excess delay, rms delay spread, number of significant paths and energy captured for different threshold levels.

System Configuration	Threshold [dB]	τ_{mean} [nsec]	τ_{rms} [nsec]	Num. of Paths	% Power
Point to Multipoint	5	7.2	5.6	18	31
	10	12.1	11.1	82	56
	15	16.8	15.8	200	75
	20	19.9	19.5	355	88
Peer to Peer	5	13.2	8.3	34	28
	10	18.3	13.1	163	63
	15	22.8	17.3	360	85
	20	25.8	20.6	578	94

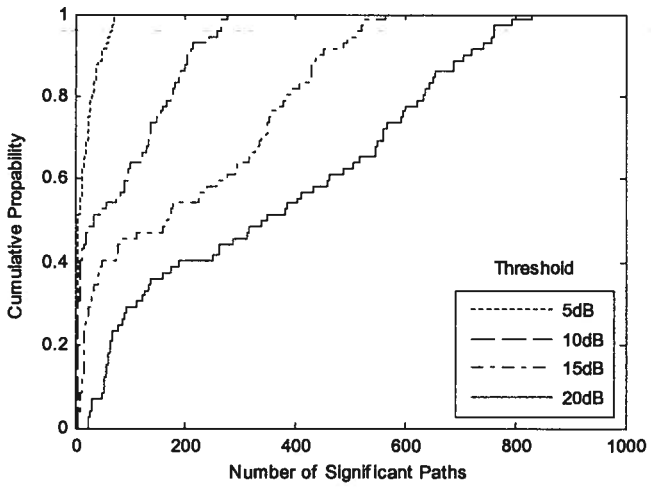

(a)

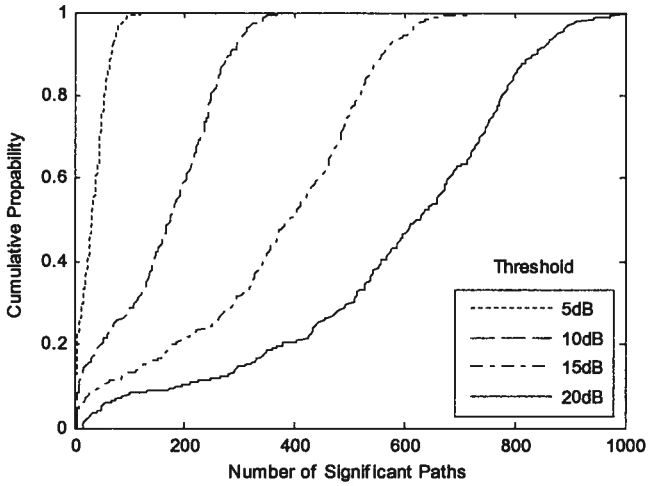

(b)

Figure 2.7. CDF of the number of significant paths for (a) point-to-multipoint and (b) peer-to-peer configuration for thresholds between 5 and 20 dB.

2.5 Conclusions

With its confined volume and cylindrical structure, and the dense and regular layout of its seating, the passenger cabin of a mid-sized airliner is quite distinct from the residential, office, industrial, outdoor and bodycentric environments previously considered by the IEEE 802.15.4a channel modeling committee and its contributors. Our investigation of time dispersion within the cabin reveals that scattering and reflection

accounts for the bulk of the energy that arrives at a given receiving antenna, including cases where a clear LOS exists. Our investigation of path gain within the cabin reveals that the dense and regular layout of the seats and obstruction by the overhead bins cause the coverage pattern to take the form of chevron-shaped contours with path gain decreasing least rapidly along the aisle seats and most rapidly along the window seats. Moreover, as the frequency increases from 3.1 to 10.6 GHz, coverage in p-to-mp configurations is reduced by half while in p-to-p configurations it is reduced by almost two-thirds. Thus, there is significant advantage to using higher frequency portions of the UWB allocation for short-range p-to-p links and reserving lower frequency portions of the band for long-range p-to-mp links within such environments.

We have not considered either the effect of human presence, which given the high density of occupancy within the aircraft is likely to be considerable, or the fine structure of the UWB channel impulse response, but are doing so in follow-on studies. In this work, we have only considered the possibility of mounting the access point in the p-to-mp configuration along the centerline of the cabin. While this provides symmetrical coverage across the cabin and keeps the access point at the greatest possible distance from seated passengers, there may be practical reasons why it may be desirable to mount the access point at a lower height on a cabin wall instead, *e.g.*, proximity to cabin wiring, avoidance of blockage by the overhead bins, etc. Evaluating the consequences of such an alternative mounting location is a topic for future work.

2.6 References

[1] N. R. Diaz and M. Holzbock, "Aircraft cabin propagation for multimedia communications," in *Proc. EMPS 2002*, 25-26 Sep. 2002, pp. 281-288.

[2] A. Jahn *et al.*, "Evolution of aeronautical communications for personal and multimedia services," *IEEE Commun. Mag.*, vol. 41, no. 7, pp. 36-43, Jul. 2003.

[3] C. P. Niebla, "Topology and capacity planning for wireless heterogeneous networks in aircraft cabins," in *Proc. IEEE PIMRC 2005*, 11-14 Sep. 2005, pp. 2088-2092.

[4] S. Fisahn, M. Camp, N. R. Diaz, R. Kebel and H. Garbe, "General analysis of leaky section cables for multi-band aircraft cabin communications with different measurement techniques," in *Ultra-Wideband Short-Pulse Electromagnetics 7*, 12-16 Jul. 2004, pp. 509-516.

[5] G. A. Breit, H. Hachem, J. Forrester, P. Guckian, K. P. Kirchoff and B. J. Donham, "RF propagation characteristics of in-cabin CDMA mobile phone networks," in *Proc. Digital Avionics Syst. Conf. 2005*, 30 Oct.-3 Nov. 2005, pp. 9.C.5-1--9.C.5-12.

[6] G. Hankins, L. Vahala and J. H. Beggs, "Propagation prediction inside a B767 in the 2.4 GHz and 5 GHz radio bands," in *2005 IEEE AP-S Int. Symp. Dig.*, 3-8 Jul. 2005, pp. 791-794.

[7] N. R. Díaz, B. S. Pérez and F. P. Fontán, "In-cabin deterministic channel modeling: a satellite to aircraft link extension," in *Proc. CNES workshop on Earth-Space Propagation* 2006, 25-27 Sep. 2006.

[8] R. Bhagavatula, R. W. Heath and S. Vishwanath, "Optimizing MIMO antenna placement and array configuration for multimedia delivery in aircraft," in *Proc. IEEE VTC 2007 – Spring*, 22-25 Apr. 2007, pp. 425-429.

[9] N. R. Díaz, "Narrowband measurements in an Airbus A319 for in-cabin wireless personal communications via satellite," in *Proc. ASMS 2003*, 10-11 Jul. 2003.

[10] N. R. Diaz and J. E. J. Esquitino, "Wideband channel characterization for wireless communications inside a short haul aircraft," in *Proc. IEEE VTC 2004 - Spring*, 17-19 May 2004, pp. 223-228.

[11] J. Chuang, N. Xin, H. Huang, S. Chiu and D. G. Michelson, "UWB radiowave propagation within the passenger cabin of a Boeing 737-200 Aircraft," in *Proc. IEEE VTC 2007 – Spring*, 22-25 Apr. 2007, pp. 496-500.

[12] A. Kaouris, M. Zaras, M. Revithi, N. Moraitis and P. Constantinou, "Propagation measurements inside a B737 aircraft for in-cabin wireless networks," in *Proc. IEEE VTC 2008 - Spring*, 11-14 May 2008, pp. 2932-2936.

[13] J. Jemai *et al.*, "UWB channel modeling within an aircraft cabin," in *Proc. IEEE ICUWB 2008*, 10-12 Sep. 2008, pp. 5-8.

[14] J. J. Ely, G. L. Fuller and T. W. Shaver, "Ultrawideband electromagnetic interference to aircraft radios," in *Proc. Digital Avionics Syst. Conf. 2002*, Oct. 2002, pp.13E4-1--13E4-12.

[15] J. J. Ely, W. L. Martin, G. L. Fuller, T. W. Shaver, J. Zimmerman and W. E. Larsen, "UWB EMI to aircraft radios: field evaluation on operational commercial transport airplanes," in *Proc. Digital Avionics Syst. Conf. 2004*, 24-28 Oct. 2004, pp. 9.D.4-1--9.D.4-11.

[16] J. J. Ely, W. L. Martin, T. W. Shaver, G. L. Fuller, J. Zimmerman and W. E. Larsen, "UWB EMI to aircraft radios: field evaluation on operational commercial transport airplanes," NASA TP-2005-213606 Vol. 1, Jan. 2005.

[17] A. F. Molisch, J. R. Foerster and M. Pendergrass, "Channel models for ultrawideband personal area networks," *IEEE Wireless Commun.*, vol. 10, no. 6, pp. 14-21, Dec. 2003.

[18] A. F. Molisch, "Ultrawideband propagation channels: Theory, measurement, and modeling", *IEEE Trans. Veh. Technol.*, vol. 54, no.9, pp. 1528–1545, Sep. 2005.

[19] A. F. Molisch *et al.*, "A comprehensive standardized model for ultrawideband propagation channels," *IEEE Trans. Antennas Propag.*, vol. 54, no. 11, pp. 3151-3165, Nov. 2006.

[20] S. S. Ghassemzadeh, R. Jana, C. W. Rice, W. Turin and V. Tarokh, "Measurement and modeling of an ultra-wide bandwidth indoor channel," *IEEE Trans. Wireless Commun.*, vol. 52, no. 10, pp. 1786-1796, Oct. 2004.

[21] J. A. Dabin, A. M. Haimovich and H. Grebel, "A statistical ultra-wideband indoor channel model and the effects of antenna directivity on path loss and multipath propagation," *IEEE J. Sel. Areas Commun.*, vol. 24, no. 4, pp. 752-758, Apr. 2006.

[22] W. Q. Malik, D. J. Edwards and C. J. Stevens, "Frequency-dependent pathloss in the ultrawideband indoor channel," in *Proc. IEEE ICC 2006*, Jun. 2006, pp. 5546-5551.

[23] C. C. Chong and S. K. Yong, "A generic statistical-based UWB channel model for high-rise apartments," *IEEE Trans. Antennas Propag.*, vol. 53, no. 8, pp.2389-2399, Aug. 2005.

[24] W. Q. Malik, D. J. Edwards and C. J. Stevens, "Frequency dependence of fading statistics for ultrawideband systems," *IEEE Trans. Wireless Commun.*, vol. 6, no. 3, pp. 800-804, Mar. 2007.

[25] J. Karedal, S. Wyne, P. Almers, F. Tufvesson and A. F. Molisch, "A measurement-based statistical model for industrial ultra-wideband channels," *IEEE Trans. Wireless Commun.*, vol. 6, no. 8, pp. 3028-3037, Aug. 2007.

[26] V. Erceg *et al.*, "A model for the multipath delay profile of fixed wireless channels," *IEEE J. Sel. Areas Commun.*, vol. 17, no. 3, pp. 399-410, Mar. 1999.

Chapter 3
Characterization of UWB Channel Impulse Responses within the Passenger Cabin of a Boeing 737-200 Aircraft[2]

3.1 Introduction

The channel modeling committees of the IEEE 802.15.3a and 802.15.4a task groups devoted considerable effort to developing ultrawideband (UWB) wireless channel models applicable to systems that operate between 3.1 and 10.6 GHz under both line-of-sight (LOS) and non-line-of-sight (NLOS) conditions in residential, office, outdoor, industrial and body-centric environments at ranges up to 15 m. The standard channel models and channel impulse response (CIR) simulator that they developed allow fair comparison between alternative UWB systems over a range of representative channel conditions and deployment scenarios [1]-[3].

So that developers can effectively predict and compare the performance of UWB wireless communication systems in an environment of interest, both the shape and structure of the CIR, and the small-scale fading statistics experienced by individual multipath components (MPCs) within the CIR, must be accurately modeled. The results affect many important design issues, including selection of the number and placement of the fingers in rake receivers used to implement temporal diversity in spread spectrum systems and the selection of the guard-time and the design of cyclic prefixes used to mitigate multipath fading in OFDM systems. Because unclustered CIR models tend to overestimate link capacity if the MPCs are indeed clustered, it is useful to determine the extent to which clustering occurs [4]. The shape of the CIR also affects the performance of UWB ranging and positioning algorithms because it determines how well the

[2] A version of this chapter has been submitted for publication: S. Chiu, J. Chuang and D. G. Michelson, "Characterization of UWB channel impulse responses within the passenger cabin of a Boeing 737-200 aircraft."

algorithm will be able to detect the first arriving MPC. In practice, the CIR is often expressed in the form of a power delay profile (PDP) that excludes the phase information associated with each MPC.

UWB wireless systems hold great promise for: (1) enabling high data rate in-flight entertainment (IFE) and network access within the passenger cabin of an aircraft and (2) facilitating operations and maintenance through deployment of low power UWB-based sensor networks [5]. Early concerns that UWB-based systems would interfere with aircraft systems have largely been allayed by recent NASA studies [6],[7]. However, with its confined volume, cylindrical structure and high density of seating, an aircraft passenger cabin is fundamentally different from previously modeled UWB propagation environments. Although several research groups have made considerable progress in characterizing aircraft passenger cabins in support of deployment of conventional wireless technologies [8]-[14], and a few groups, including us, have reported results regarding large-scale aspects of UWB propagation in aircraft passenger cabins [15],[16], little has been reported concerning the detailed structure of UWB CIRs and the fading and correlation properties of their MPCs in such environments.

Here, we characterize the shape and structure of the UWB CIR, and the fading statistics and correlation properties of individual MPCs within the passenger cabin of a typical mid-sized airliner with the intent of developing a UWB CIR simulation model useful in analysis and design. Our results are based upon over 3300 complex channel frequency responses (CFRs) that we measured over the range 3.1 – 10.6 GHz aboard a Boeing 737-200 aircraft with an omnidirectional transmitting antenna mounted near the cabin ceiling and an omnidirectional receiving antenna mounted at selected locations throughout the cabin. We refer to this as a *point-to-multipoint* (p-to-mp) configuration. So that we could assess the spatial statistics of the UWB CIR, *i.e.*, the spatial average and the spatial correlation, we collected the CIRs across a 300-mm-by-300-mm spatial sampling grid with 50-mm spacing.

The remainder of this paper is organized as follows. In Section 3.2, we describe the configuration and calibration of our VNA-based channel sounder, our procedure for collecting channel frequency response (CFR) data in the aircraft and our measurement database. In Section 3.3, we present our proposed model for the shape and structure of the PDPs that we observed within the aircraft passenger cabin. In Section 3.4, we report

upon the fading statistics experienced by MPCs and the fading correlation between MPCs that are either: (1) in adjacent delay bins with the antenna at the same point on the sampling grid or (2) in the same delay bin but with the antenna at an adjacent point on the sampling grid. In Section 3.5, we describe how we modified the standard channel impulse response simulation code developed by IEEE 802.15.4a to generate CIRs representative of those observed in the aircraft passenger cabin environment and verified that its output is consistent with our measurement results. Finally, in Section 3.6, we summarize our key findings and contributions.

3.2 Measurement Approach

3.2.1 UWB Channel Sounder Configuration and Calibration

Our UWB channel sounder consists of an Agilent E8362B vector network analyzer (VNA), 4-m FLL-400 SuperFlex and 15-m LMR-400 UltraFlex coaxial cables, a pair of Electro-metrics 6865 UWB omnidirectional biconical antennas, a 0.5-m-by-0.5-m two-dimensional antenna positioner based upon Velmex BiSlide positioning slides, the tripods and fixtures that we used to mount the antennas at various locations throughout the cabin, and a laptop-based instrument controller equipped with a GPIB interface. During data collection, a MATLAB script running on the laptop controlled both the VNA and the two-dimensional positioner, and logged the received data.

We configured the VNA to sweep from 3.1 to 10.6 GHz in 6401 steps with an IF bandwidth of 3 kHz. The resulting displayed average noise level (DANL) is -107.2 dBm. In order to meet RF emission limits imposed upon us by the Research Ethics Boards at the University of British Columbia and the British Columbia Institute of Technology for the human presence study to be conducted as a follow-on to the present work, we set the transmit power to 5 dBm. The frequency sampling interval of 1.1716 MHz corresponds to a maximum unambiguous excess delay of 853 ns or a maximum observable distance of 256 m. The frequency span of 7.5 GHz corresponds to a maximum temporal resolution of 133 ps or a maximum spatial resolution of 40 mm. In Table 3.1, we give the principal elements of the system link budget at 3.1, 6.85 and 10.6 GHz, *i.e.*, the bottom, mid-point

and top of the UWB frequency band for a transmitter-receiver separation distance of 15 m. The average antenna gain refers to the average over all angles and directions. The path loss exponent of 2.2 used in the Table is the worst case that we observed both here and in our previous work [15]. We used through-line calibration to remove the frequency distortion introduced by the VNA and the coaxial cables that connect it to the transmitting and receiving antennas. A more detailed description of the through-line calibration is given in Appendix A.

Table 3.1. Link budget for the UWB channel sounder.

Links	Values		
	3.1 GHz	6.85 GHz	10.6 GHz
Transmitted Power	5 dBm	5 dBm	5 dBm
Transmit Cable Loss	1.2 dB	1.9 dB	2.4 dB
Average Transmit Antenna Gain	0 dBi	0 dBi	0 dBi
Path Loss at 15 m*	72.4 dB	79.9 dB	84.1 dB
Average Receive Antenna Gain	0 dBi	0 dBi	0 dBi
Receive Cable Loss	4.5 dB	7.0 dB	9.1 dB
Received Power	-73.1 dBm	-83.8 dBm	-90.6 dBm
Receiver Sensitivity	-107.2 dBm	-107.2 dBm	-107.2 dBm
System Margin	34.1 dB	23.4 dB	16.6 dB

*Calculated using a path loss exponent of 2

The transmitting and receiving antennas are vertically polarized, omnidirectional and identical. The measured channel response includes elements of both the actual response of the *propagation channel* and the response of the transmitting and receiving antennas. This result is often referred to as the response of the *radio channel*. In order to perfectly de-embed the propagation channel response from the radio channel response, one would need to measure the frequency-dependent double-directional channel response that accounts for the angle-of-departure (AoD) and angle-of-arrival (AoA) of each ray and the frequency-dependent three-dimensional radiation pattern of each antenna [2]. Implementing the required measurement setup within the confines of the aircraft passenger cabin would be problematic, however.

The antenna calibration problem is simplified considerably if we can assume that the environment is rich with scatterers so that the physical MPCs arrive from all possible directions and each resolvable MPC includes many physical MPCs. Because the directivity of any antenna averaged over all directions would be unity for all frequencies, the measured CIR would be independent of the radiation patterns of the transmitting and receiving antennas. Moreover, the CIR would take on a characteristic form in which

every delay bin would contain MPCs and every MPC would exhibit Rayleigh fading. In such cases, after appropriate account has been taken for the frequency-dependent return loss of the antennas, the measured channel response would be equivalent to the actual channel response.

As we shall show, the density of the MPCs in the CIRs and the Rayleigh fading distribution displayed by each resolvable MPC that we measured in the aircraft passenger cabin suggests that many of these conditions are at least partly met. Because the receiving antenna pattern is essentially uniform in the horizontal plane, the effective antenna pattern given by the convolution of the free space antenna pattern and the AoA distribution in that plane is also uniform regardless of the actual AoA distribution. Thus, this condition is automatically met. However, the receiving antenna pattern in the vertical plane is decidedly non-uniform so the effective antenna pattern will be uniform only if the actual AoA distribution is uniform. Previous work in conventional indoor environments has shown that the AoA distribution in the vertical plane broadens considerably as the size of the enclosed space becomes smaller [17]. While this suggests that the AoA distribution in the vertical plane within the aircraft is likely to be broad, it is not likely to be uniform. Other previous work using the same biconical antennas found remarkable differences in the spatial correlation between 2 and 12 GHz, which were also related to differences in the antenna patterns, particularly in the vertical plane [18]. In such work, when the frequency was increased, the spatial correlation was increased as well (for the same wavelength), which indicated higher directivity on radio channels, and lower delay spread. Thus, although we believe that our measured CIR provides a reasonable indication of the actual CIR, our results strictly apply to the radio channel and slightly different results may be obtained if other transmitting and receiving antennas with different radiation patterns in the vertical plane are used.

3.2.2 Data Collection

We collected our CFR measurements within the passenger cabin of a Boeing 737-200 aircraft. The cabin, which can seat over 100 passengers, is 3.54 m in width, 2.2 m in height and 21 m in length of which 18 m actually includes passenger seating. Plan and cross-sectional views of the passenger cabin are shown in Figure 3.1(a) and (b),

respectively. Other modern mid-sized airliners, such as the CRJ series from Bombardier, the A320 family from AirBus Industries and the ARJ21 family from ACAC, have similar cross-sections. Only the lengths of the passenger cabins, which range from 12 to 43 m, are appreciably different.

Here, we have considered a p-to-mp wireless system configuration in which the transmitting antenna is mounted along the centerline of the cabin ceiling in the manner of an access point and the receiving antenna is placed at the headrest, armrest and footrest level of the passenger seats throughout the aircraft, as suggested by Figure 3.1 (a) and (b). The different receiving antenna mounting positions not only represent typical use cases such as using a cell phone (at headrest level), a laptop (at armrest level) or devices that might be contained in passengers' carry-on baggage (at footrest level) but also represent both LOS (at the headrest and aisle armrest) and NLOS (at the outboard armrest and footrest) channels.

In Section 3.4, we present MPC fading statistics within a local area that we estimated using methods similar to those described in [3]. Although standard practice would be to move the receiving antenna across the spatial sampling grid, this is difficult to do when the antenna is mounted close to the passenger seats. Because moving the transmitting antenna instead was shown to yield good results in [4], we did so here, too. With the receiving antenna mounted at headrest, armrest and footrest levels, we collected 49 spatial samples by mounting the transmitting antenna at ceiling level at row 2 and moving it across a 7-by-7 grid with a spacing of 50 mm, as shown in Figure 3.1 (a). By setting the spacing equal to half of the wavelength of the lowest frequency, we sought to ensure that the spatial samples are independent. This, however, does not allow unambiguous resolution of the direction of a given ray, which requires the spacing be equal to half of wavelength of the highest frequency [2]. Previous work suggests that: (1) approximately nine samples are sufficient to average out the small-scale fading and permit the true shape of the PDP to be recovered [19], and (2) approximately 50 samples are sufficient to determine the underlying fading distribution [2]. Here, we have elected to use 49 spatial samples per measurement location because it permits use of a symmetrical 7-by-7 sampling grid.

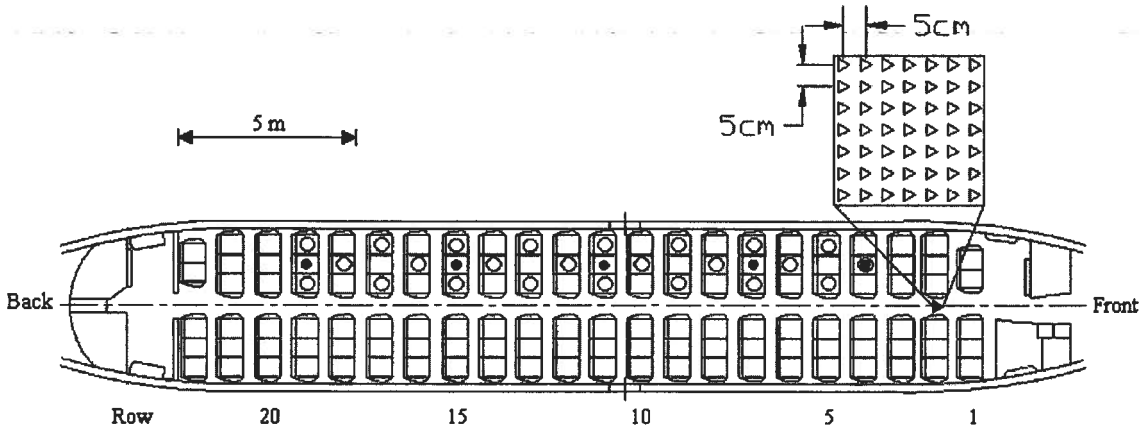

(a)

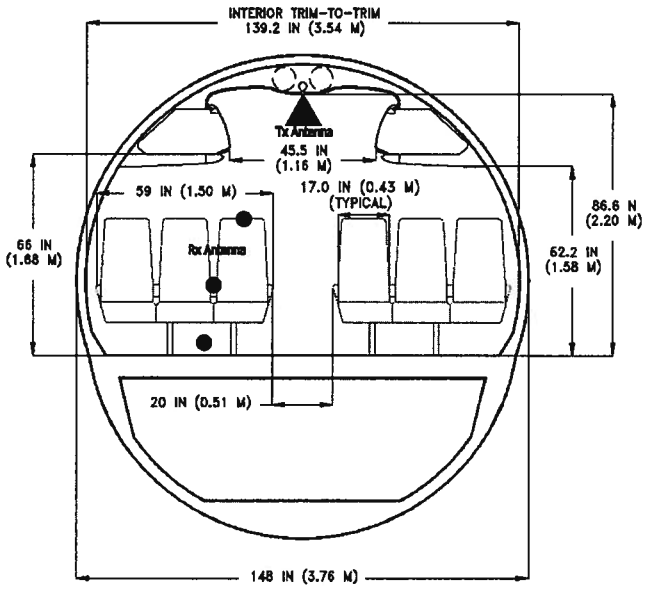

(b)

Figure 3.1. Locations of the transmitting antenna (▶) and receiving antennas (O = headrest and armrest, ● = footrest) within a Boeing 737-200 aircraft in (a) plan and (b) cross-section view.

3.2.3 Consistency Checks

Before we collected production data, we conducted a series of development runs in order to: (1) verify that the channel is static and show that we could exploit the bilateral and translational symmetry inherent in the cabin layout to dramatically reduce the number of measurements needed to characterize propagation within the aircraft, and (2)

verify that the shape and structure of the CIRs are consistent within a local area and that any differences between the CIRs that we observed over that local area are mostly due to multipath fading of individual MPCs. We did so by comparing: (1) the shapes of the average power delay profiles (APDPs) based upon CIRs measured at nine points on a 100-mm-by-100-mm grid with the receiving antenna mounted at rows 4, 7, 11, 15 and 19, and (2) the mean excess delay, τ_{mean}, and RMS delay spread, τ_{rms}, based upon CIRs measured at 49 points on a 300-mm-by-300-mm grid with the receiving antenna mounted at rows 4, 11 and 19. The mean excess delay and RMS delay spread were calculated using a threshold of 25 dB below the peak scattered component. Although it is difficult to set an absolute criterion for consistency, support for the conjecture is given by: (1) visual inspection of the APDPs and the plot of RMS delay spread vs. distance in Figure 3.2 and (2) observation that the standard deviations of the mean excess delay and RMS delay spread over all measurement locations are, on average, less than 1.5 and 1 ns, respectively. In Section 3.3.1, we describe the details of the processing steps that we followed when estimating APDPs from measured CIRs.

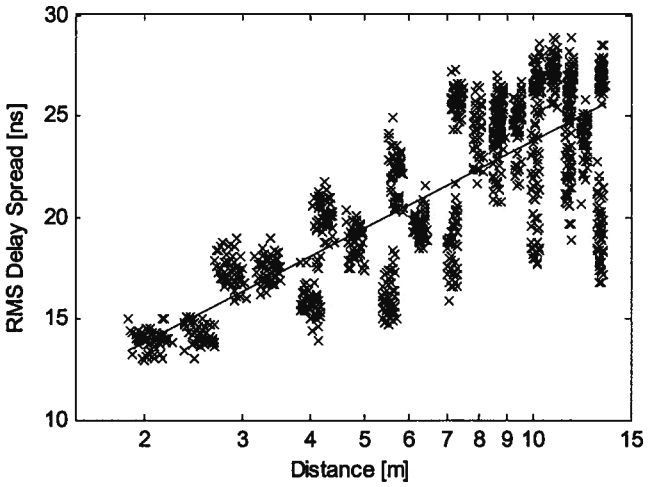

Figure 3.2. The rms delay spread as a function of distance when the receiving antenna is mounted on the headrest.

3.2.4 Measurement Database

Our measurement database includes both development and production data. During our development runs, we collected two sets of data. In the first set, we considered three

transmitter locations and over 50 receiver locations. For selected paths, we collected multiple sweeps in succession and verified that: (1) the channel is static and (2) our channel sounder yielded consistent results. In the second set, we used a single transmitter location and we measured the channel response at five locations across either 9-point or 49-point spatial sampling grids with the receiving antenna placed at headrest, armrest and footrest levels. The two sets combine to yield over 700 CFRs.

During our production runs, we placed the receiving antenna at headrest, armrest and footrest levels throughout the port side of the cabin. When we mounted the receiving antenna at the headrest and armrest, we collected the CFRs at 24 different locations and when we mounted the antenna at the footrest level, we collected CFRs at five locations. These measurement locations are shown in Figure 3.1. In both cases, we used a 49-point spatial sampling grid, yielding 2597 CFRs. In total, our development and production runs yielded over 3300 CFRs.

3.3 Shape and Structure of the Power Delay Profile

3.3.1 Initial Processing of the Channel Impulse Response

Whether measured in the time or frequency domain, a measured channel response has a finite bandwidth that is determined by either the instrument or the measurement process. The result is equivalent to convolving the true CIR with a sinc function whose duration is inversely proportional to the bandwidth of the measurement. Before processing a measured CIR, one must first remove the effects of the finite bandwidth either by windowing or deconvolution. Here, we applied a Kaiser window with $\beta = 7$ to the CFRs in order to suppress dispersion of energy into adjacent delay bins. We converted the CFRs into complex baseband CIRs by applying an inverse Fourier transform (IFT).

We normalized the CIRs so that they contained unit energy and then removed the initial propagation delay. For LOS channels, we define the start of the CIR as the first

MPC that arrives within 10 dB of, and 10 ns before, the peak MPC. For NLOS channels, we define the start of the CIR as the first MPC that arrives within 10 dB of, and 50 ns before, the peak MPC. We removed the propagation delay, τ_0, by setting the start time of the first arriving MPC to zero. After we removed the initial delays, we aligned the first arriving MPCs in each PDP and averaged the MPCs directly in the time domain to yield the small-scale APDP [20],[21]. Unless otherwise indicated, we removed all MPCs with amplitudes that are more than 25 dB below the peak MPC before we extracted any model parameters. These criteria are based upon the techniques described in [4].

As others have noted, the fine delay resolution of a UWB PDP may cause a physical MPC that arrives at a certain delay when observed at a certain grid point to fall in a different delay bin when observed at another grid point [2][21]. Although the process of averaging will smear the PDP, the result will affect dense single cluster PDPs (in which a resolvable MPC consists of several physical MPCs) differently than sparse multi cluster PDPs (in which a resolvable MPC may correspond to a single physical MPC and many delay bins are empty). Following the method described in [20], we reduced our delay resolution by a factor of 10, *i.e.*, from 133 ps to 1.33 ns in order to reduce the smearing effect. The results show that the APDP with reduced time resolution presents the same shape and structure as the original APDP. A more detailed description of the smearing effect is given in Appendix B.

3.3.2 IEEE 802.15 CIR Models

Our next task was to identify the channel impulse response model that offers the best description of time dispersion within the aircraft passenger cabin. We began by considering the two standard UWB channel models that were adopted by the IEEE 802.15.3a and 4a task groups [1][3]. The sparse multi-cluster model is based upon the SV model given by

$$h(t) = \sum_{l=1}^{L} \sum_{k=1}^{K} a_{k,l} \exp(j\phi_{k,l}) \delta(t - T_l - \tau_{k,l}). \tag{3.1}$$

Here, the MPCs are modeled as Dirac delta functions, $\delta(.)$, and $a_{k,l}$ and $\phi_{k,l}$ are the amplitude and phase of the kth MPC in the lth cluster, L is the total number of clusters in the CIR and K is the total number of MPCs within the lth cluster. T_l and $\tau_{k,l}$ represent the

arrival time of the lth cluster and the kth MPC in the lth cluster, respectively. Because path loss is frequency dependent, the MPCs are distorted as described in [2][3]. IEEE 802.15.4a used a modified form of the SV model that accounts for such distortion to describe the UWB CIRs in six of the eight scenarios they considered. The shape of the corresponding PDP is described by the product of two exponential functions,

$$E\left\{\left|a_{k,l}\right|^2\right\} \propto \exp(-T_l/\Gamma)\exp(-\tau_{k,l}/\gamma_m), \tag{3.2}$$

where Γ and γ_m are the inter-cluster and intra-cluster decay constants, respectively.

The dense single-cluster model is used to describe dense scattering environments, *e.g.*, the office and industrial environments under NLOS conditions. In these environments, one can no longer discern clustering within the CIR and the envelope of the PDP can be described as

$$E\left\{\left|a_{k,l}\right|^2\right\} \propto \left(1-\chi\exp\left(\frac{-\tau_{k,l}}{\gamma_{rise}}\right)\right)\exp\left(\frac{-\tau_{k,l}}{\gamma_1}\right), \tag{3.3}$$

where χ denotes the attenuation of the first component, γ_{rise} determines how fast the PDP rises to its local maximum and γ_1 represents the decay at later times [3]. If the scattering environment is sufficiently dense, *e.g.*, an industrial NLOS environment, then every time resolution bin contains an MPC. Accordingly, the PDP can be modeled as a tapped delay line with a fixed arrival time, Δt, that is given by the inverse of the signal bandwidth. Where scatterers are less dense but the single cluster response still applies, *e.g.*, an office NLOS environment, then the convention is to model the arrival rate of the MPCs by a Poisson distribution [3].

3.3.3 Modeling the Shape of the Power Delay Profile

In Figure 3.3(a), we present a typical APDP of a LOS channel based upon measurement data collected when the transmitting antenna was mounted near the cabin ceiling and the receiving antenna was mounted on the headrest of a passenger seat. When the receiving antenna is mounted on the armrest of an aisle seat, the resulting channel is also LOS and the CIR resembles that of the headrest. As in the case of industrial LOS channels, the MPCs form a continuous exponential decay with no distinct clusters. In many cases, we observed a few strong spikes or impulses early in the APDP, as described below.

In Figure 3.3(b) and (c), we present typical APDPs observed over NLOS channels where the receiving antenna was mounted on an outboard armrest or footrest, respectively. Similar to industrial NLOS channels, both cases display a gentle rise before reaching the local maximum described by the dense single cluster model. We also observe that the footrest case exhibits a slower rise time than the armrest case. This is likely because the initial MPCs in the footrest case encounter more and/or denser obstacles and thus are more severely attenuated than the initial MPCs in the armrest case.

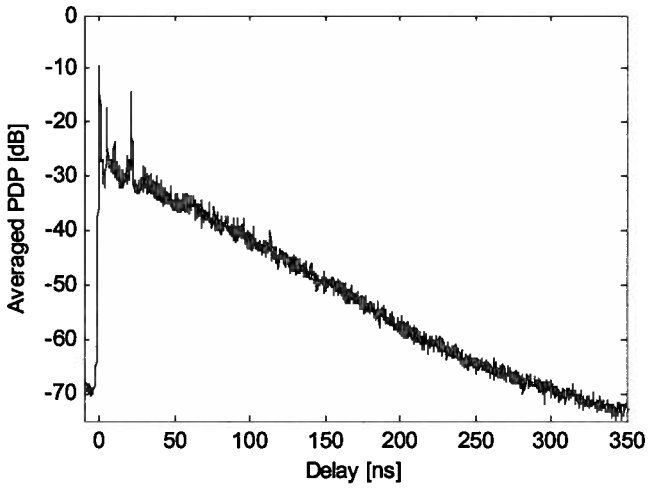

(a)

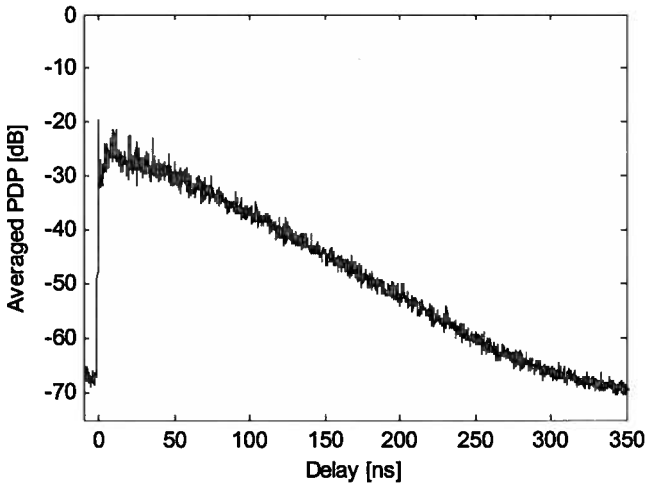

(b)

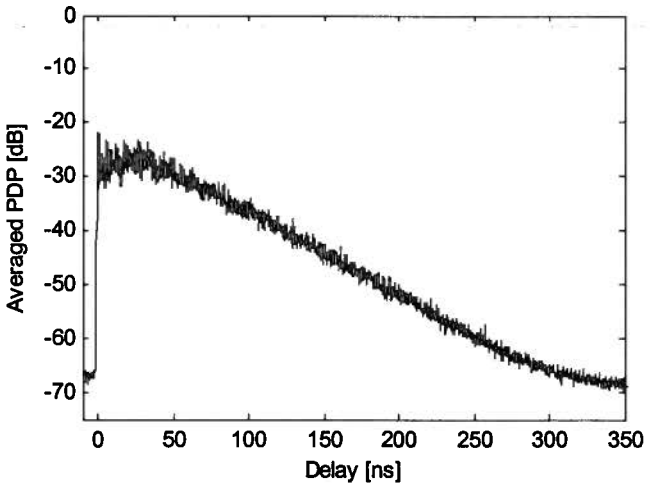

(c)

Figure 3.3. The spatially averaged PDP observed when the receiving antenna is mounted at row 19 on (a) the headrest, (b) the outboard armrest and (c) the footrest.

Based upon our measurement results, we propose the following model for the PDP of LOS channels in aircraft passenger cabins, *i.e.,* where the receiving antenna is mounted on a headrest or aisle armrest. First, we model the shape of the scatter components of the APDP as a simple exponential decay,

$$E\left\{|a_k|^2\right\} \propto \exp\left(\frac{-\tau_k}{\gamma}\right), \tag{3.4}$$

where γ is the exponential decay constant. Next, we model the excess amplitude of the LOS MPC above the exponential decay curve at the propagation delay, τ_0. In linear units, we define the excess amplitude as

$$\Delta = P_{\text{LOS}} / \exp\left(\frac{-\tau_0}{\gamma}\right), \tag{3.5}$$

where P_{LOS} is the power in the LOS component and the denominator is the expected power at the beginning of the exponential decay described using equation (3.4).

On LOS channels, we often observe random impulses within the first 30 ns of the initial response. We suspect that they are due to specular reflection from the cabin bulkhead or floor and note that similar impulses have been observed in industrial environments [21]. The ratios of the energy in the initial (LOS) and delayed impulses in the APDPs that we observed when the receiving antenna is mounted on the headrest are

shown in Figure 3.4. The delayed impulses contain only a very small fraction of the energy in the CIR and, on average, carry only 15% of the energy in the LOS component. The development of a statistical model that captures their occurrence, amplitude distribution and arrival rate would require much more data than we have available. Accordingly, we leave further efforts to model them for future study.

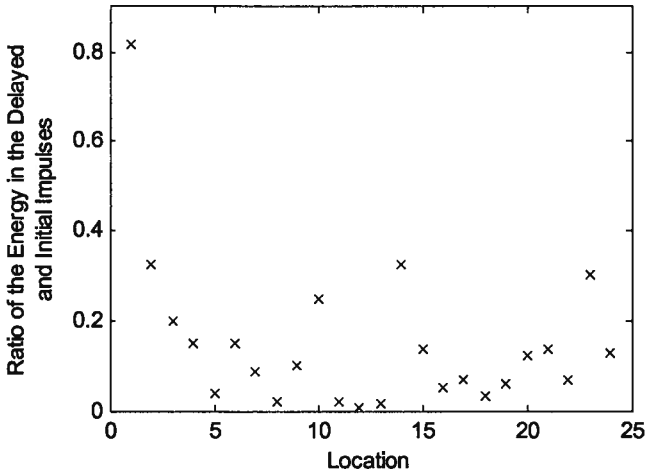

Figure 3.4. Ratio of the energy in the delayed and initial specular components.

Although the IEEE 802.15.4a channel modeling committee did not account for the distance dependence of the CIR model parameters, we have done so here. In UWB scenarios, increases in rms delay spread with distance are generally associated with a decrease in the SV model's cluster decay constant, Γ, or the single cluster model's exponential decay constant, γ. Using methods similar to those employed in [22] and [23] we model the variation in the exponential decay constant γ and the excess amplitude Δ with distance for LOS channels by

$$\gamma = \gamma_0 + \beta_\gamma \cdot 10\log_{10} d + X_\gamma \tag{3.6}$$

and

$$10\log_{10}\Delta = 10\log_{10}\Delta_0 - \beta_\Delta \cdot 10\log_{10} d + X_\Delta, \tag{3.7}$$

where γ_0 and $10\log_{10}\Delta_0$ are the intercepts, β_γ and β_Δ are the slopes, X_γ and X_Δ are zero-mean Gaussian random variables with standard deviations σ_γ and σ_Δ, respectively, and d is the distance between the transmitting and receiving antennas. The regression lines given by (6) and (7) are shown in Figure 3.5(a) and (b), respectively. The regression lines

for the exponential decay constant for the aisle and non-aisle cases are essentially identical so we have treated the two cases as a single case in Figure 3.5 (a). The regression lines for the excess amplitude of the LOS component for aisle and non-aisle cases are quite different so we have presented them separately in Figure 3.5 (b). Both X_γ and X_Δ are generally well described by zero-mean normal distributions in ns and dB, respectively, and pass the Anderson-Darling goodness-of-fit test at the 5% significance level in most cases and at the 1% level in all cases except one. The bell-shaped distribution presented by X_Δ in the aisle-headrest case is slightly distorted and does not pass. A summary of the LOS channel model parameters that we extracted is given in Table 3.2.

For NLOS channels, *i.e.*, the receiving antenna mounted upon an outboard armrest or a footrest, we modeled the envelope of the PDP using equation (3.3). We describe the distance dependence of the parameters by

$$\chi = \chi_0 - \beta_\chi \cdot 10\log_{10} d + X_\chi, \tag{3.8}$$

$$\gamma_{rise} = \gamma_r + \beta_r \cdot 10\log_{10} d + X_r, \tag{3.9}$$

and

$$\gamma_1 = \gamma_0' + \beta_\gamma' \cdot 10\log_{10} d + X_\gamma'. \tag{3.10}$$

In (3.8), (3.9) and (3.10), χ_0, γ_r and γ_0 are the intercepts and β_χ, β_r and β'_γ are the slopes. X_χ, X_r and X'_γ are zero-mean Gaussian random variables with standard deviations, σ_χ, σ_r and σ'_γ, respectively, and d is the distance between the transmitting and receiving antennas. A summary of the NLOS channel model parameters that we extracted is given in Table 3.3.

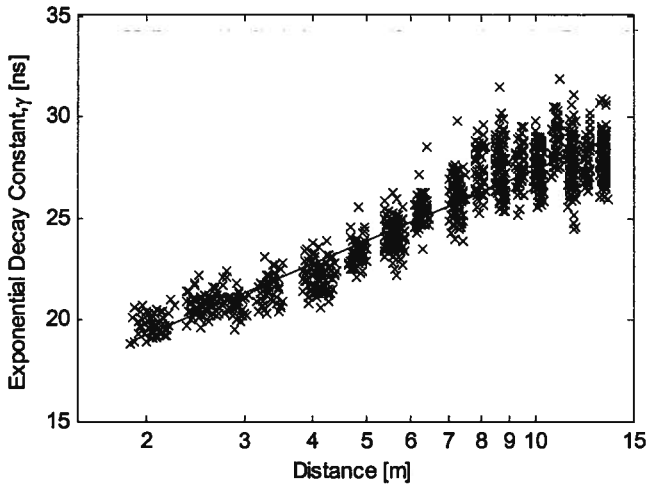

(a)

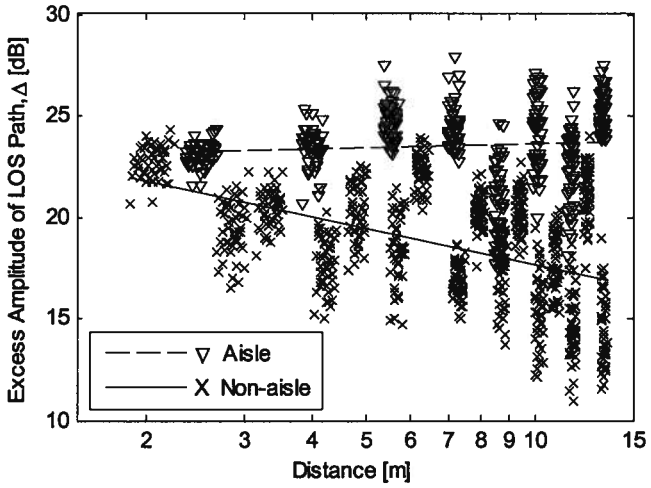

(b)

Figure 3.5. Shape parameters of the power delay profile as a function of distance for headrest channels: (a) the exponential decay constant, γ, and (b) the excess amplitude of the LOS path, Δ.

Table 3.2. Power delay profile model parameters (headrest and aisle armrest).

Model Parameters	Headrest		Armrest
	Aisle	Others	
γ_0	15.75 ns		16.02 ns
β_γ	1.16		1.23
σ_γ	1.10 ns		1.22 ns
Δ_0	23.03 dB	23.54 dB	15.40 dB
β_Δ	-0.06	0.59	0.58
σ_Δ	1.95 dB	2.47 dB	2.14 dB
d	2 to 13 m	2 to 13 m	2 to 13 m

Table 3.3. Power delay profile model parameters (outboard armrest and footrest).

Model Parameters	Armrest	Footrest
χ_0	0.116	-0.143
β_χ	0.0223	0.0629
σ_χ	0.0397	0.0242
γ_r	4.86 ns	-6.34 ns
β_r	0.697	2.61
σ_r	0.657 ns	0.409 ns
γ_0	12.7 ns	13.7 ns
β'_γ	1.54	1.50
σ'_γ	0.648 ns	1.03 ns
d	2 to 13 m	2 to 13 m

3.4 Small-Scale Fading and Interdependence of MPCs

3.4.1 Small-Scale Fading

We determined the distribution that best describes the small-scale fading of individual MPCs by processing the CIRs that we sampled at 49 points within a 300-mm x 300-mm grid, extracting the amplitudes of the taps over all delays, computing the corresponding CDFs, and comparing them to standard distributions. In the past, others have found that the small scale fading distributions observed in residential environments are well approximated by a lognormal distribution [23] while others have found that a Nakagami distribution fits well [3]. However, our results show that the small-scale fading distribution of individual MPCs in the aircraft environment is well-approximated by a Rayleigh distribution. This is a reasonable outcome given that the aircraft passenger cabin is a dense scattering environment and it is likely that each delay bin or MPC consists of several rays. Moreover, others have reported that small-scale fading follows Rayleigh statistics in other dense scattering environments such as industrial plants [21].

We refined our understanding of the distribution of small-scale fading by fitting it to the more general Nakagami distribution that has been used to model small-scale fading in other UWB environments. The Nakagami distribution is given by

$$f_X(x) = \frac{2}{\Gamma(m)}\left(\frac{m}{\Omega}\right)^m x^{2m-1}\exp\left(-\frac{m}{\Omega}x^2\right), \tag{3.11}$$

where $m \geq ½$ is the Nakagami m-factor (or the shape parameter of the distribution), $\Gamma(m)$ is the Gamma function, and Ω is the mean-squared value of the amplitude (or the spread parameter of the distribution). For each delay bin, we estimated the m-factor of the Nakagami distribution by applying the inverse normalized variance estimator [24] to the 49 spatial samples. The estimate of the m-factor is given by

$$\hat{m} = \frac{\mu_2^2}{\mu_4 - \mu_2^2}, \tag{3.12}$$

where

$$\mu_k = \frac{1}{N}\sum_{i=1}^{N} |h_i|^k, \tag{3.13}$$

and where N is the number of spatial sampling points and h_i is the complex amplitude of the ith path.

A scatter plot of the m-factor estimates for the first 200 ns of delay bins for the receiving antenna mounted on the headrest at row 19 is shown in Figure 3.6(a). Although a few MPCs at the beginning of the PDP (typically when the delay is less than 30 ns) exhibit large m-factors, the vast majority of the 1501 MPCs shown in Figure 3.6(a) exhibit m-factors of approximately 1 and, as noted previously, their fading distributions are therefore well approximated by Rayleigh statistics. The fading distributions of MPCs observed at the armrest and footrest are also well approximated by Rayleigh statistics.

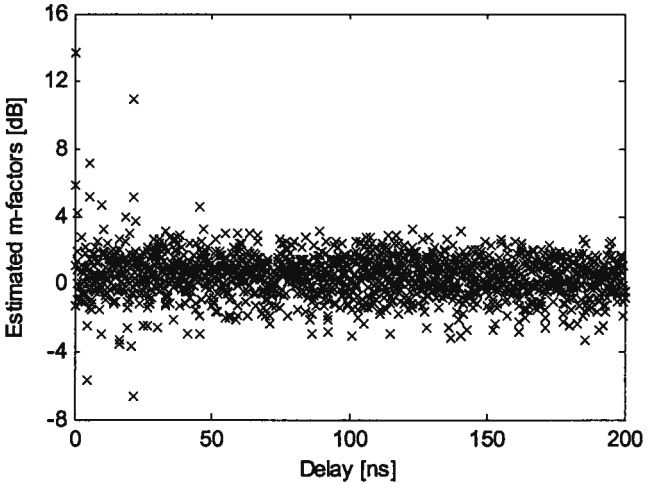

(a)

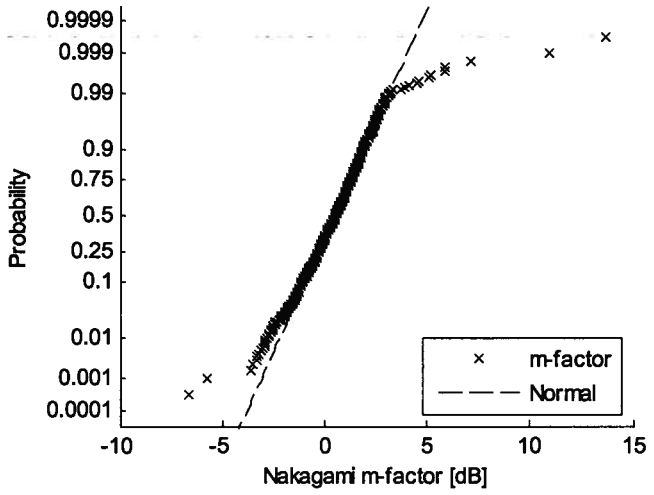

(b)

Figure 3.6. Estimates of the m-factors (in dB) that describe the MPC fading distribution when the receiving antenna was mounted on the headrest of row 19: (a) as a function of delay and (b) expressed as a CDF and compared to the best fit normal distribution.

Other researchers have found that the m-parameter follows a lognormal distribution given by

$$f(m) = \frac{1}{\sigma_m x\sqrt{2\pi}} \exp\left(-\frac{(\ln m - \mu_m)^2}{2\sigma_m^2}\right), \tag{3.14}$$

where μ_m and σ_m are the mean and variance of the m-factors and are by convention given in decibels [19][21]. The initial impulses in the PDP for the LOS channel are characterized by a deterministic m-factor, m_0, which is typically much larger than m at other delays. In [3], it was found that both μ_m and σ_m may depend on the delay of the MPC within the CIR. As shown in Figure 3.6(a), we did not find any evidence of such dependence. We also observe that m_0 tends to decrease with increasing distance, while μ_m and σ_m are effectively independent of distance. Accordingly, we have characterized μ_m and σ_m simply by taking the average over all distances in each case and we model m_0 by

$$m_0(d) = m_{00} - \beta_{m0} \cdot 10\log_{10} d + X_{m0}, \tag{3.15}$$

where m_{00} is the intercept and β_{m0} is the slope, X_{m0} is a zero-mean Gaussian random variable with standard deviation σ_{m0}, and d is the distance between the transmitting and receiving antennas. The small-scale fading parameters that we extracted are summarized in Table 3.4. The CDF of the estimated m-factors is compared to the CDF of the best-fit

lognormal distribution for the case of the receiving antenna mounted on the headrest at row 19 in Figure 3.6(b). The 12 strongest taps (out of 1501 taps in total) deviate greatly from the lognormal distribution. They correspond to a few strong impulses that arrived near the leading edge of the response and we consider them to be outliers.

Table 3.4. Small-scale fading parameters.

Model Parameters	Headrest	Armrest		Footrest
		Aisle	Outboard	
μ_m	0.311 dB	0.247 dB	0.342 dB	-0.194 dB
σ_m	1.17 dB	1.21 dB	1.16 dB	1.23 dB
m_{00}	20.83 dB	21.98 dB	–	–
β_{m0}	0.702	0.707	–	–
σ_{m0}	2.47 dB	2.74 dB	–	–

3.4.2 Interdependence of MPCs

The fading correlation between MPCs that are either: (1) in adjacent delay bins with the antenna at the same point on the sampling grid, which we shall refer to as temporal correlation, or (2) in the same delay bin but with the antenna at other points on the sampling grid, which we shall refer to as spatial correlation, is of interest for several reasons. First, if the MPCs in *adjacent* delay bins cannot be modeled as independent random variables, then the complexity of the channel model will increase dramatically. Second, we want to verify that the fading observed at a *given* delay at each point in the spatial sampling grid is reasonably independent from that observed at other points in the grid so that we have confidence that we have a sufficient number of independent samples to estimate the fading statistics. Third, some have recently proposed that WiMedia UWB systems be equipped with antenna arrays so that the direction-of-arrival of incoming signals can be estimated and adaptive array techniques can be used to reduce the susceptibility of the system to interfering signals. UWB-MIMO systems have also been proposed. Knowledge of the spatial correlation properties of the channel is required in order to determine the required antenna element spacing [25]. While the spatial correlation results presented here provide a useful first indication, our grid spacing of 5 cm does not allow unambiguous resolution of angular components at higher UWB frequencies. Thus, practical design of adaptive array antennas to be used at higher UWB

frequencies will require that our measurements be supplemented by new data with finer spatial resolution.

The temporal correlation is given by

$$\rho_{temp\,a_{k,k+1}} = \frac{E\{(a_k - \bar{a}_k)(a_{k+1} - \bar{a}_{k+1})\}}{\sqrt{E\{(a_k - \bar{a}_k)^2\}E\{(a_{k+1} - \bar{a}_{k+1})^2\}}}, \tag{3.16}$$

where $E\{.\}$ denotes expectation, a_k and a_{k+1} are the amplitudes of the kth and $(k+1)$th MPC respectively, as observed in the CIRs measured at all 49 points in the grid, and $\bar{a}_k$ and $\bar{a}_{k+1}$ are the corresponding mean values across all 49 points [4]. For all receiving antenna positions and locations considered, the mean value of the temporal correlation for the different delay taps is 0.13 with no value exceeding 0.56. Because the correlation between MPCs in adjacent delay bins is low, we can reasonably treat the path amplitudes at each delay as uncorrelated independent random variables.

The spatial correlation between the MPCs at a given delay is given by

$$\rho_{spat}(k,d) = \frac{E\{(p_{n,k} - \bar{p}_k)(p'_{n,k} - \bar{p}'_k)\}}{\sqrt{E\{(p_{n,k} - \bar{p}_k)^2\}E\{(p'_{n,k} - \bar{p}'_k)^2\}}}, \tag{3.17}$$

where $p_{n,k}$ and $p'_{n,k}$ are the amplitudes of the kth MPC in the PDPs that are observed at the nth pair of points that are separated by a distance d. The parameters $\bar{p}_k$ and $\bar{p}'_k$ are the mean amplitudes seen at all pairs of observation points that satisfy the above criteria [26]. In Figure 3.7, we show the spatial correlation coefficient as a function of separation distance averaged over all delay bins. When the separation distance is greater than or equal to 50 mm, both the mean and standard deviation of the spatial correlation coefficient are always less than 0.1 and 0.3, respectively. Thus, we can reasonably assume that the path amplitudes observed at any two grid points at the same delay are uncorrelated and that our grid spacing of 50 mm was sufficient for obtaining independent samples for fading statistics estimation. Although this result implies that UWB-MIMO arrays can be realized within aircraft passenger cabins with antenna spacings as small as 50 mm, further measurements will be required to determine if an even smaller spacing is practical.

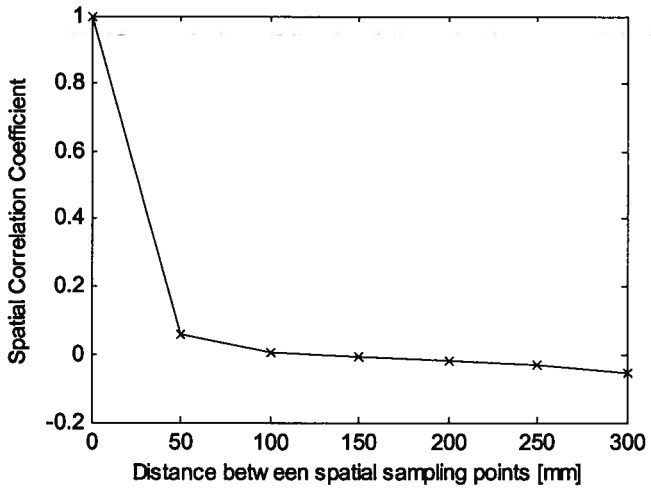

Figure 3.7. Spatial correlation averaged over delay as a function of distance between spatial sampling points when the receiving antenna is mounted on the headrest of row 19.

3.5 A Simulation Model for UWB CIRs in an Aircraft Passenger Cabin

With their final report, the IEEE 802.15.4a channel modeling committee released a MATLAB-based simulation code that uses their models to generate CIRs typical of those encountered in residential, office, outdoor and industrial environments. We have modified their channel simulation code so that it can be used to generate UWB CIRs typical of p-to-mp scenarios with the transmitting antenna located at the cabin ceiling and the receiving antenna located at the headrest, armrest and footrest level in the aircraft passenger cabin environment. In our version of the channel simulation code, scenarios AC 1 through AC 4 refer to transmission from the cabin ceiling to the headrest, aisle armrest, outboard armrest and footrest, respectively.

The four main parts of the IEEE 802.15.4a code are concerned with: (1) assignment of the channel model parameters, (2) generation of CIRs using random processes that simulate: (a) the arrivals of the clusters and rays and (b) the path amplitudes based upon the shape of the PDP and the small-scale fading distribution, (3) prediction of the frequency dependent path loss, and (4) conversion of the result from continuous time to

discrete time. The original simulator is based upon statistics that have been averaged over distance.

Here, we use our new models to account for distance explicitly. The headrest and aisle armrest scenarios correspond to LOS channels and the APDPs are modeled by a single exponential decay as described by (3.4)-(3.7). The outboard armrest and footrest scenarios correspond to NLOS channels and are modeled using (3.3) and (3.8)-(3.10). Finally, we have modeled the small-scale fading of individual MPCs using (3.14) and (3.15). To verify that the modified channel simulator produces reasonable results, we generated CIRs using parameters for a given distance and then compared the results with the measured CIRs observed at the same distance. As shown in Figure 3.8, the measured and simulated APDPs for both the headrest and outboard armrest scenarios compare well. As shown in Figure 3.9, the CDFs of the rms delay spreads associated with measured and simulated CIRs over all ranges between 2 and 13 m also compare well. The modified version of the channel simulator code is given in Appendix C.

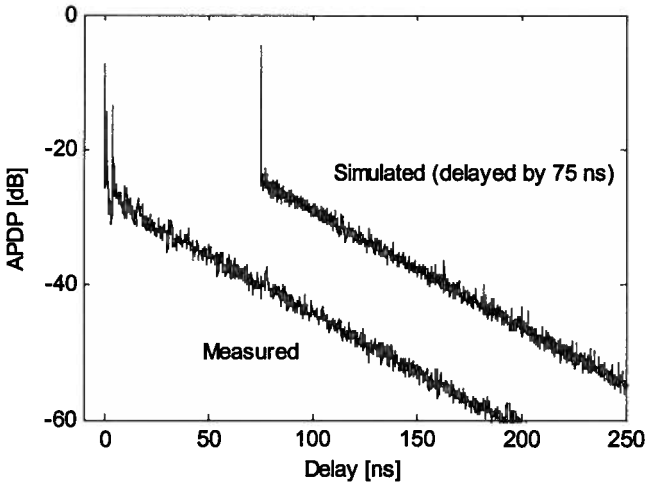

(a)

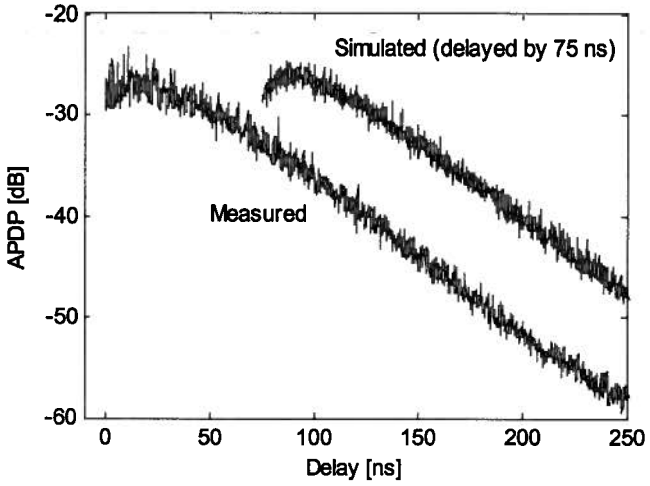

(b)

Figure 3.8. Comparison of the measured and regenerated APDP for (a) headrest and (b) footrest.

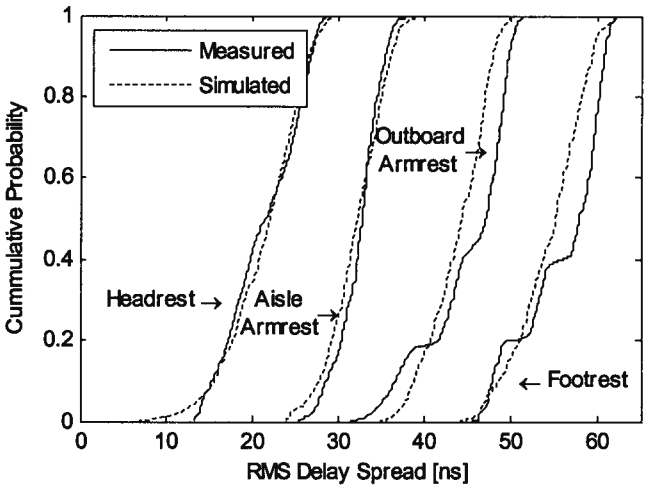

Figure 3.9. Distributions of simulated and measured rms delay spreads for different receiver mounting positions. For clarity, the distributions for the aisle armrest, outboard armrest and footrest cases are offset by 10, 20 and 30 ns, respectively.

3.6 Conclusions

Based upon channel response data collected within the passenger cabin of a typical mid-size airliner in p-to-mp configurations, we have proposed a pair of statistical models

that describe the UWB channel impulse responses observed over LOS and NLOS channels, respectively. The models describe the shape of the power delay profile, characterize the fading experienced by individual multipath components and give the spatial and delay dependence of the correlation between fading on adjacent MPCs.

We have observed the following trends: (1) For LOS channels, *e.g.*, cabin ceiling to headrest or aisle armrest, the shape of the PDP generally follows IEEE 802.15.4a's dense single-cluster model, but with negligible rise time and, on many occasions, one or more impulses or spikes within 30 ns of the leading edge of the response. (2) For NLOS channels, *e.g.*, cabin ceiling to outboard armrest or footrest, the shape of the PDP follows IEEE 802.15.4a's dense single-cluster model and the rise time is up to 10 ns. (3) The mean and variance of the exponential decay constant (hence the rms delay spread) tends to increase with path length and as the receiving antenna drops from the headrest to the footrest. (4) Small-scale fading of MPCs tends to follow a Nakagami distribution with a lognormally-distributed m-parameter that is close to 0 dB (which corresponds to Rayleigh fading) with a small variance, as has been found in other rich scattering environments.

In most cases, our results take the form of the parameters of the corresponding models recommended by the IEEE 802.15.4a channel modeling committee and can be used directly in simulations of UWB propagation in an aircraft interior. Moreover, we have modified the standard channel impulse response simulation code developed by IEEE 802.15.4a so that it can generate CIRs representative of those observed in the aircraft passenger cabin environment. Accordingly, our results will assist: (1) those who are planning UWB deployments and field trials in aircraft and (2) those who need to simulate UWB systems in aircraft using realistic channels.

3.7 References

[1] A. F. Molisch, J. R. Foerster and M. Pendergrass, "Channel models for ultrawideband personal area networks," *IEEE Wireless Commun.*, vol. 10, no. 6, pp. 14-21, Dec. 2003.

[2] A. F. Molisch, "Ultrawideband propagation channels: Theory, measurement, and modeling", *IEEE Trans. Veh. Technol.*, vol. 54, no.5, pp. 1528–1545, Sep. 2005.

[3] A. F. Molisch *et al.*, "A comprehensive standardized model for ultrawideband propagation channels," *IEEE Trans. Antennas Propag.*, vol. 54, no. 11, pp. 3151-3165, Nov. 2006.

[4] C. C. Chong and S. K. Yong, "A generic statistical-based UWB channel model for high-rise apartments," *IEEE Trans. Antennas Propag.*, vol. 53, no. 8, pp. 2389-2399, Aug. 2005.

[5] A. Jahn *et al.*, "Evolution of aeronautical communications for personal and multimedia services," *IEEE Commun. Mag.*, vol. 41, no. 7, pp. 36-43, Jul. 2003.

[6] J. J. Ely, W. L. Martin, G. L. Fuller, T. W. Shaver, J. Zimmerman and W. E. Larsen, "UWB EMI to aircraft radios: field evaluation on operational commercial transport airplanes," in *Proc. Digital Avionics Syst. Conf. 2004*, 24-28 Oct. 2004, pp. 9.D.4-1--9.D.4-11.

[7] J. J. Ely, W. L. Martin, T. W. Shaver, G. L. Fuller, J. Zimmerman and W. E. Larsen, , "UWB EMI to aircraft radios: field evaluation on operational commercial transport airplanes," NASA TP-2005-213606 Vol. 1, Jan. 2005.

[8] N. R. Diaz and M. Holzbock, "Aircraft cabin propagation for multimedia communications," in *Proc. EMPS 2002*, 25-26 Sep. 2002, pp. 281-288.

[9] N. R. Diaz and J. E. J. Esquitino, "Wideband channel characterization for wireless communications inside a short haul aircraft," in *Proc. IEEE VTC 2004 - Spring*, 17-19 May 2004, pp. 223-228.

[10] S. Fisahn, M. Camp, N. R. Diaz, R. Kebel and H. Garbe, "General analysis of leaky section cables for multi-band aircraft cabin communications with different measurement techniques," in *Ultra-Wideband Short-Pulse Electromagnetics 7*, 12-16 Jul. 2004, pp. 509-516.

[11] G. Hankins, L. Vahala and J. H. Beggs, "Propagation prediction inside a B767 in the 2.4 GHz and 5 GHz radio bands," in *2005 IEEE AP-S Int. Symp. Dig.*, 3-8 Jul. 2005, pp. 791-794.

[12] C. P. Niebla, "Topology and capacity planning for wireless heterogeneous networks in aircraft cabins," in *Proc. IEEE PIMRC 2005*, 11-14 Sep. 2005, pp. 2088-2092.

[13] G. A. Breit, H. Hachem, J. Forrester, P. Guckian, K. P. Kirchoff and B. J. Donham, "RF propagation characteristics of in-cabin CDMA mobile phone networks," in *Proc. Digital Avionics Syst. Conf. 2005*, 30 Oct.-3 Nov. 2005, pp. 9.C.5-1--9.C.5-12.

[14] R. Bhagavatula, R. W. Heath and S. Vishwanath, "Optimizing MIMO antenna placement and array configuration for multimedia delivery in aircraft," in *Proc. IEEE VTC 2007 – Spring*, 22-25 Apr. 2007, pp. 425-429.

[15] J. Chuang, N. Xin, H. Huang, S. Chiu and D. G. Michelson, "UWB radiowave propagation within the passenger cabin of a Boeing 737-200 aircraft," in *Proc. IEEE VTC 2007 – Spring*, 22-25 Apr. 2007, pp. 496-500.

[16] J. Jemai *et al.*, "UWB channel modeling within an aircraft cabin," in *Proc. IEEE ICUWB 2008*, 10-12 Sep. 2008, pp. 5-8.

[17] J. Wang, A. S. Mohan and T. A. Aubrey, "Angles-of-arrival of multipath signals in indoor environments," in *Proc. IEEE VTC 1996*, 28 Apr. – 1 May 1996, pp. 155-159.

[18] D. Porrat and Y. Serfaty, "Sub-band analysis of NLOS indoor channel responses," in *Proc. IEEE PIMRC 2008*, 15-18 Sept. 2008, pp. 1-5.

[19] C. W. Kim, X. Sun, L. C. Chiam, B. Kannan, F. P. S. Chin and H. K. Garg, "Characterization of ultra-wideband channels for outdoor office environment," in *Proc. IEEE WCNC*, 13-17 Mar. 2005, pp. 950-955.

[20] D. Cassioli, M. Z. Win and A. F. Molisch, "The ultra-wide bandwidth indoor channel: From statistical model to simulations," *IEEE J. Sel. Areas Commun.*, vol. 20, no. 6, pp. 1247-1257, Aug. 2002.

[21] J. Karedal, S. Wyne, P. Almers, F. Tufvesson and A. F. Molisch, "A measurement-based statistical model for industrial ultra-wideband channels," *IEEE Trans. Wireless Commun.*, vol. 6, no. 8, pp. 3028-3037, Aug. 2007.

[22] J. A. Dabin, A. M. Maimovich and H. Grebel, "A statistical ultra-wideband indoor channel model and the effects of antenna directivity on path loss and multipath propagation," *IEEE J. Sel. Areas Commun.*, vol. 24, no. 4, pp. 752-758, Apr. 2006.

[23] S. S. Ghassemzadeh, L. J. Greenstein, T. Sveinsson, A. Kavcic and V. Tarokh, "UWB delay profile models for residential and commercial indoor environments," *IEEE Trans. Veh. Technol.*, vol. 54, no. 4, pp. 1235-1244, Jul. 2005.

[24] A. Abdi and M. Kaveh, "Performance comparison of three different estimators for the Nakagami *m* parameter using Monte Carlo simulation," *IEEE Commun. Lett.*, vol. 4, no. 4, pp. 119-121, Apr. 2000.

[25] A. K. Marath, A. R. Leyman and H. K. Garg, "DOA estimation of multipath clusters in WiMedia UWB systems," in *Proc. IEEE SAM'08*, 21-23 Jul. 2008, pp. 108-112.

[26] K. Makaratat and S. Stavrou, "Spatial correlation technique for UWB antenna arrays," *Electron. Lett.*, vol. 42, no. 12, pp. 675-676, 8 Jun. 2006.

Chapter 4

Effect of Human Presence on UWB Radiowave Propagation within the Passenger Cabin of a Midsize Airliner[3]

4.1 Introduction

Human presence in the vicinity of a short-range, low-power wireless link often leads to shadowing and scattering that affect both the path gain and time dispersion experienced by the link [1]. Concern for the effect of human presence on short-range wireless links has motivated both measurement- and simulation-based studies of: (1) the depth and duration of shadow fading due to pedestrians moving in the vicinity of such links [2]-[4], (2) the effect of human presence on wireless personal area networks (WPANs), *i.e.*, where one end of the link is located either close to or on a person [5]-[7], and (3) the effect of human presence on wireless body area networks (WBANs), *i.e.*, where both ends of the link are located either close to or on a person [8]-[10].

In recent years, airlines and aircraft manufacturers have expressed much interest in deploying short-range wireless links within the passenger cabins of airliners in order to: (1) permit deployment of in-flight entertainment (IFE) and network access services and (2) facilitate operations and maintenance through deployment of sensor networks [11]-[14]. Although various wireless technologies have been considered and evaluated, ultrawideband (UWB) wireless technologies that operates within the frequency band between 3.1 and 10.6 GHz have attracted particular interest for future systems because it: (1) can support very high data rates (up to 480 Mbps) over short distances, (2) occupies a particularly small footprint, radiates little RF energy, and consumes little power, and (3) can support precise positioning capabilities.

---

[3] A version of this chapter has been submitted for publication: S. Chiu, J. Chuang and D. G. Michelson, "Effect of Human Presence on UWB radiowave propagation within the passenger cabin of a midsize airliner."

With its cylindrical structure, its confined volume, the regular layout of its seating, and its high density of occupancy, an airliner passenger cabin is fundamentally different from the residential, commercial and industrial indoor environments considered previously by UWB researchers [15],[16]. The confined volume and high density of occupancy suggest that human presence will affect the performance of wireless systems in aircraft passenger cabins more than it will in other environments. Two previous studies presented characterizations of the UWB wireless channel within aircraft passenger cabins [17],[18], but disclosed only limited information concerning the effect of human presence on UWB wireless propagation in such environments. In other previous work, assessments of the excess pathloss introduced by human presence and internal components in passenger cabins were presented based upon: (1) narrowband measurements collected using CDMA handsets onboard a Boeing MD-90 with up to 17 passengers in the cabin [19] and (2) simulations of the effect of passengers and internal components on electromagnetic field strength inside Boeing B747, B767 and B777 aircraft passenger cabins [20]. Other previous work has yielded estimates of the manner in which the presence of windows, people and furnishings affect the field statistics and spoil the Q-factor of an enclosed space that functions as a multimode cavity [21]. However, designers require a more complete description of the effect of human presence on propagation in aircraft passenger cabins that account for the different types of paths within such environments and which are based upon larger data sets.

After completing a pair of rigorous research ethics review and recruiting almost 100 volunteers to occupy passenger seats, we collected a few hundred UWB channel frequency responses (CFRs) over the frequency range of 3.1-6.1 GHz in a point-to-multipoint configuration within the passenger cabin of a Boeing 737-200 aircraft. We mounted the transmitting antenna at either the cabin ceiling or headrest level along the centerline of the forward part of the cabin and collected channel frequency response data with the receiving antenna mounted at headrest or armrest level at selected locations throughout the cabin with three degrees of occupancy: empty, partially filled and completely filled. We processed the result to determine the manner in which human presence affects the distance and frequency dependence of path gain, the form of the channel impulse response, the distance and frequency dependence of rms delay spread, and the number of significant paths below a given threshold within the passenger cabin

of a typical mid-size airliner. We selected the frequency range 3.1-6.1 GHz, which corresponds closely to Band Groups 1 and 2 as defined by the WiMedia Alliance, because it is more likely that the lower portion of the UWB band will be used for point-to-multipoint coverage over large portions of the aircraft passenger cabin while the higher portions of the band are used to implement short-range peer-to-peer links [22].

The remainder of this paper is organized as follows. In Section 4.2, we describe our VNA-based UWB channel sounder, our procedure for calibrating it, our data collection procedure and our measurement database. In Section 4.3, we present the results of our investigation of path gain. In Section 4.4, we present the results of our investigation of time dispersion. Finally, in Section 4.5, we summarize our key findings and their implications.

4.2 Measurement Setup

4.2.1 UWB Channel Sounder

Our UWB channel sounder consists of an Agilent E8362B vector network analyzer (VNA), 4-m FLL-400 SuperFlex and 15-m LMR-400 UltraFlex coaxial cables, a pair of Electro-metrics 6865 omnidirectional UWB biconical antennas, tripods and fixtures suitable for mounting the antennas at various locations throughout the aircraft, and a laptop-based instrument controller equipped with a GPIB interface. During data collection, a MATLAB script running on the laptop controlled the VNA and logged the received data.

We recruited volunteers to occupy passenger seats during the measurement session. In order to meet RF emission limits imposed upon us by the Research Ethics Boards at the University of British Columbia and the British Columbia Institute of Technology, we set the transmit power to 5 dBm. We set the intermediate frequency bandwidth of the VNA to 3 kHz which reduced the resulting displayed average noise level (DANL) to -107.2 dBm. The minimum sweep time was automatically set to 2 seconds. As configured, the channel sounder can resolve channel impulse responses (CIRs) with an SNR $\geq$25 dB at transmitter-receiver separation distances of up to 15 m assuming a

distance exponent of 2.2, based on the worst case observed in our previous work [17], and average transmit and receive antenna gains of 0 dBi over all angles and directions.

During data collection, the VNA was configured to sweep from 3.1 to 6.1 GHz over 2560 frequency points. The frequency sampling interval of 1.1718 MHz corresponds to a maximum unambiguous excess delay of 853 ns or a maximum observable distance of 256 m. The frequency span of 3 GHz gives us a temporal resolution of 333 ps or a spatial resolution of 100 mm.

4.2.2 Channel Sounder Calibration

Before measurement data can be collected, the channel sounder must be calibrated so that systematic variations in the amplitude and phase of the measured frequency response due to factors other than the propagation channel can be removed. The process involves two steps. The first step is to use the VNA's built-in calibration routines, which are based upon a standard 12-term error model, to compensate for amplitude and phase distortions up to the point where the cables attach to the transmitting and receiving antennas. Care must be taken to ensure that the distortions for which the error correction model is compensating do not change appreciably during the measurement session, *e.g.*, due to significant cable flexion and torsion, so that the error correction process will not introduce its own distortions. Appropriate cable handling and management techniques are the most effective way to avoid such problems.

The second step, which is much more difficult, is to compensate for the distortions introduced by the antennas themselves. Because the radiation patterns of practical UWB antennas vary with both direction and frequency, individual multipath components (MPCs) arriving at the receiving antenna from different directions will be distorted in different ways. The measured channel response includes elements of the response of both: (1) the propagation channel and (2) the transmitting and receiving antennas. The result is often referred to as the response of the radio channel. In order to perfectly de-embed the propagation channel response from the radio channel response, one would need to measure the frequency-dependent double-directional channel response that accounts for the angle-of-departure (AoD) and angle-of-arrival (AoA) of each ray and the frequency-dependent three-dimensional radiation pattern of each antenna [23].

Implementing the required measurement setup within the confines of the aircraft passenger cabin would be problematic, however.

The antenna calibration problem is simplified considerably if we can assume that the environment is rich with scatterers so that the physical MPCs arrive from all possible directions and each resolvable MPC includes many physical MPCs. Because the directivity of any antenna averaged over all directions is unity for all frequencies, the measured CFR will be independent of the radiation patterns of the transmitting and receiving antennas. In such cases, after appropriate account has been taken for the return loss of the antennas and the amplitude of any line-of-sight (LOS) components, the measured channel response will be equivalent to the propagation channel response.

The dense single cluster form of the CIRs that we observed within that environment suggests that the density of scatterers within the cabin is very high. Moreover, previous work in conventional indoor environments has shown that the AoA distribution in the vertical plane broadens considerably as the size of the enclosed space becomes smaller [24]. Accordingly, it is not unreasonable to assume that the scattering is sufficiently broad that the effective gain of the transmitting and receiving antennas over all directions and frequencies is unity. Thus, while our results strictly characterize the *radio channel*, it seems likely that the measured channel is a useful approximation to the *propagation channel*.

4.2.3 Data Collection

We collected the CFR measurements within the passenger cabin of a Boeing 737-200 aircraft. The cabin, which can seat 130 passengers, is 3.54 m in width, 2.2 m in height and 21 m in length of which 18 m actually includes passenger seating. So that we could assess the effect of human presence on RF propagation aboard the passenger cabin, we collected measurement data with three levels of occupancy: empty, partially full and completely full. When the cabin was partially full, volunteer passengers sat in alternating seats from rows 4 through 19. When the cabin was full, volunteer passengers sat in every seat from row 4 through 19. During data collection, all of the passengers were asked to engage in quiet activities such as talking or reading while seated rather than standing in the aisle or moving about the aircraft. Before we collected production data, we verified

that we could exploit the bilateral and translational symmetry inherent in the cabin layout to dramatically reduce the number of measurements needed to characterize propagation within the aircraft.

We mounted the transmitting antenna along the centerline of the cabin at row 2 at either ceiling or headrest height, as appropriate, in the manner of an access point. We considered three different path types: ceiling-to-headrest (C-to-H), ceiling-to-armrest (C-to-A) and headrest-to-armrest (H-to-A). For both the C-to-H and C-to-A path types, we mounted the transmitting antenna at the ceiling level and used a custom-designed mount to place the receiving antenna at the headrest or armrest level of passenger seats in a reproducible manner on the port side of the aircraft from rows 4 to 19. For the C-to-H path type, the receiving antenna was placed on alternating aisle, middle and window seats, while for the C-to-A path type, the receiving antenna was placed only on alternating middle and window seats. For the H-to-A path type, we mounted the transmitting antenna at the headrest level and placed the receiving antenna at the armrest level of alternating middle seats on the port side of the aircraft from rows 4 to 18. The two different receiving antenna mounting positions not only represent typical use cases such as using a cell phone (at headrest level) or a laptop (at armrest level) but also represent both LOS (at the headrest) and NLOS (at the armrest) channels. A cross-section view of the cabin that shows the various antenna mounting positions is given in Figure 4.1.

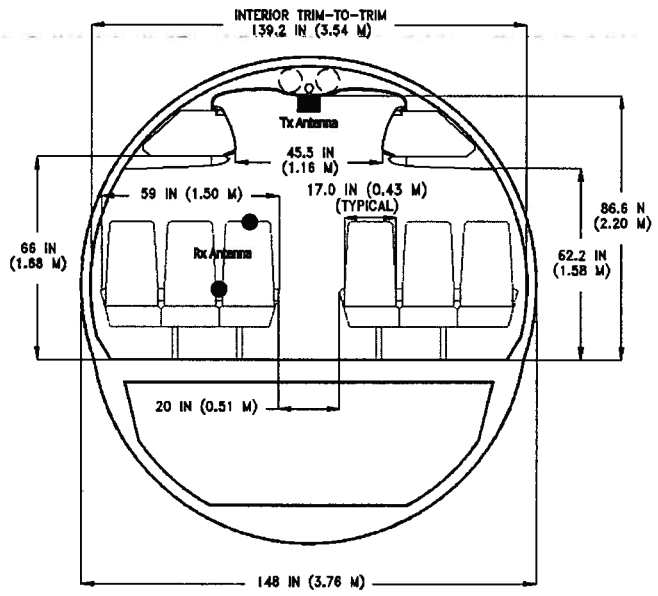

Figure 4.1. Cross-sectional view of the passenger cabin showing the positions at which the transmitting and receiving antennas were deployed in the ceiling-to-headrest and ceiling-to-armrest configurations. The transmitting antenna is lowered to headrest level for the headrest-to-armrest configuration.

4.2.4 Measurement Database

During the development phase, we considered three transmitter locations at rows 2, 11 and 16 and over 50 receiver locations in the empty passenger cabin. For selected paths, we took multiple sweeps to verify the static nature of the channel and the reproducibility of our measurements. This yielded over 200 CFRs in the development phase. During the production phase, we used only one transmitter location and collected data only on the port side of the aircraft. For each of the three levels of occupancy, *i.e.*, empty, partially filled and completely filled, we collected CFRs at 24 and 16 different receiver locations along the port side of the aircraft for the C-to-H and C-to-A path types, respectively. For the empty and full aircraft cases, we also collected CFRs at 8 selected receiver locations for the H-to-A path type. This yielded 136 CFRs in the production phase. In total, we collected over 330 CFRs.

4.3 Effect of Human Presence on Path Gain in the Aircraft Environment

The manner in which path gain decreases with distance determines the maximum range that can be achieved by a wireless link. For UWB-based wireless systems, path gain is an especially important consideration given the relatively low power levels that such systems are permitted to radiate. Within the passenger cabin, path gain decreases with increasing transmitter-receiver separation due to the combined effects of spatial spreading and obstruction by cabin fixtures, seating and passengers. Assessing the effect of human presence on path gain within the aircraft environment allows system designers to more accurately predict the coverage and reliability of UWB-based point-to-multipoint wireless systems deployed within such environments.

We modeled the path gain within the passenger cabin environment as follows. First, we divided the 3.1-6.1 GHz frequency range into two band groups $b = \{1, 2\}$, each of which is 1.5 GHz wide. Over each band group, we verified that the frequency response was effectively flat. We obtained the distance-dependent path gain $G_p(d)$ by taking the average of the magnitude of the measured complex CFRs, $H(f, d)$, across each band group, yielding

$$G_p(d) = \frac{1}{M}\sum_{i=0}^{M-1}\left|H(f_i, d)\right|^2, \tag{3.1}$$

where d is the transmitter-receiver separation distance, M is the number of frequency steps in each band group, and f_i is the ith frequency step. At each location, we estimated the path gain when the aircraft was empty, and then estimated the *reduction* in path gain, ΔG_p, when the aircraft was partially and fully occupied. The configuration of the transmitting and receiving antennas and their antenna patterns remained constant as the level of occupancy increased. Thus, any variation in antenna gain due to changes in the path geometry with distance would have cancelled out when the difference in the estimated path gains was calculated.

In Figure 4.2, the reduction in path gain, ΔG_p, observed in band group 1 is presented as a function of distance, d, for different path types and, within each plot, for different levels of occupancy. Although we had anticipated that the reduction in path gain would

generally increase with distance over the length of the cabin, the actual relationship was more complicated. Initially, path gain decreases as the distance between the transmitter and receiver increases. Beyond the mid-point in the cabin (a distance of between 7 and 9 meters), however, the trend reverses. The time dispersion results presented in the next section do not reveal a similar breakpoint at the mid-point of the cabin so it seems likely that AoA effects are responsible. Although our measurement data are insufficient to reveal such effects, ray tracing simulations similar to those described in [20] may provide additional insight and be a useful next step.

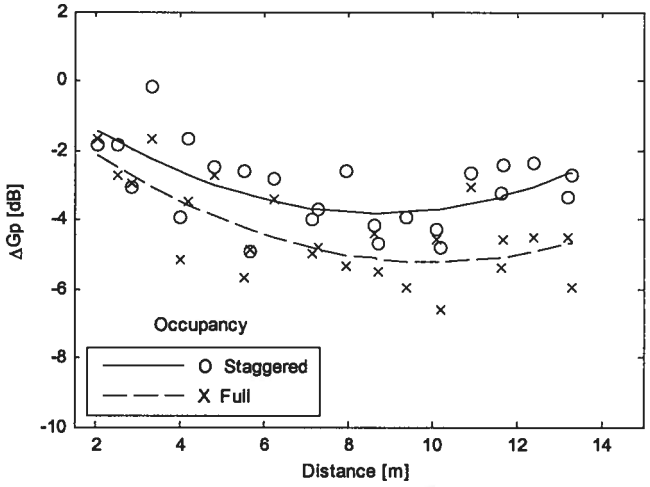

(a)

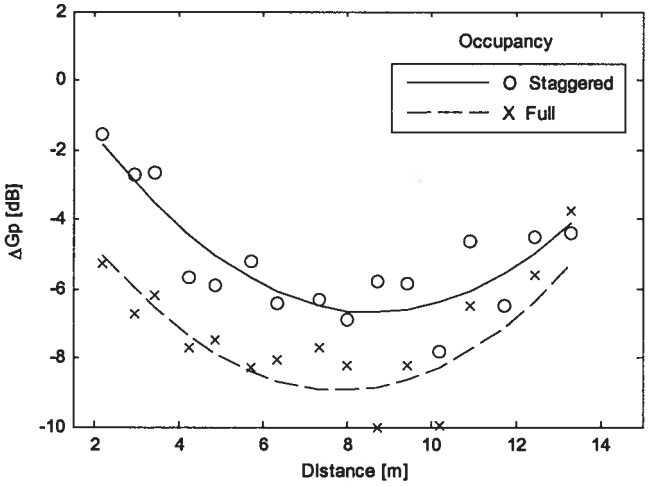

(b)

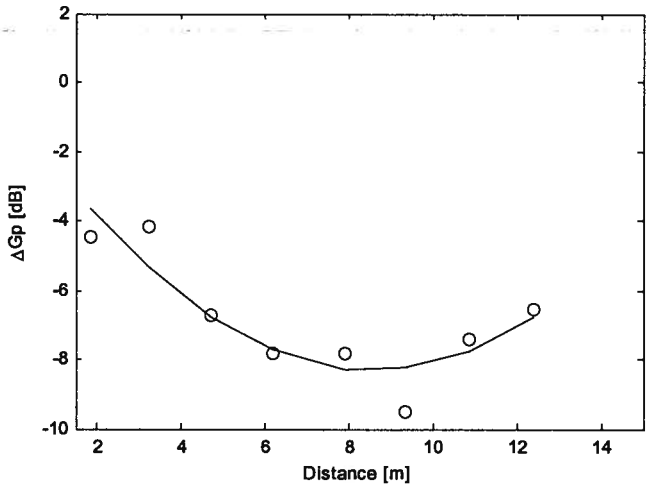

(c)

Figure 4.2. Reduction in path gain with respect to distance for band group 1 for (a) ceiling-to-headrest, (b) ceiling-to-armrest, and (c) headrest-to-armrest configurations.

In all cases and both band groups, we found that the reduction in path gain associated with human presence was well-approximated by a quadratic expression in distance of the form

$$\Delta G_p(d) = \Delta G_{p0} + Ad + Bd^2 + X_\sigma, \tag{3.2}$$

where ΔG_{p0}, A and B are constants and X_σ is a zero-mean Gaussian random variable with a standard deviation of σ that accounts for location variability. In each case, we determined the constants ΔG_{p0}, A and B by applying regression analysis to the measured data. We estimated σ by subtracting the quadratic regression line from the measured values of ΔG_p and fitting the results to a Gaussian distribution. The values of the parameters in each case are presented in Table I. In the C-to-H configuration, the maximum decrease in mean path gain due to human presence is relatively low (no more than a few dB), as one might expect given that the C-to-H paths are relatively unobstructed by human presence. In the C-to-A and H-to-A configurations, the maximum decrease in mean path gain is much greater (up to 10 dB), as one might expect given that the C-to-A and C-to-H paths are much more obstructed by passengers.

Table 4.1. Large-scale path gain parameters for the aircraft passenger cabin environment.

Path Type	Occupancy	Band	ΔG_{p0} [dB]	A [dB/m]	B [dB/m^2]	Location variability, σ [dB]
C-to-H	Empty	1	–	–	–	–
		2	–	–	–	–
	Staggered	1	0.261	-0.941	0.054	0.903
		2	0.718	-0.865	0.051	1.121
	Full	1	-0.326	-0.979	0.049	0.884
		2	-1.109	-0.588	0.033	1.424
C-to-A	Empty	1	–	–	–	–
		2	–	–	–	–
	Staggered	1	2.061	-2.029	0.118	0.824
		2	-0.742	-1.178	0.076	0.578
	Full	1	-1.388	-1.928	0.123	1.252
		2	-1.936	-1.582	0.105	0.881
H-to-A	Empty	1	–	–	–	–
		2	–	–	–	–
	Full	1	-0.635	-1.790	0.104	0.759
		2	1.993	-2.323	0.142	0.521

4.4 Effect of Human Presence on Time Dispersion in the Aircraft Environment

Our first step in characterizing time dispersion within the aircraft passenger cabin was to convert the CFRs that we measured into CIRs. Following [22], we truncated the CFRs into band groups and zero-padded them to restore the original length and thus preserve the temporal resolution. If $f_{b,u}$ and $f_{b,l}$ are the upper and lower frequency boundaries of band group b, respectively, then the complex CFR for band group b is given by

$$H_b(f,d) = \begin{cases} H(f,d), & \text{if } f_{b,l} \le f \le f_{b,h} \\ 0, & \text{otherwise.} \end{cases}, \tag{3.3}$$

Following the approach described in [26], we applied a Kaiser window with $\beta = 7$ to the CFR in order to suppress dispersion of energy between delay bins. We then applied an inverse Fourier transform (IFT) directly to the complex baseband of the CFR to yield a CIR. We expressed the result in the form of a power delay profile (PDP),

$$P_{h,b}(\tau_k) = \left|h_b(\tau_k)\right|^2 = \sum_k a_k \delta(\tau - \tau_k), \tag{3.4}$$

where a_k are the amplitudes (expressed in units of power) of MPCs at different delays τ_k.

Measured PDPs typical of the C-to-A configuration under empty, partially filled and

completely filled conditions in the aircraft are given in Figure 4.3. It is immediately apparent that the passenger cabin is rich with scatterers leading to a high density of MPCs in the PDPs. For LOS channels, we define the start of the PDP as the first MPC that arrives within 10 dB of, and 10 ns, before the peak MPC. For NLOS channels, we define the start of the PDP as the first MPC that arrives within 10 dB of, and 50 ns, before the peak MPC. We remove the propagation delay by setting the start time of the first arriving MPC to zero. These criteria are based upon those adopted by IEEE 802.15.4a and used in [27].

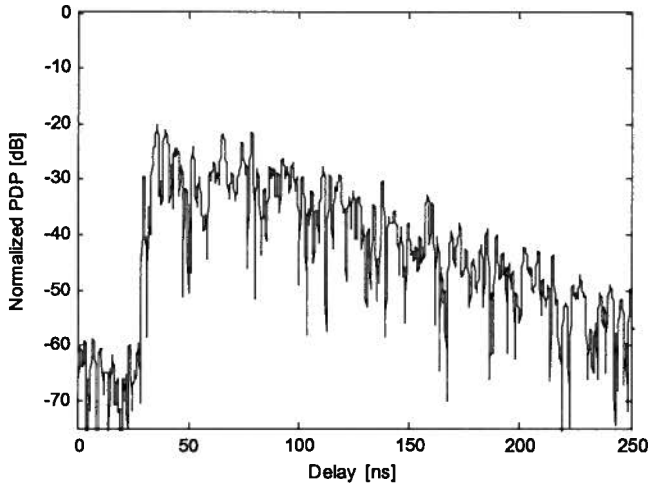

(a)

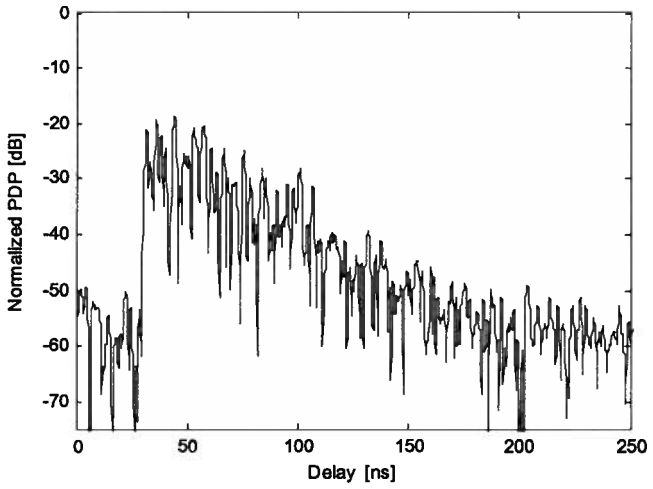

(b)

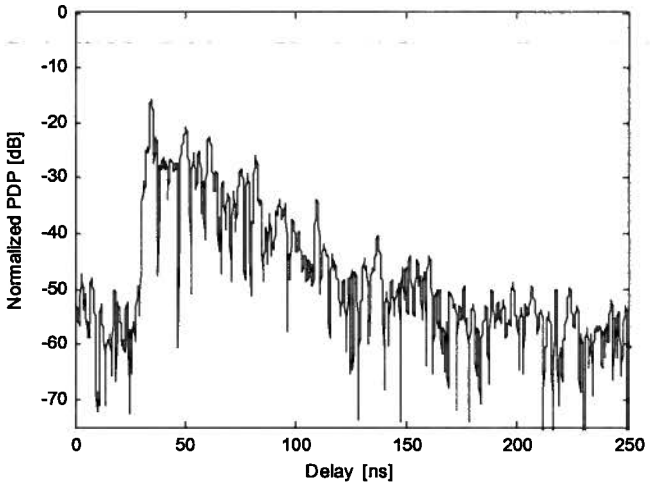

(c)

Figure 4.3. The normalized power delay profiles for band group 2 for the ceiling-to-armrest path type that were observed at row 13 for occupancy levels of: (a) empty, (b) partially full, and (c) completely full.

Using regression techniques, we estimated the decay time constants, τ_0, *i.e.*, the reciprocal of the slope of *the scattered components* in the PDPs, for various path types, degrees of occupancy and band groups. The values are given in Table 4.2. As the density of occupancy increased from empty to half full, the decay rate of the scattered components in the PDP almost doubled. Further increases in the density of occupancy had little effect, however.

Table 4.2. Large-scale delay spread parameters for the aircraft passenger cabin environment.

Path Type	Occupancy	Band	Intercept τ_i[ns]	Distance exponent (rms delay spread), γ	Residual, σ_{ds} [ns]	Decay time constant, τ_0 [ns]
C-to-H	Empty	1	8.21	2.12	3.65	-32.7
		2	5.72	1.88	3.66	-26.7
	Staggered	1	9.52	0.66	2.23	-19.0
		2	7.76	0.58	2.58	-18.5
	Full	1	8.46	0.76	2.58	-17.5
		2	8.05	0.43	2.70	-17.8
C-to-A	Empty	1	11.6	2.10	1.20	-37.0
		2	11.1	1.93	2.20	-37.1
	Staggered	1	10.9	0.78	1.37	-19.3
		2	14.3	0.35	1.96	-17.7
	Full	1	14.2	0.21	1.70	-18.4
		2	10.6	0.63	2.14	-16.6
H-to-A	Empty	1	14.6	1.82	0.89	-33.8
		2	13.1	1.91	0.88	-32.1
	Full	1	9.73	0.92	1.74	-17.4
		2	11.5	0.52	1.05	-18.8

4.4.1 Delay Spread

The normalized first-order moment of a PDP gives the mean excess delay,

$$\tau_{mean} = \frac{\sum_k P_{h,b}(\tau_k)\tau_k}{\sum_k P_{h,b}(\tau_k)}, \tag{3.5}$$

while the square root of the second central moment of a PDP gives the rms delay spread,

$$\tau_{rms} = \sqrt{\tau_{mean}^2 - (\tau_{mean})^2}, \tag{3.6}$$

where

$$\tau_{mean}^2 = \frac{\sum_k P_{h,b}(\tau_k)\tau_k^2}{\sum_k P_{h,b}(\tau_k)}. \tag{3.7}$$

Before we estimated the rms delay spread, we removed all MPCs with amplitudes that are more than 25 dB below the peak component to ensure that only significant MPCs are considered.

In Figure 4.4, we show how rms delay spread depends upon the transmitter-receiver separation distance d for the three different path types (C-to-H, C-to-A, H-to-A) in band group 2. We model the distance dependence as

$$\tau_{rms} = \tau_i + 10\gamma \log d + X_{\sigma_\tau}, \tag{3.8}$$

where τ_i is the mean rms delay spread at $d = 1$ m, γ is the distance exponent, and X_{σ_τ} is a zero-mean Gaussian random variable with a standard deviation of σ_τ that accounts for location variability. The values of these parameters for various path types, degrees of occupancy and both band groups are given in Table 4.2. In all cases where the aircraft was empty, the rms delay spread increased rapidly with distance while increasing the density of occupancy to half-full generally caused γ to decrease by a factor of nearly four. Increasing the density of occupancy caused little further reduction in γ. The decrease in γ is likely the result of energy in the scattered components being blocked or attenuated as the number of passengers aboard the aircraft increase.

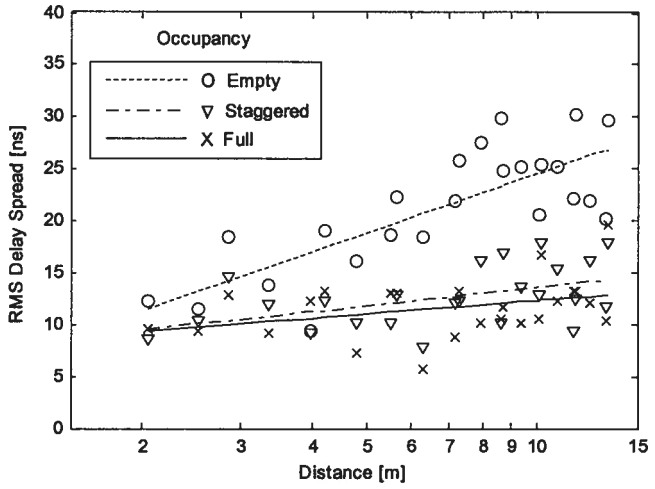

(a)

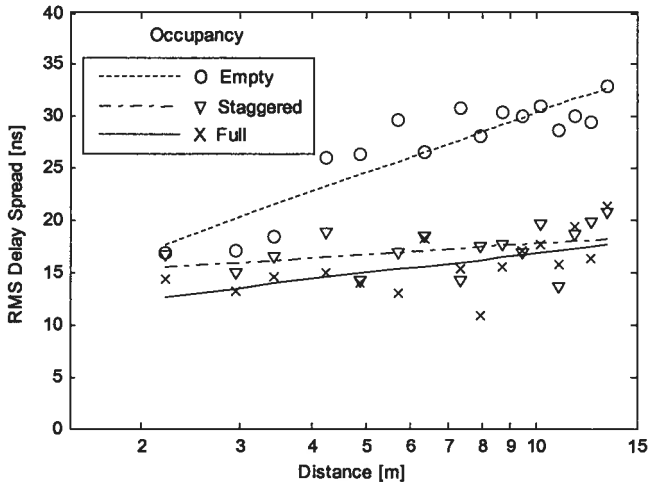

(b)

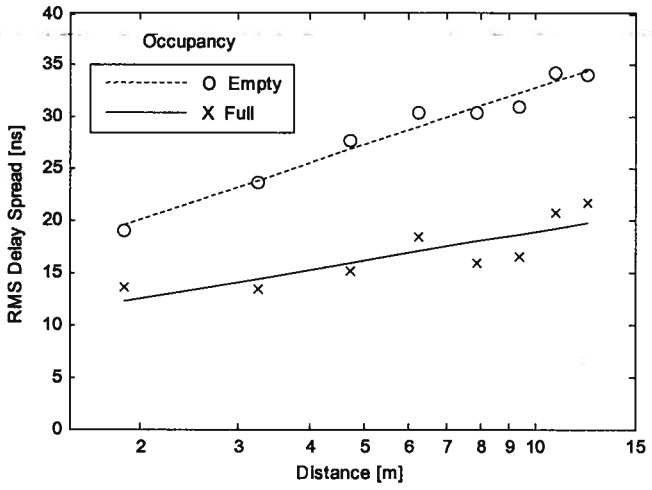

(c)

Figure 4.4. The rms delay spread with respect to distance for band group 2 for (a) ceiling-to-headrest, (b) ceiling-to-armrest, and (c) headrest-to-armrest configurations.

The rms delay spread generally decreases with increasing center frequency, which is likely a consequence of the corresponding increase in attenuation and diffraction losses with frequency. Although increasing from band group 1 to 2 for the C-to-H path type causes the rms delay spread to drop by 15 - 20%, doing so for the C-to-A and H-to-A path types results in little if any reduction. The mean excess delay and rms delay spread that we observed for the C-to-H and C-to-A cases for band group 2 as a function of threshold levels of 5, 10, 15 and 20 dB below the strongest MPC are summarized in Table III and Table IV, respectively.

Table 4.3. Ceiling-to-headrest configuration – mean excess delay, rms delay spread, number of significant paths and energy captured for different threshold levels

Occupancy	Band	Threshold [dB]	τ_{mean} [nsec]	τ_{rms} [nsec]	Num. of Paths	% Power
Empty	1	5	7.85	7.06	24	27
		10	14.3	12.1	116	59
		15	20.1	18.0	288	81
		20	24.3	22.5	520	93
	2	5	1.93	1.68	12	32
		10	5.43	6.41	47	52
		15	10.8	12.3	153	75
		20	15.2	17.2	337	90
Staggered	1	5	3.13	2.43	15	32
		10	6.37	6.19	63	61
		15	9.78	9.84	158	82
		20	12.2	12.7	295	93
	2	5	1.64	1.40	11	38
		10	3.49	3.80	36	60
		15	6.14	7.18	105	80
		20	8.52	10.2	224	92
Full	1	5	2.29	2.53	15	35
		10	5.50	6.09	59	61
		15	8.91	9.61	154	83
		20	11.4	12.7	290	94
	2	5	1.06	0.79	10	40
		10	2.47	3.07	30	59
		15	4.83	6.16	88	78
		20	7.14	9.32	192	91

Table 4.4. Ceiling-to-armrest configuration – mean excess delay, rms delay spread, number of significant paths and energy captured for different threshold levels

Occupancy	Band	Threshold [dB]	τ_{mean} [nsec]	τ_{rms} [nsec]	Num. of Paths	% Power
Empty	1	5	16.9	11.7	53	32
		10	23.2	17.9	217	69
		15	29.0	22.8	458	89
		20	32.3	26.4	715	96
	2	5	11.9	7.88	41	32
		10	18.1	14.0	174	64
		15	23.6	19.3	366	85
		20	27.1	23.2	595	94
Staggered	1	5	7.85	5.34	32	38
		10	10.8	8.30	112	69
		15	14.2	12.3	246	88
		20	16.4	14.9	402	96
	2	5	5.44	3.38	24	35
		10	9.03	7.84	92	66
		15	12.4	11.3	209	86
		20	14.8	14.3	365	95
Full	1	5	6.25	4.30	29	36
		10	10.1	8.44	110	70
		15	13.0	11.3	226	88
		20	14.9	13.8	371	95
	2	5	5.12	3.42	25	37
		10	8.60	7.29	93	68
		15	11.6	10.5	208	87
		20	13.6	12.9	345	95

4.4.2 Number of Significant Paths

We define a significant path as a resolvable MPC that exceeds a given threshold of 5, 10, 15 and 20 dB below the strongest MPC. The number of significant paths that we observed for the C-to-H and C-to-A cases and the percentage of energy that each set captures as a function of the threshold level are summarized in Table 4.3 and Table 4.4, respectively. We found that the PDPs associated with band group 2 have between 10 and 30% fewer significant paths at a given threshold than those associated with band group 1. Moreover, we found that the PDPs measured in a full aircraft have between 40 and 45% fewer significant paths at a given threshold than those measured in an empty aircraft. These results are consistent with our observation that the duration of the PDP shrinks with increased occupancy and increased carrier frequency.

4.5 Conclusions

Because the passenger cabin has a confined volume and may be densely occupied, human presence affects radiowave propagation within a midsized airliner more than in conventional indoor environments such as homes, offices and industrial sites. In order to assess the effect of human presence in such environments, we collected channel frequency response data over the range 3.1 to 6.1 GHz within the passenger cabin of a Boeing 737-200 aircraft.

Our investigation of path gain over point-to-multipoint links within the cabin with the transmitting antenna in the front of the cabin reveals that: (1) the decrease in path gain that occurs as occupancy increases reaches a maximum near the mid-point of the cabin, decreases thereafter, and is well-approximated by a quadratic function, (2) the maximum decrease in path gain becomes more acute as: (a) the transmitting antenna drops from the ceiling to the headrest level and (b) as the receiving antenna drops from the headrest to armrest, (3) in the ceiling-to-headrest configuration, the maximum decrease in the mean path gain due to human presence is only a few dB; in the ceiling-to-armrest or headrest-to-armrest cases, the maximum decrease in the mean path gain is up to 10 dB. Although our measurement data are insufficient to reveal the physical cause of the distance-dependent behavior, ray tracing simulations similar to those described in [20] may

provide additional insight and might be a useful next step.

Our investigation of time dispersion within the cabin reveals that: (1) the channel impulse response always presents a dense single cluster regardless of the level of occupancy, (2) the rms delay spread generally increases with distance when the aircraft is empty but is essentially uniform when the aircraft is partially or fully occupied, (3) both the rms delay spread and the number of significant paths reduces by up to half as the level of occupancy increases from empty to half occupied, and (4) increasing the level of occupancy from half to full has little additional effect.

Our results: (1) suggest that human presence substantially affects radiowave propagation within an aircraft passenger cabin and should be considered when characterizing the performance of in-cabin wireless systems and (2) will be helpful to those wishing to validate the results of software simulations of in-cabin wireless propagation. Further measurements in different aircraft will be required to assess: (1) how seatbacks that incorporate in-flight entertainment units contribute to excess shadowing on ceiling-to-armrest and headrest-to-armrest links and (2) how human presence affects UWB propagation within a wide-body aircraft.

4.6 References

[1] M. Ghaddar, L. Talbi and T. A. Denidni, "Human body modeling for prediction of effect of people on indoor propagation channel," *Electron. Lett.*, vol. 40, no. 25, pp. 1592-1594, 9 Dec. 2004.

[2] R. Ganesh and K. Pahlavan, "Effects of traffic and local movements on multipath characteristics of an indoor radio channel," *Electron. Lett.*, vol. 26, no. 12, pp. 810-812, 7 Jun. 1990.

[3] K. I. Ziri-Castro, W. G. Scanlon, and N. E. Evans, "Prediction of variation in MIMO channel capacity for the populated indoor environemnt using a radar cross-section-based pedestrian model," *IEEE Trans. Wireless Commun.*, vol. 4, no. 3, pp. 1186–1194, May 2005.

[4] K. I. Ziri-Castro, N. E. Evans and W. G. Scanlon, "Propagation modeling and measurements in a populated indoor environment at 5.2 GHz," in *Proc. AusWireless 2006*, 13-16 Mar. 2006, pp. 1-8.

[5] S. L. Cotton and W. G. Scanlon, "Characterization and modeling of the indoor radio channel at 868 MHz for a mobile bodyworn wireless personal area network," *IEEE Antennas Wireless Propag. Lett.*, vol. 6, pp. 51-55, Dec. 2007.

[6] T. B. Welch *et al.*, "The effects of the human body on UWB signal propagation in an indoor environment," *IEEE J. Sel. Areas Commun.*, vol. 20, no. 9, pp. 1778-1782, Dec. 2002.

[7] J. Karedal, A. J. Johansson, F. Tufvesson and A. F. Molisch, "Shadowing effects in MIMO channels for personal area networks," in *Proc. IEEE VTC 2006 Fall*, 25-28 Sep. 2006, pp. 1-5.

[8] A. Fort, J. Ryckaert, C. Desset, P. De Donecker, P. Wambacq and L. Van Biesen, "Ultra-wideband channel model for communication around the human body," *IEEE J. Sel. Areas Commun.*, vol. 24, no. 4, pp. 927-933, Apr. 2006.

[9] S. L. Cotton and W. G. Scanlon, "A statistical analysis of indoor multipath fading for a narrowband wireless body area network," in *Proc. IEEE PIMRC'06*, Sep. 2006, pp. 1-5.

[10] A. Alomainy, Y. Hao, A. Owaldally, C. G. Parini, Y. I. Nechayev, and C. C. Coonstantinou and P. S. Hall, "Statistical analysis and performance evaluation for on-body radio propagation with microstrip patch antennas," *IEEE Trans. Antennas Propag.*, vol. 55, no. 1, pp. 245-248, Jan. 2007.

[11] N. R. Diaz and M. Holzbock, "Aircraft cabin propagation for multimedia communications," in *Proc. EMPS 2002*, 25-26 Sep. 2002, pp. 281-288.

[12] A. Jahn *et al.*, "Evolution of aeronautical communications for personal and multimedia services," *IEEE Commun. Mag.*, vol. 41, no. 7, pp. 36-43, Jul. 2003.

[13] R. Bhagavatula, R. W. Heath and S. Vishwanath, "Optimizing MIMO antenna placement and array configuration for multimedia delivery in aircraft," in *Proc. IEEE VTC 2007 Spring*, 22-25 Apr. 2007, pp. 425-429.

[14] A. Kaouris, M. Zaras, M. Revithi, N. Moraitis and P. Constantinou, "Propagation measurements inside a B737 aircraft for in-cabin wireless networks," in *Proc. IEEE VTC 2008 Spring*, 11-14 May 2008, pp. 2932-2936.

[15] A. F. Molisch, J. R. Foerster and M. Pendergrass, "Channel models for ultrawideband personal area networks," *IEEE Wireless Commun.*, vol. 10, no. 6, pp. 14-21, Dec. 2003.

[16] A. F. Molisch *et al.*, "A comprehensive standardized model for ultrawideband propagation channels," *IEEE Trans. Antennas Propag.*, vol. 54, no. 11, pp. 3151-3165, Nov. 2006.

[17] J. Chuang, N. Xin, H. Huang, S. Chiu and D. G. Michelson, "UWB radiowave propagation within the passenger cabin of a Boeing 737-200 Aircraft," in *Proc. IEEE VTC 2007 Spring*, 22-25 Apr. 2007, pp. 496-500.

[18] J. Jemai *et al.*, "UWB channel modeling within an aircraft cabin," in *Proc. IEEE ICUWB 2008*, 10-12 Sep. 2008, pp. 5-8.

[19] G. A. Breit, H. Hachem, J. Forrester, P. Guckian, K. P. Kirchoff and B. J. Donham, "RF propagation characteristics of in-cabin CDMA mobile phone networks," in *Proc. Digital Avionics Syst. Conf. 2005*, 30 Oct.-3 Nov. 2005, pp. 9.C.5-1--9.C.5-12.

[20] M. Youssef and L. Vahala, "Effects of passengers and internal components on electromagnetic propagation prediction inside Boeing aircrafts," in *2006 IEEE AP-S Int. Symp. Dig.*, 9-14 Jul. 2006, pp. 2161-2164.

[21] M. P. Robinson, J. Clegg and A. C. Marvin, "Radio frequency electromagnetic fields in large conducting enclosures: effects of apertures and human bodies on propagation and field-statistics," *IEEE Trans. Electromagn. Compat.*, vol. 48, no. 2, pp. 304-310, May 2006.

[22] ECMA International, "High rate – ultra wide band (UWB) background," Available: www.ecma-international.org/activities/communicaitons/tg20_UWB_Background.pdf

[23] A. F. Molisch, "Ultrawideband propagation channels: Theory, measurement, and modeling", *IEEE Trans. Veh. Technol.*, vol. 54, no.5, pp. 1528–1545, Sep. 2005.

[24] J. Wang, A. S. Mohan and T. A. Aubrey, "Angles-of-arrival of multipath signals in indoor environments," in *Proc. IEEE VTC 1996*, 28 Apr. – 1 May 1996, pp. 155-159.

[25] W. Q. Malik, D. J. Edwards and C. J. Stevens, "Frequency dependence of fading statistics for ultrawideband systems," *IEEE Trans. Wireless Commun.*, vol. 6, no. 3, pp. 800-804, Mar. 2007.

[26] S. S. Ghassemzadeh, R. Jana, C. W. Rice, W. Turin and V. Tarokh, "Measurement and modeling of an ultra-wide bandwidth indoor channel," *IEEE Trans. Wireless Commun.*, vol. 52, no. 10, pp. 1786-1796, Oct. 2004.

[27] C. C. Chong and S. K. Yong, "A generic statistical-based UWB channel model for high-rise apartments," *IEEE Trans. Antennas Propag.*, vol. 53, no. 8, pp. 2389-2399, Aug. 2005.

[28] V. Erceg *et al.*, "A model for the multipath delay profile of fixed wireless channels," *IEEE J. Sel. Areas Commun.*, vol. 17, no. 3, pp. 399-410, Mar. 1999.

Chapter 5

A Range-Extended UWB Channel Sounder for Characterizing Outdoor Industrial Environments[4]

5.1 Introduction

Wireless devices are increasingly used for preventive maintenance, Supervisory Control and Data Acquisition (SCADA), Real-Time Control (RTC), dispatch, asset tracking and inventory control in outdoor industrial environments to increase productivity, avoid damage to machinery and prevent injury to personnel [1]-[3]. A few examples of outdoor industrial environments include train yards, construction sites, seaports, oil refineries, utility plants, chemical plants, etc. At the time of this writing, outdoor ultrawideband (UWB) communications is limited to the usage between mobile devices in the 3.1-10.6 GHz range [4]. Provided that regulatory issues can be dealt with, UWB wireless technology will be of particular interest for future systems in outdoor industrial environments for the aforementioned applications. As described in [5], one of the most promising applications for UWB is sensor networks. In such applications, the data rates are typically less than 1 Mbit/s and the good ranging and geolocation capabilities of UWB are especially useful [6].

In order to develop UWB systems in outdoor industrial environments that realize the foreseeable applications, it is first necessary to understand the nature of the propagation channel, i.e., the factors that affect coverage and reliability such as the transmitting and receiving antenna height, the transmitter-receiver separation distance and the scatterers presented in the environment itself. Previous work has been mostly concerned with either indoor industrial [7]-[10] or open outdoor environments [6],[11]. However, unlike indoor industrial environments, outdoor industrial sites usually pose a much less scattered

[4] A version of this chapter is to be submitted for publication: S. Chiu, J. Chuang and D. G. Michelson, "A Range-Extended UWB Channel Sounder for Characterizing Outdoor Industrial Environments."

environment. And unlike conventional open outdoor environments, outdoor industrial sites often have metallic structures or large industrial vehicles such as trains, dump trucks, concrete pourers, etc. in the vicinity. Past work concerning radiowave propagation in the outdoor industrial environment has included: (1) path loss and time dispersion results based on wideband measurements at 915 MHz over a measurement bandwidth of 20 MHz in an active train yard [12],[13], and (2) excess path loss results based on UWB measurements over the range 25 MHz to 18 GHz in an oil refinery [2],[3]. In this paper, we focus on the manner in which path loss and time dispersion vary with transmitter-receiver separation under both line-of-sight (LOS) and non-line-of-sight (NLOS) conditions in such environments.

UWB measurements can be performed in a number of ways by using a pulse sounder, a correlative channel sounder or a vector network analyzer (VNA). Of all these measurement devices, VNA is the most popular among researchers as measurements with a large bandwidth can be performed rather effortlessly. However, one of the issues with VNA-based measurements is that the range is often limited by the use of RF cables. Clearly, the longer the cables used, the higher the attenuation will be, especially at higher frequencies, which significantly degrades the system margin. In outdoor industrial environments, the ranges considered are usually over 100 m, rendering the VNA impractical for measurements in such environments. Here, we describe a range-extended VNA-based UWB channel sounder suitable for the characterization of UWB radiowave propagation over the range of 3.1-6.1 GHz in outdoor industrial environments. We selected the frequency range 3.1-6.1 GHz, which corresponds closely to Band Groups 1 and 2 as defined by the WiMedia Alliance, because it is more likely that the lower portion of the UWB band will be used for point-to-multipoint coverage over larger distances [14].

The remainder of this paper is organized as follows. In Section II, we describe our VNA-based range-extended UWB channel sounder, our procedure for calibrating it, our proposed data collection procedure and our proposed measurement database. In Section III, we describe the data reduction process for typical UWB channel frequency response (CFR) data for the study of distance and frequency dependence of path gain and time dispersion. Finally, in Section IV, we summarize our contributions and their implications.

5.2 Measurement Setup

5.2.1 UWB Channel Sounder Configuration

Our UWB channel sounder consists of an Agilent E8362B VNA, a Miteq SCMT-100M11G optical transmitter with a matching Miteq SCMR-100M11G optical receiver, 500-m optical fiber, Mini Circuits ZVA-183+ power amplifier, three 0.5-m and two 4-m FLL-400 SuperFlex coaxial cables, a pair of Electro-metrics 6865 UWB omnidirectional biconical antennas, a Electro-metrics 6865A UWB omnidirectional biconical antenna, a Samlex America 300 Watt pure sine-wave inverter, a 12 VDC 35 Ah battery, a handcart and a laptop-based instrument controller equipped with a GPIB interface. During data collection, a MATLAB script running on the laptop controlled both the VNA and logged the received data. The measurement setup is shown in Figure 5.1.

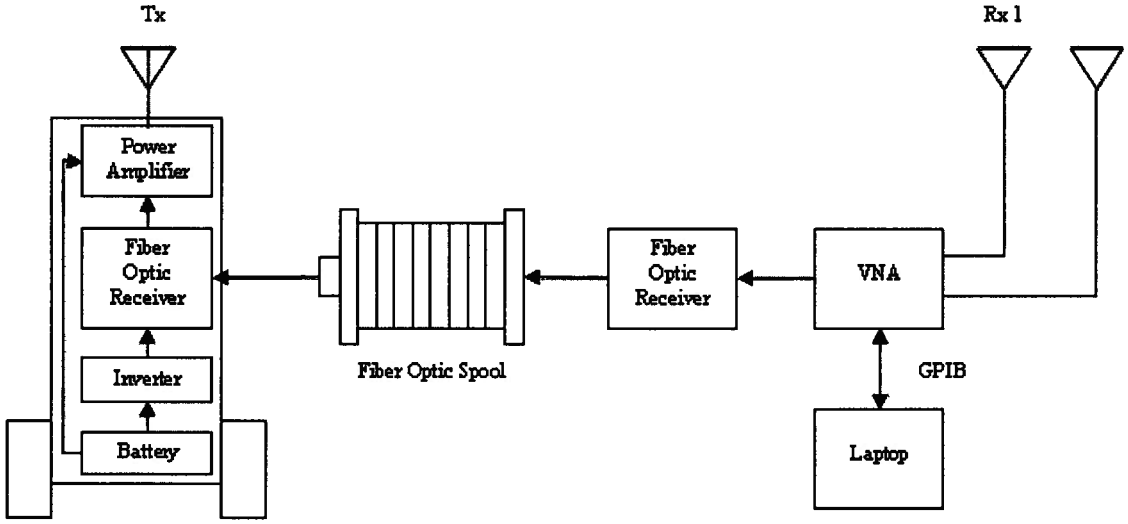

Figure 5.1. The range-extended UWB channel Sounder.

Because the maximum input power to the optical receiver is -14 dBm, we set the transmit power of the VNA accordingly. We set the intermediate frequency bandwidth of the VNA to 3 kHz which reduced the resulting displayed average noise level (DANL) to -107.2 dBm. The minimum sweep time was automatically set to 2 seconds. The system link budget is given in Table 5.1 for the bottom and top of our frequency range: 3.1 and 6.1 GHz. As configured, the channel sounder can resolve channel impulse responses

(CIRs) with an SNR ≥35 dB at transmitter-receiver separation distances of up to 200 m assuming a distance exponent of 2 and average transmit and receive antenna gains over all angles and directions of 0 dBi.

Table 5.1. Link budget for the range-extended UWB channel sounder.

Links	Values	
	3.1 GHz	6.1 GHz
Transmitted Power	-14 dBm	-14 dBm
Transmit Cable Gain	-0.4 dB	-0.7 dB
Optical Fiber System Gain	14 dB	14 dB
Optical Fiber Gain (1dB/km)	-0.5 dB	-0.5 dB
Power Amplifier Gain	26 dB	26 dB
Average Transmit Antenna Gain	0 dBi	0 dBi
Path Gain at 200 m*	-88.3 dB	-94.2 dB
Average Receive Antenna Gain	0 dBi	0 dBi
Receive Cable Gain	-1.2 dB	-1.8 dB
Received Power	-63.2 dBm	-71.2 dBm
Receiver Sensitivity	-107.2 dBm	-107.2 dBm
System Margin	44.0 dB	36.0 dB

*Calculated using a path loss exponent of 2

During data collection, we will configure the VNA to sweep from 3.1 to 6.1 GHz over 6401 frequencies. The frequency sampling interval of 1.1718 MHz corresponds to a maximum unambiguous excess delay of 853 ns or a maximum observable distance of 256 m. The frequency span of 3 GHz gives us a temporal resolution of 333 ps or a spatial resolution of 100 mm.

5.2.2 UWB Channel Sounder Calibration

Before use, the channel sounder must be calibrated so that systematic variations in the amplitude and phase of the measured frequency response due to factors other than the propagation channel can be removed. The process involves two steps. In the first step, we will use through-line calibration to remove the frequency distortion introduced by the VNA, amplifier, optical fiber system and the coaxial cables. Care must be taken to ensure that the distortions for which the through-line calibration is compensating do not change appreciably during the measurement session, *e.g.*, due to significant cable flexion and torsion, so that the error correction process will not introduce its own distortions. Appropriate cable handling and management techniques are the most effective way to avoid such problems.

The second step, which is much more difficult, is to compensate for the distortions introduced by the antennas themselves. Because the radiation patterns of practical UWB antennas vary with both direction and frequency, individual multipath components (MPCs) arriving at the receiving antenna from different directions will be distorted in different ways. The measured channel response includes elements of the response of both: (1) the propagation channel and (2) the transmitting and receiving antennas. The result is often referred to as the response of the radio channel. In order to perfectly de-embed the propagation channel response from the radio channel response, one would need to measure the frequency-dependent double-directional channel response that accounts for the angle-of-departure (AoD) and angle-of-arrival (AoA) of each ray and the frequency-dependent three-dimensional radiation pattern of each antenna [4]. Implementing the required measurement setup would require expensive equipment, however.

The antenna calibration problem is simplified considerably if we can assume that the environment is free-space and that the transmitting and receiving antennas are mounted at the same height. In this way, the physical MPCs arrive only in the direction of maximum gain, *i.e.*, the azimuthal plane. This is not an unreasonable assumption in the outdoor industrial environment as the environment is open and the considered distances are often greater than 100 m. Previous work in conventional indoor environments has shown that the AoA distribution in the vertical plane narrows considerably as the size of the enclosed space becomes larger [15]. While this suggests that the AoA distribution in the vertical plane in the outdoor industrial environment is likely to be narrow, it is not likely to be azimuthal. Thus, while our results strictly characterize the *radio channel*, it seems likely that the measured channel is a useful approximation to the *propagation channel*.

5.2.3 Data Collection

Measurements will be conducted in outdoor industrial sites, as whatever is available to us. In future measurement campaigns, we suggest that two receiving antenna mounting locations be considered: above and below truck-top level. The two mounting locations are chosen to resemble practical scenarios observed in outdoor industrial environments.

In such environments, the antenna at one end of the link is usually mounted on industrial vehicles such as trains, dump trucks, concrete pourers, *etc.* In some cases, such as that for trains, the antenna may be mounted on the rooftop of the vehicle to allow symmetric coverage on both sides of the vehicle. In other cases, however, such as that for concrete pourers, there may be moving mechanical parts which limit antenna mounting locations to the sides of the vehicle.

Before collecting production data, development runs should always be conducted in order to become familiar with the environment, identify any issues with the measurement equipment or data collection procedures and identify models against which the measurement data could be reduced. If we can verify the static nature of the channel and the consistency of our measurements by demonstrating that consecutive CFR measurements over a given path are essentially identical, then this would allow us to take just one sweep per location during production runs and thereby dramatically reduce the number of measurements needed to characterize the outdoor industrial environment.

5.2.4 Measurement Database

The measurement database will be a combination of the data collected during the development and production runs. During both the development and production runs, measurement data should be collected for the two considered receiving antenna mounting locations described in Section II-C. The database should be large enough such that the quality of the results from data analysis is not compromised. If possible, we would like to cover as wide a range of outdoor industrial environments possible, such as train yards, construction sites, seaports, oil refineries, utility plants, chemical plants, *etc.*

5.3 Data Reduction

Once the measurement data has been collected, we will need to reduce them in such a way that is directly applicable to those who are planning UWB deployments and field trials in outdoor industrial environments. In the following two sections, we describe the propose methods for the reduction of UWB CFR data collected in such environments.

The proposed methods are based on those used by other researchers and on our previous work [17].

5.3.1 Path Gain

The manner in which path gain decreases with distance determines the maximum range that can be achieved by a wireless link. For UWB-based wireless systems, path gain is an especially important consideration given the relatively low power levels that such systems are permitted to radiate. A path gain model will allow system designers to more accurately predict the coverage and reliability of UWB-based point-to-multipoint wireless systems deployed within outdoor industrial environments.

We propose that the path gain in the outdoor industrial environment be modeled as follows. First, we will divide the 3.1-6.1 GHz frequency range into two band groups b = {1, 2}, each of which is 1.5 GHz wide. For each band group, we will verify that the frequency response is effectively flat over the band. In decibels, the path gain with respect to distance in each band group can be modeled by

$$G_p(d) = G_{p0} - 10n\log_{10}\left(\frac{d}{d_o}\right) + X_\sigma . \tag{5.1}$$

where d is the distance from the transmitter to the receiver in meters, d_0 = 1 m is the reference distance, G_{p0} is the path gain at d_0, n is the distance exponent and X_σ is a zero-mean Gaussian random variable with a standard deviation of σ that accounts for location variability. We can then obtain the distance-dependent path gain $G_p(d)$ by taking the average of the magnitude of the measured complex CFRs, $H(f, d)$, across each band group, yielding

$$G_p(d) = \frac{1}{M}\sum_{i=0}^{M-1}\left|H(f_i, d)\right|^2 . \tag{5.2}$$

where M is the number of frequency steps in each band group, and f_i is the ith frequency step. We determine the distance exponent n and the intercept point G_{p0}. We estimate σ by subtracting the regression line from the measured values of path gain and fitting the results to a Gaussian distribution.

The effect of receiving antenna height on path gain will be studied. Clearly, since the channel is considered LOS for the case when the receiving antenna is mounted above

truck-top level, we expect to see that the mean path gain will be higher than that observed in the case when the receiving antenna is mounted below truck-top level.

5.3.2 Time Dispersion

The first step in characterizing time dispersion in the outdoor industrial environment is to convert the measured CFRs into CIRs. Following [18], we will truncate the CFRs into band groups and zero-padded them to restore the original length and thus preserve the temporal resolution. If $f_{b,u}$ and $f_{b,l}$ are the upper and lower frequency boundaries of band group b, respectively, then the complex CFR for band group b is given by

$$H_b(f,d) = \begin{cases} H(f,d), & \text{if } f_{b,l} \le f \le f_{b,h} \\ 0, & \text{otherwise.} \end{cases} \quad (3.3)$$

Following the approach described in [19], we will apply a Kaiser window with $\beta = 7$ to the CFR in order to suppress dispersion of energy between delay bins. We will then apply an inverse Fourier transform (IFT) directly to the complex baseband of the CFR to yield a CIR. It is convenient to express the result in the form of a power delay profile (PDP),

$$P_{h,b}(\tau_k) = |h_b(\tau_k)|^2 = \sum_k a_k \delta(\tau - \tau_k), \quad (3.4)$$

where a_k are the amplitudes (expressed in units of power) of MPCs at different delays τ_k.

When the PDP corresponds to a LOS case, we define its start as the first MPC that arrives within 10 dB of, and 10 ns, before the peak MPC. When the PDP corresponds to a NLOS case, we define the start of the PDP as the first MPC that arrives within 10 dB of, and 50 ns, before the peak MPC. We remove the propagation delay by setting the start time of the first arriving MPC to zero. These criteria are based upon those described in [20]. In the following two subsections, we describe the parameters that can be extracted from the PDP. Namely, we detail on the data reduction for delay spread and the number of significant paths.

5.3.2.1 Delay Spread

The normalized first-order moment of a PDP gives the mean excess delay,

$$\tau_{mean} = \frac{\sum_k P_h(\tau_k)\tau_k}{\sum_k P_h(\tau_k)}, \tag{3.5}$$

while the square root of the second central moment of a PDP gives the RMS delay spread,

$$\tau_{rms} = \sqrt{\tau_{mean}^2 - (\tau_{mean})^2}, \tag{3.6}$$

where

$$\tau_{mean}^2 = \frac{\sum_k P_h(\tau_k)\tau_k^2}{\sum_k P_h(\tau_k)}, \tag{3.7}$$

In the outdoor industrial environment, the PDP is expected to show clustering. Before we estimate the RMS delay spread, we will remove all MPCs with amplitudes that are more than 25 dB below the peak scattered component. This ensures that only significant MPCs are considered.

The RMS delay spread generally increases with transmitter-receiver separation distance *d*. We suggest modeling the distance dependence as proportional to d^{γ} for the two considered receiver mounting locations. In addition, RMS delay spread decreases with increasing center frequency and bandwidth [18]. Thus, we expect that the RMS delay spread observed in outdoor industrial environments to decrease as: (1) we move from band 1 to band 2 and (2) compared to those observed in [12].

5.3.2.2 Number of Significant Paths

The number of significant paths and the percentage of energy captured by these paths have important implications on the design of rake receivers such as the number of fingers required. We define a significant path as a resolvable MPC that exceeds a given threshold of 5, 10, 15 and 20 dB below the strongest MPC. We then calculate the percentage of energy carried by these significant paths as compared to that of the entire PDP.

5.4 Conclusions

The outdoor industrial environment is quite distinct from the residential, office, industrial, outdoor and bodycentric environments previously considered by the IEEE 802.15.4a channel modeling committee and its contributors in which: (1) unlike indoor industrial environments, outdoor industrial sites usually pose a much less scattered environment, and (2) unlike conventional open outdoor environments, outdoor industrial sites often have metallic structures or large industrial vehicles in the vicinity. In this work, we have presented a fully operational range-extended UWB channel sounder which is ideal for data collection, and hence the characterization of radiowave propagation, in such environments. Our range-extended channel sounder allows measurement distances of up to 500 m and can be easily configured to incorporate another receiving antenna if required. In addition, whereas the model given by IEEE 802.15.4a for outdoor environments covers only a suburban-like microcell scenario with a rather small range, our work in this area will provide a useful supplement.

5.5 References

[1] M. Ward, T. Thorpe, A. Price and C. Wren, "Implementation and control of wireless data collection on construction sites," *Journal of Information Technology in Construction*, vol. 9, Aug. 2004.

[2] K. A. Remley et al., "Measurements to support broadband modulated-signal radio transmissions for the public-safety sector," *National Institute of Standards and Technology*, Technical Note 1546, April 2008.

[3] K. A. Remley, G. Koepke, C. L. Holloway, C. Grosvenor and D. G. Camell, "Radio communications for emergency responders in high-multipath outdoor environments," in *Proc. ISART 2008*, June 2008.

[4] A. F. Molisch, "Ultrawideband propagation channels: Theory, measurement, and modeling," *IEEE Trans. Veh. Technol.*, vol. 54, no.9, pp. 1528–1545, Sep. 2005.

[5] I. Guvenc, H. Arslan, S. Gezici and H. Kobayashi, "Adaptation of multiple access parameters in time hopping UWB cluster based wireless sensor networks," in *Proc. Int. Conf. Mobile Ad-hoc Sensor Syst.*, Oct. 2004, pp. 235-244.

[6] A. F. Molisch et al., "A comprehensive standardized model for ultrawideband propagation channels," *IEEE Trans. Antennas Propag.*, vol. 54, no. 11, pp. 3151-3165, Nov. 2006.

[7] T. S. Rappaport, "Characterization of UHF multipath radio channels in factory buildings," *IEEE Trans. Antennas Propag*, vol. 37, no. 8, pp. 1058–1069, Aug. 1989.

[8] T. S. Rappaport, S. Y. Seidel and K. Takamizawa, "Statistical channel impulse response models for factory and open plan building radio communication system design," *IEEE Trans. on Commun.*, vol. 39, no. 5, pp. 794–807, May 1991.

[9] E. Tanghe et al., "Large-scale fading in industrial environments at wireless communication frequencies," in *Proc. IEEE AP-S 2007*, June 2007, pp. 3001–3004.

[10] J. Karedal, S. Wyne, P. Almers, F. Tufvesson and A. F. Molisch, "A measurement-based statistical model for industrial ultra-wideband channels," *IEEE Trans. Wireless Commun.*, vol. 6, no. 8, pp. 3028-3037, Aug. 2007.

[11] C. W. Kim, X. Sun, L. C. Chiam, B. Kannan, F. P. S. Chin and H. K. Garg, "Characterization of ultra-wideband channels for outdoor office environment," in *Proc. IEEE WCNC*, 13-17 Mar. 2005, pp. 950-955.

[12] W. G. Newhall, K. J. Saldanha and T. S. Rappaport, "Propagation time delay spread measurements at 915 MHz in a large train yard," in *Proc. IEEE VTC 1996*, April 1996, pp. 864–868.

[13] W. G. Newhall, "Wideband propagation measurement results, simulation models, and processing techniques for a sliding correlator measurement system," *Master Thesis*, Nov. 1997.

[14] ECMA International, "High rate – ultra wide band (UWB) background," Available: www.ecma-international.org/activities/communicaitons/tg20_UWB_Background.pdf

[15] J. Wang, A. S. Mohan and T. A. Aubrey, "Angles-of-arrival of multipath signals in indoor environments," in *Proc. IEEE VTC 1996*, 28 Apr. – 1 May 1996, pp. 155-159.

[16] D. Porrat and Y. Serfaty, "Sub-band analysis of NLOS indoor channel responses," in *Proc. IEEE PIMRC 2008*, 15-18 Sept. 2008, pp. 1-5.

[17] J. Chuang, N. Xin, H. Huang, S. Chiu and D. G. Michelson, "UWB radiowave propagation within the passenger cabin of a Boeing 737-200 Aircraft," in *Proc. IEEE VTC 2007 – Spring*, 22-25 Apr. 2007, pp. 496-500.

[18] W. Q. Malik, D. J. Edwards and C. J. Stevens, "Frequency dependence of fading statistics for ultrawideband systems," *IEEE Trans. Wireless Commun.*, vol. 6, no. 3, pp. 800-804, Mar. 2007.

[19] S. S. Ghassemzadeh, R. Jana, C. W. Rice, W. Turin and V. Tarokh, "Measurement and modeling of an ultra-wide bandwidth indoor channel," *IEEE Trans. Wireless Commun.*, vol. 52, no. 10, pp. 1786-1796, Oct. 2004.

[20] C. C. Chong and S. K. Yong, "A generic statistical-based UWB channel model for high-rise apartments," *IEEE Trans. Antennas Propag.*, vol. 53, no. 8, pp. 2389-2399, Aug. 2005.

Chapter 6

Conclusions and Recommendations

6.1 Conclusions

Previous work on ultrawideband (UWB) has only considered conventional environments such as residential, office, outdoor, industrial and body-centric environments [1]-[5]. With the growing interest of deploying UWB wireless devices in less conventional environments or under more extreme conditions, measurement-based channel models that accurately describe the nature of UWB radiowave propagation in such environments is essential. In this thesis, we have: (1) characterized UWB propagation within the passenger cabin of a typical mid-size airliner, and (2) assembled an operational range-extended UWB channel sounder suitable for data collection in outdoor industrial environments.

Upon reducing the measurement data that we collected using different transmitter/receiver configurations and under different densities of occupancy aboard the Boeing 737-200, we have found that: (1) scattering and reflection accounts for the bulk of the energy that arrives at a given receiving antenna, including cases where a clear line-of-sight between the transmitter and receiver exists, (2) the dense and regular layout of the seats combined with obstruction by the overhead bins causes the coverage pattern to take the form of chevron-shaped contours with path gain decreasing least rapidly along the aisle seats and most rapidly along the window seats, (3) there is significant advantage to using higher portions of the UWB band for short-range applications and reserving lower portions of the band for longer range applications in such environments, (4) the shape of the channel impulse response (CIR) generally follows IEEE 802.15.4a's dense single-cluster model, but with negligible rise time if the link is line-of-sight (LOS), (5) the shape parameters that we extracted for CIRs under both LOS and non-line-of-sight (NLOS) conditions were distance dependent, (6) human presence can substantially affect both path gain and time dispersion within the aircraft, and (7) the receiving antenna should be mounted at the headrest level instead of the armrest to minimize blockage from the seated passengers.

The range-extended UWB channel sounder that we have devised and implemented not only allows long range measurements in environments such as outdoor industrial sites, but also allows between-floors and through-walls measurements. The VNA-based channel sounder makes it easily configurable to perform narrowband, wideband and UWB measurements.

In this work, we have either made significant contributions to filling some of the significant gaps in the literature or made an essential first step that will facilitate future work. The results that we presented in Chapters 2 to 4 will assist: (1) those who are planning UWB deployments and field trials in aircraft and (2) those who need to simulate UWB systems in aircraft using realistic channels. Specifically, the work in Chapters 2 and 4 will affect systems and deployment of UWB devices while the work in Chapter 3 will affect receiver design. The range-extended UWB channel sounder that we described in Chapter 5 will serve as a first step for characterizing outdoor industrial environments.

6.2 Recommendations for Further Work

In the aircraft studies, we have only considered the possibility of mounting the transmitting antenna in the manner of an access point at ceiling height along the centerline of the cabin. While this provides symmetrical coverage across the cabin and keeps the access point at the greatest possible distance from seated passengers, there may be practical reasons why it may be desirable to mount the access point at a lower height on a cabin wall instead, *e.g.*, proximity to cabin wiring, avoidance of blockage by overhead bins, *etc.*, as was done in [6].

For practical reasons, we were only able to characterize UWB propagation within the passenger cabin of a Boeing 737-200. While our results serves as a starting point for further work and should be representative of those observed in aircraft with similar cross-section dimensions, we suggest further work to characterize the UWB propagation within passenger cabins of wider-bodied aircraft. And unlike modern aircrafts, the Boeing 737-200 does not have electronics installed on the passenger seatbacks. In addition, passenger luggage was not considered in our study. Attenuation is expected to increase with these

additional components aboard the passenger cabin and further work is required to assess the extent of each of these effects.

In our work concerning human presence, we have only characterized the UWB path gain and time dispersion over the range 3.1 – 6.1 GHz. While this chosen frequency range corresponds closely to Band Groups 1 and 2 as defined by the WiMedia Alliance and is more likely to be used for point-to-multipoint coverage over large portions of the aircraft passenger cabin, there may be practical reasons why it may be more advantageous to using the higher portions of the UWB band, *e.g.*, Band Group 6 as defined by the WiMedia Alliance is the universally licensed band for UWB devices.

Upon setting up and configuring the range-extended channel sounder, the obvious next step is to collect measurement data at actual outdoor industrial sites such as train yard or construction sites. The measurement data can then be reduced using the proposed methods with the aim of characterizing the UWB path gain and time dispersion in such environments. Moreover, the results will provide a useful supplement to the work previously done by IEEE 802.15.4a.

6.3 References

[1] A. F. Molisch, J. R. Foerster and M. Pendergrass, "Channel models for ultrawideband personal area networks," *IEEE Wireless Commun.*, vol. 10, no. 6, pp. 14-21, Dec. 2003.

[2] A. F. Molisch, "Ultrawideband propagation channels: Theory, measurement, and modeling", *IEEE Trans. Veh. Technol.*, vol. 54, no.5, pp. 1528–1545, Sep. 2005.

[3] A. F. Molisch et al., "A comprehensive standardized model for ultrawideband propagation channels," *IEEE Trans. Antennas Propag.*, vol. 54, no. 11, pp. 3151-3165, Nov. 2006.

[4] J. Karedal, S. Wyne, P. Almers, F. Tufvesson and A. F. Molisch, "A measurement-based statistical model for industrial ultra-wideband channels," *IEEE Trans. Wireless Commun.*, vol. 6, no. 8, pp. 3028-3037, Aug. 2007.

[5] C. W. Kim, X. Sun, L. C. Chiam, B. Kannan, F. P. S. Chin and H. K. Garg, "Characterization of ultra-wideband channels for outdoor office environment," in *Proc. IEEE WCNC*, 13-17 Mar. 2005, pp. 950-955.

[6] J. Jemai et al., "UWB channel modeling within an aircraft cabin," in *Proc. IEEE ICUWB 2008*, 10-12 Sep. 2008, pp. 5-8.

Appendix A

Through-Line Calibration of Systematic Errors

Prior to use, the UWB channel sounder must be calibrated to compensate for amplitude and phase distortions up to the point where the cables attach to the transmitting and receiving antennas. The intention is to calibrate for the systematic errors in the measurement system, *i.e.*, errors that do not vary over time and can be removed from the measurement process mathematically. These errors are caused by imperfections in the test equipment and setup such as cables, connectors, signal leakage, signal reflections and frequency response. The VNA provides built-in calibration routines for two-port error correction, which yields the most accurate results because it takes into consideration all of the major sources of systematic error. The calibrations routines are based upon a 12-term error model, which is shown in Figure A.1. In the figure, S_{11}, S_{12}, S_{21} and S_{22} are the S-parameters measured in the forward and reverse directions and the subscript 'A' denotes the actual values of the parameters.

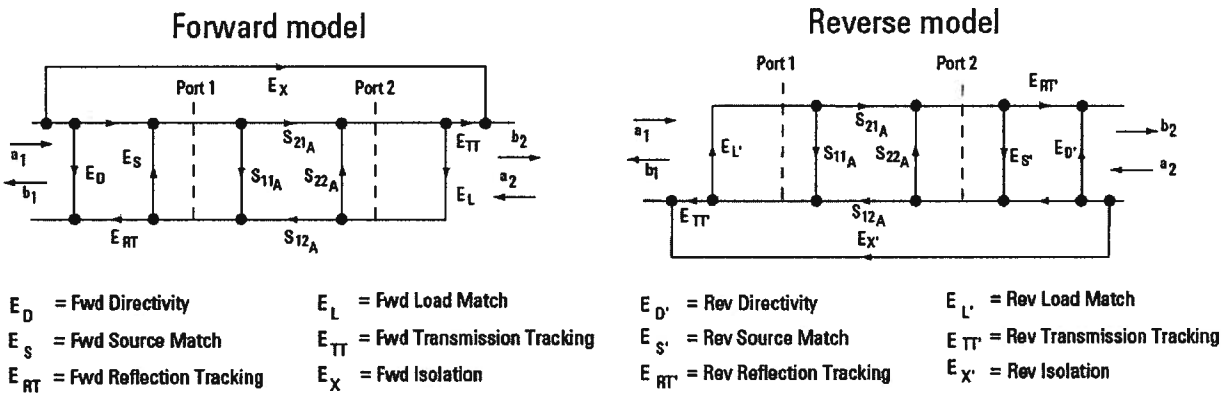

Figure A.1. Two-port error correction.

In our channel response measurements, we are interested in S_{21_A}, which, by solving the model in Figure A.1, is given by

$$S_{21_A} = \frac{\left(\frac{S_{21_M} - E_X}{E_{TT}}\right)\left(1 + \frac{S_{22_M} - E_{D'}}{E_{RT'}}(E_{S'} - E_L)\right)}{\left(1 + \frac{S_{11_M} - E_D}{E_{RT}}E_S\right)\left(1 + \frac{S_{22_M} - E_{D'}}{E_{RT'}}E_{S'}\right) - E_L E_{L'}\left(\frac{S_{21_M} - E_X}{E_{TT}}\right)\left(\frac{S_{12_M} - E_{X'}}{E_{TT'}}\right)}, \tag{F.1}$$

where '*M*' denotes the measured value. As one can see, each actual *S*-parameter is a function of all four measured *S*-parameters. This implies that (1) the VNA must sweep four times in either forward or backward directions in order to obtain the four measured *S*-parameters at each of the measurement locations, and (2) the measurement path must be bidirectional (*e.g.*, amplifiers or other unidirectional devices may not be in the measurement path).

In cases where two-port error correction is not possible, the through-line calibration can be used instead. In a through-line calibration, we apply a through-line connection between the two cables that attach to the transmitting and receiving antennas and we measure the resulting through-line response, which we call S_{TT}. Since the dominant distortions arise from the measurement cables, this approach ignores the directivity, crosstalk and load matching terms. Once measurement data has been taken, we simply apply the correction by

$$S_{21_A} = \frac{S_{21_M}}{S_{TT}}. \tag{F.2}$$

Although this approach is less accurate than the two-port error correction, the results are fairly accurate nonetheless. In Figure A.2, we show a typical PDP before and after applying the through-line calibration. Both the magnitude and phase distortions are apparent in the figure.

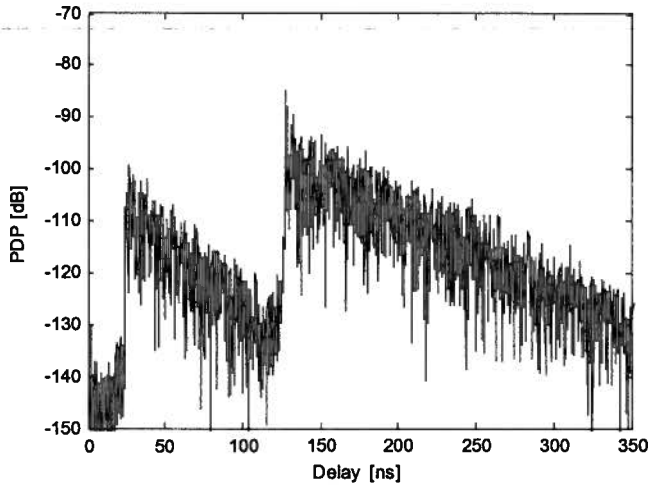

(a)

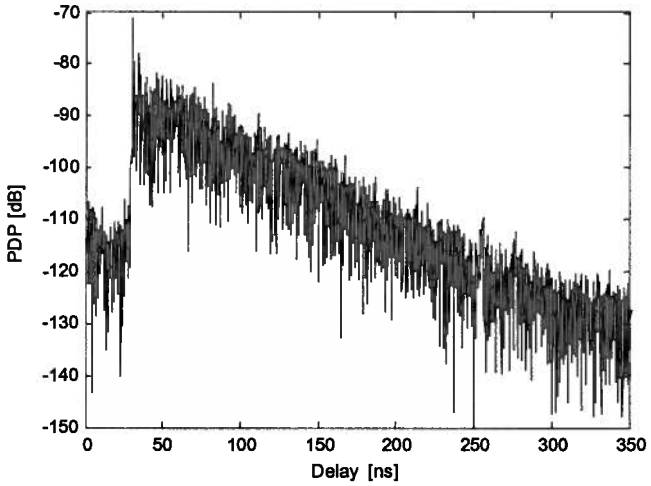

(b)

Figure A.2. A typical PDP: (a) before and (b) after through-line calibration.

Appendix B

Smearing Effect in the APDP

When we want to calculate the APDP from the PDPs in the same grid, we must first remove the propagation delay of each PDP and align them before we perform the averaging. However, because of the fine time resolution of UWB systems (in our case, $\Delta t = 133$ ps), the same specular component in one PDP may not be in the same delay in another PDP. Thus, by averaging the 49 PDPs in our grid, we would observe the impulses having a "smearing" effect. As suggested in previous literature, one way to mitigate the smearing effect is to reduce the time resolution. Here, we show that: (1) the smearing effect has minimal effect for the aircraft environment as we have such a dense scattering environment, and (2) the APDPs are similar with both the original and lowered resolution.

To reduce the time resolution, we took the complex CIR, $h(\tau)$, and we summed every ten data points before transforming $h(\tau)$ to the PDP. This way the resulting time resolution, $\Delta t'$, is 1.33 ns and the resulting PDP with lower resolution, PDP', is 10 dB above the original PDP, as shown in Figure B.1. In each of the PDPs, we see impulses that correspond to the specular components. The APDPs obtained from PDPs with original and lowered resolutions are shown in Figure B.2. The slope and intercept for the regression line for the original APDP are -0.1791 dB/ns and -28.50 dB, while those of the APDP with the lowered resolution are -0.1773 dB/ns and -17.18 dB. The standard deviation from the regression line for the original APDP is 0.841 dB, while that of the APDP with the lowered resolution is 0.682 dB. It is observed in the APDP that the impulses from specular components in each PDP have resulted in the smearing effect. However, the smearing effect is observed to be minimal given the dense scattering environment in the aircraft. We also observe that the shape of the APDP does not change. Hence, in our analysis in Chapter 3, we did not lower the resolution to mitigate the smearing effect.

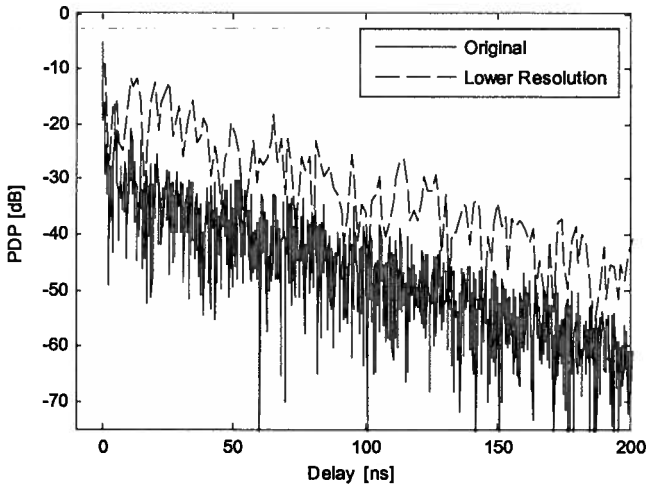

Figure B.1. Comparison of a given PDP with original and lowered resolution.

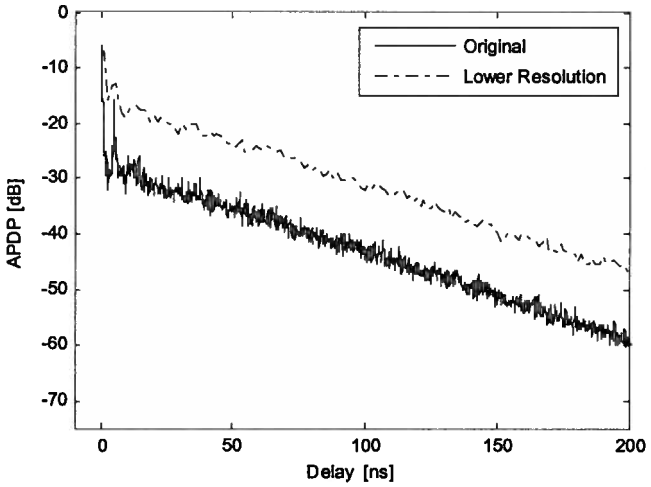

Figure B.2. Comparison of APDPs with original and lowered resolution.

Appendix C

MATLAB Code of the Modified IEEE 802.15.4a Channel Impulse Response Simulator

Below is the main script for the modified IEEE 802.15.4a channel impulse response simulator: IEEE_802_15_4a_Model.m.

```
%% Modified S-V channel model evaluation.
%% Written by Sun Xu, Kim Chee Wee, B. Kannan & Francois Chin on
%% 22/02/2005.

%% RSL release version with aircraft channels, CM 10 (LOS) and 11
(NLOS),
%% added. CM 10 corresponds to headrest configuration and 11
corresponds to
%% armrest and footrest configurations.
%%
%% Last modified by James Chuang and Simon Chiu on 05/09/2008.

clear all;
clc;

cm_num = input(['Please input channel model number:\n' ...
    '[1]  Residential LOS\n' '[2]  Residential NLOS\n' ...
    '[3]  Office LOS\n' '[4]  Office NLOS\n' '[5]  Outdoor LOS\n' ...
    '[6]  Outdoor NLOS\n' '[7]  Industrial LOS\n' ...
    '[8]  Industrial NLOS\n' '[9]  Open Outdoor NLOS\n', ...
    '[10] Aircraft LOS\n' '[11] Aircraft NLOS\n' ...
    '--------------------------> ']);
if isempty(find(cm_num == 1:11))
    error('Unrecognized channel model number!');
end
if cm_num == 11
    configuration = input(['\nPlease input configuration:\n' ...
        '[1] Armrest\n' '[2] Footrest\n' '--------------------------->
']);
    if isempty(find(configuration ~= 1:2))
        error('Unrecognized configuration!');
    end
else
    configuration = [];
end

num_channels = 100; % number of channel impulse responses to generate
no_output_files = 1; % non-zero: avoids writing output files of
continuous-time responses

randn('state',12); % initialize state of function for repeatability
rand('state',12); % initialize state of function for repeatability
```

```
%% Get channel model params based on this channel model number.
[Lam,Lmean,lambda_mode,lambda_1,lambda_2,beta,Gam,gamma_0,Kgamma, ...

sigma_cluster,nlos,gamma_rise,gamma_1,chi,m0,Km,sigma_m0,sigma_Km, ...
    sfading_mode,m0_sp,std_shdw,kappa,fc,fs] =
uwb_sv_params_15_4a( cm_num, configuration );

fprintf(1,['\nModel Parameters\n' ...
    ' Lam = %.4f, Lmean = %.4f, lambda_mode(FLAG) = %d\n' ...
    ' lambda_1 = %.4f, lambda_2 = %.4f, beta = %.4f\n' ...
    ' Gam = %.4f, gamma0 = %.4f, Kgamma = %.4f, sigma_cluster =
%.4f\n' ...
    ' nlos(FLAG) = %d, gamma_rise = %.4f, gamma_1 = %.4f, chi =
%.4f\n' ...
    ' m0 = %.4f, Km = %.4f, sigma_m0 = %.4f, sigma_Km = %.4f\n' ...
    ' sfading_mode(FLAG) = %d, m0_sp = %.4f, std_shdw = %.4f\n', ...
    ' kappa = %.4f, fc = %.4fGHz, fs = %.4fGHz\n\n'], ...
    Lam,Lmean,lambda_mode,lambda_1,lambda_2,beta,Gam,gamma_0,Kgamma,  ...

sigma_cluster,nlos,gamma_rise,gamma_1,chi,m0,Km,sigma_m0,sigma_Km,...
    sfading_mode,m0_sp,std_shdw,kappa,fc,fs);

ts = 1/fs; % sampling frequency


%% Get a bunch of realizations (impulse responses).
[h_ct,t_ct,t0,np] =
uwb_sv_model_ct_15_4a(Lam,Lmean,lambda_mode,lambda_1, ...

lambda_2,beta,Gam,gamma_0,Kgamma,sigma_cluster,nlos,gamma_rise,gamma_1,
 ...

chi,m0,Km,sigma_m0,sigma_Km,sfading_mode,m0_sp,std_shdw,num_channels,ts
,cm_num,configuration);


%% Change to complex baseband channel.
h_ct_len = size(h_ct, 1);
phi = zeros(h_ct_len, 1);

for k = 1:num_channels
    phi = rand(h_ct_len, 1).*(2*pi);
    h_ct(:,k) = h_ct(:,k) .* exp(phi .* i);
end


%% Now reduce continuous-time result to a discrete-time result.
[hN,N] = uwb_sv_cnvrt_ct_15_4a( h_ct, t_ct, np, num_channels, ts );
if N > 1,
    h = resample(hN, 1, N); % decimate the columns of hN by factor N
else
    h = hN;
end
```

```
%% Add the frequency dependency.
[h]= uwb_sv_freq_depend_ct_15_4a(h,fc,fs,num_channels,kappa);


%%
************************************************************************
%%
%% Testing and ploting
%%
************************************************************************
%%

channel_energy = sum(abs(h).^2);
h_len = length(h(:,1));
t = (0:(h_len-1))*ts; % for use in computing excess & RMS delays
excess_delay = zeros(1,num_channels);
RMS_delay = zeros(1,num_channels);
num_sig_paths = zeros(1,num_channels);
num_sig_e_paths = zeros(1,num_channels);

for k=1:num_channels
    %% Determine excess delay and RMS delay.
    sq_h = abs(h(:,k)).^2 / channel_energy(k);

    %% Apply a threshold.
    for dd = 1:length(sq_h)
        if(sq_h(dd) < max(sq_h)/10^(25/10));
            sq_h(dd) = 0;
        end
    end

    t_norm = t - t0(k); % remove the randomized arrival time of first
cluster
    excess_delay(k) = t_norm * sq_h;
    RMS_delay(k) = sqrt( ((t_norm-excess_delay(k)).^2) * sq_h );

    %% Determine number of significant paths (paths within 10 dB from
peak).
    threshold_dB = -10; % dB
    temp_h = abs(h(:,k));
    temp_thresh = 10^(threshold_dB/20) * max(temp_h);
    num_sig_paths(k) = sum(temp_h > temp_thresh);

    %% determine number of sig. paths (captures x % of energy in
channel)
    x = 0.85;
    temp_sort = sort(temp_h.^2); % sorted in ascending order of energy
    cum_energy = cumsum(temp_sort(end:-1:1)); % cumulative energy
    index_e = min(find(cum_energy >= x * cum_energy(end)));
    num_sig_e_paths(k) = index_e;
end

energy_mean = mean(10*log10(channel_energy));
energy_stddev = std(10*log10(channel_energy));
mean_excess_delay = mean(excess_delay);
```

```
mean_RMS_delay = mean(RMS_delay);
mean_sig_paths = mean(num_sig_paths);
mean_sig_e_paths = mean(num_sig_e_paths);

fprintf(1,'Model Characteristics\n');
fprintf(1,' Mean delays: excess (tau_m) = %.1f ns, RMS (tau_rms) =
%1.f\n', ...
    mean_excess_delay, mean_RMS_delay);
fprintf(1,' # paths: NP_10dB = %.1f, NP_85%% = %.1f\n', ...
    mean_sig_paths, mean_sig_e_paths);
fprintf(1,' Channel energy: mean = %.1f dB, std deviation = %.1f
dB\n', ...
    energy_mean, energy_stddev);

figure(1);
clf;
plot(t, abs(h)); grid on
title('Impulse Response Realization');
xlabel('Time [ns]');

figure(2);
clf;
plot((1:num_channels), excess_delay, 'b-', [1 num_channels],
mean_excess_delay*[1 1], 'r-');
grid on
title('Excess delay [ns]');
xlabel('Channel number');

figure(3);
clf;
plot((1:num_channels), RMS_delay, 'b-', [1 num_channels],
mean_RMS_delay*[1 1], 'r-');
grid on
title('RMS delay [ns]');
xlabel('Channel number');

figure(4);
clf;
plot((1:num_channels), num_sig_paths, 'b-', [1 num_channels],
mean_sig_paths*[1 1], 'r-');
grid on
title('Number of significant paths within 10 dB of peak');
xlabel('Channel number');

figure(5);
clf;
plot((1:num_channels), num_sig_e_paths, 'b-', [1 num_channels],
mean_sig_e_paths*[1 1], 'r-');
grid on
title('Number of significant paths capturing > 85% energy');
xlabel('Channel number');

temp_average_power = sum((abs(h))'.*(abs(h))', 1)/num_channels;
temp_average_power = temp_average_power/max(temp_average_power);
average_decay_profile_dB = 10*log10(temp_average_power);
threshold_dB = -60;
```

```
above_threshold = find(average_decay_profile_dB > threshold_dB);
ave_t = t(above_threshold);
apdf_dB = average_decay_profile_dB(above_threshold);

figure(6); clf; plot(ave_t, apdf_dB); grid on;
title('Average Power Decay Profile');
xlabel('Delay (nsec)');
ylabel('Average power (dB)');

figure(7); clf;
plot(ave_t, 10*log10((10.^(apdf_dB/10))/sum(10.^(apdf_dB/10)))); grid
on;
title('Normalized Average Power Decay Profile');
xlabel('Delay (nsec)');
ylabel('Amplitude (dB)');
axis([-10 200 -60 0]);

% figure(8); clf;
% for i = 1:num_channels
%     plot(t, 10*log10(abs(h(:,i)).^2./sum(abs(h(:,i)).^2))); grid on;
%     title(['PDP #: ', num2str(i)]);
%     xlabel('Time [ns]');
%     axis([-10 200 -60 0]);
%     pause;
% end

if no_output_files,
    return
end


%%
%%************************************************************************
%%
%% Savinge the data
%%
%%************************************************************************
%%

%% Save continuous-time (time,value) pairs to files.
save_fn = sprintf('cm%d_imr', cm_num);

%% A complete self-contained file for Matlab users
save([save_fn '.mat'], 't', 'h','t_ct', 'h_ct', 't0', 'np',
'num_channels', 'cm_num');

%% Three comma-delimited text files for non-Matlab users:
%% File #1: cmX_imr_np.csv lists the number of paths in each
realization
dlmwrite([save_fn '_np.csv'], np, ','); % number of paths

%% File #2: cmX_imr_ct.csv can open with Excel
%% n'th pair of columns contains the (time,value) pairs for the n'th
realization
%% save continous time data
th_ct = zeros(size(t_ct,1),3*size(t_ct,2));
```

```
th_ct(:,1:3:end) = t_ct; % time
th_ct(:,2:3:end) = abs(h_ct); % magnitude
th_ct(:,3:3:end) = angle(h_ct); % phase (radians)

fid = fopen([save_fn '_ct.csv'], 'w');
if fid < 0,
    error('unable to write .csv file for impulse response, file may be
open in another application');
end

for k = 1:size(th_ct,1)
    fprintf(fid,'%.4f,%.6f,', th_ct(k,1:end-2));
    fprintf(fid,'%.4f,%.6f\r\n', th_ct(k,end-1:end)); % \r\n for
Windoze end-of-line
end
fclose(fid);

%% File #3: cmX_imr_dt.csv can open with Excel
%% discrete channel impulse response magnitude and phase pair
realization.
%% the first column is time. phase is in radians
%% save discrete time data
th = zeros(size(h,1),2*size(h,2)+1);
th(:,1) = t'; % the first column is time scale
th(:,2:2:end) = abs(h); % even columns are magnitude
th(:,3:2:end) = angle(h); % odd columns are phase

fid = fopen([save_fn '_dt.csv'], 'w');
if fid < 0,
    error('unable to write .csv file for impulse response, file may be
open in another application');
end

for k = 1:size(th,1)
    fprintf(fid,'%.4f,%.6f,', th(k,1:end-2));
    fprintf(fid,'%.4f,%.6f\r\n', th(k,end-1:end)); % \r\n for Windoze
end-of-line
end
fclose(fid);

return; % end of program
```

Below is one of the four subscripts for the modified IEEE 802.15.4a channel impulse response simulator: uwb_sv_cnvrt_ct_15_4a.m.

```
%% convert continuous-time channel model h_ct to N-times oversampled
discrete-time samples
%% h_ct, t, np, and num_channels are as specified in uwb_sv_model
%% ts is the desired time resolution
%% hN will be produced with time resolution ts / N.
%% It is up to the user to then apply any filtering and/or complex
downconversion and then
%% decimate by N to finally obtain an impulse response at time
resolution
%% ts.

function [hN,N] = uwb_sv_cnvrt_ct_15_4a( h_ct, t, np, num_channels, ts )

min_Nfs = 100; % GHz
N = max( 1, ceil(min_Nfs*ts) ); % N*fs = N/ts is the intermediate
sampling frequency before decimation
N = 2^nextpow2(N); % make N a power of 2 to facilitate efficient multi-
stage decimation
Nfs = N / ts;
t_max = max(t(:)); % maximum time value across all channels
h_len = 1 + floor(t_max * Nfs); % number of time samples at resolution
ts / N
hN = zeros(h_len,num_channels);
for k = 1:num_channels
    np_k = np(k); % number of paths in this channel
    t_Nfs = 1 + floor(t(1:np_k,k) * Nfs); % vector of quantized time
indices for this channel
    for n = 1:np_k
        hN(t_Nfs(n),k) = hN(t_Nfs(n),k) + h_ct(n,k);
    end
end
```

Below is one of the four subscripts for the modified IEEE 802.15.4a channel impulse response simulator: uwb_sv_freq_depend_ct_15_4a.m.

```
%% This function is used to include the frequency dependency.

function [h]= uwb_sv_freq_depend_ct_15_4a(h,fc,fs,num_channels,kappa)

f0 = 5; % GHz
h_len = length(h(:,1));
f = [fc-fs/2 : fs/h_len/2 : fc+fs/2]./f0;
f = f.^(-2*(kappa));
f = [f(h_len : 2*h_len), f(1 : h_len-1)]';
i = (-1)^(1/2); % complex i
for c = 1:num_channels
    % add the frequency dependency
    h2 = zeros(2*h_len, 1);
    h2(1 : h_len) = h(:,c); % zero padding
    fh2 = fft(h2);
    fh2 = fh2 .* f;
    h2 = ifft(fh2);
    h(:,c) = h2(1:h_len);
    % Normalize the channel energy to 1
    h(:,c) = h(:,c)/sqrt(h(:,c)' * h(:,c) );
end
return
```

Below is one of the four subscripts for the modified IEEE 802.15.4a channel impulse response simulator: uwb_sv_model_ct_15_4a.m.

```
%% Written by Sun Xu, Kim Chee Wee, B. Kannan & Francois Chin on
22/02/2005
%% IEEE 802.15.4a UWB channel model for PHY proposal evaluation
%% continuous-time realization of modified S-V channel model
%%
%% Input parameters:
%%
%% detailed introduction of input parameters is at uwb_sv_params.m
%% num_channels number of random realizations to generate
%%
%% Outputs
%%
%% h is returned as a matrix with num_channels columns, each column
%% holding a random realization of the channel model (an impulse
response)
%% t is organized as h, but holds the time instances (in nsec) of the
paths whose
%% signed amplitudes are stored in h
%% t0 is the arrival time of the first cluster for each realization
%% np is the number of paths for each realization.
%% Thus, the k'th realization of the channel impulse response is the
sequence
%% of (time,value) pairs given by (t(1:np(k),k), h(1:np(k),k))
%%
%% modified by I2R


function [h,t,t0,np] =
uwb_sv_model_ct_15_4a(Lam,Lmean,lambda_mode,lambda_1, ...

lambda_2,beta,Gam,gamma_0,Kgamma,sigma_cluster,nlos,gamma_rise,gamma_1,
 ...

chi,m0,Km,sigma_m0,sigma_Km,sfading_mode,m0_sp,std_shdw,num_channels,ts
,cm_num,configuration)


%% Initialize and precompute some things.
std_L = 1/sqrt(2*Lam); % std dev (nsec) of cluster arrival spacing
std_lam_1 = 1/sqrt(2*lambda_1);
std_lam_2 = 1/sqrt(2*lambda_2);
% std_lam = 1/sqrt(2*lambda); % std dev (nsec) of ray arrival spacing
h_len = 1000; % there must be a better estimate of # of paths than this
ngrow = 1000; % amount to grow data structure if more paths are needed
h = zeros(h_len,num_channels);
t = zeros(h_len,num_channels);
t0 = zeros(1,num_channels);
np = zeros(1,num_channels);


%% Randomly create distances from 2 to 13m.
if(cm_num == 10 || cm_num == 11)
```

```
    d = rand(1, num_channels)*11 + 2;
%     d(1:num_channels) = 13.2; % for verification
end


%% Main loop.
for k = 1:num_channels % loop over number of channels

    % Code for aircraft channels
    if cm_num == 10
        gamma_1 = 15.19 + 10*1.25*log10(d(k)) + 0.83*randn;
        m0 = 0.317 + 10*0.0278*log10(d(k)) + 0.0014*randn;
        m0_sp = 24.25 - 10*0.35*log10(d(k)) + 1.29*randn;
    elseif cm_num == 11
        chi = 1; gamma_rise = -1; gamma_1 = -1;
        if configuration == 1
            while chi >= 1
                chi = abs(-0.2389 + 10*0.1066*log10(d(k)) +
0.1219*randn);
            end
            while gamma_rise <= 0
                gamma_rise = abs(-11.62 + 10*3.2404*log10(d(k)) +
3.8144*randn);
            end
            while gamma_1 <= 0
                gamma_1 = abs(15.31 + 10*1.2249*log10(d(k)) +
0.5368*randn);
            end
            m0 = 0.109 + 10*0.0460*log10(d(k)) + 0.0431*randn;
        else
            while chi >= 1
                chi = 0.5992 + 10*0.0266*log10(d(k)) + 0.0250*randn;
            end
            while gamma_rise <= 0
                gamma_rise = -30.10 + 10*8.1474*log10(d(k)) +
6.3099*randn;
            end
            while gamma_1 <= 0
                gamma_1 = 17.77 + 10*0.8615*log10(d(k)) + 0.5505*randn;
            end
            m0 = 0.294 + 10*0.0378*log10(d(k)) + 0.0998*randn;
        end
    end

    tmp_h = zeros(size(h,1),1);
    tmp_t = zeros(size(h,1),1);
    if nlos == 1,
        Tc = (std_L*randn)^2 + (std_L*randn)^2; % First cluster random
arrival
    else
        Tc = 0; % First cluster arrival occurs at time 0
    end
    t0(k) = Tc;
    if nlos == 2 & lambda_mode == 2
        L = 1; % for industrial NLOS environment
    else
        L = max(1, poissrnd(Lmean)); % number of clusters
```

```
    end
    %%%%%%%%%%%%%%%%%%%%%%%%%%%%%%%%%%%%%%%%%%%%%%%%%%%%
    if Kgamma ~= 0 & nlos == 0
        Tcval = []; Tc_cluster= [];
        Tc_cluster(1,1)=Tc;
        for i_Tc=2:L+1
            Tc_cluster(1,i_Tc)= Tc_cluster(1,i_Tc-1)+(std_L*randn)^2 +
(std_L*randn)^2;
        end
    end
    %%%%%%%%%%%%%%%%%%%%%%%%%%%%%%%%%%%%%%%%%%%%%%%%%%%%
    cluster_index = zeros(1,L);
    path_ix = 0;
    nak_m = [];
    for ncluster = 1:L
        % Determine Ray arrivals for each cluster
        Tr = 0; % first ray arrival defined to be time 0 relative to
cluster
        cluster_index(ncluster) = path_ix+1; % remember the cluster
location
        gamma = Kgamma*Tc + gamma_0; % delay dependent cluster decay
time
        if nlos == 2 & ncluster == 1
            gamma = gamma_1;
        end
        Mcluster = sigma_cluster*randn;
        Pcluster = 10*log10(exp(-1*Tc/Gam))+Mcluster; % total cluster
power
        Pcluster = 10^(Pcluster*0.1);
        %%%%%%%%%%%%%%%%%%%%%%%%%%%%%%%%%%%%%%%%%%%%%%%%%%%%
        if Kgamma ~= 0 & nlos == 0
            Tr_len=Tc_cluster(1,ncluster+1)-Tc_cluster(1,ncluster);
        else
            Tr_len = 10*gamma;
        end
        %%%%%%%%%%%%%%%%%%%%%%%%%%%%%%%%%%%%%%%%%%%%%%%%%%%%
        while (Tr < Tr_len),
            t_val = (Tc+Tr); % time of arrival of this ray
            if nlos == 2 & ncluster == 1
                if cm_num == 10
                    h_val = Pcluster*exp(-Tr/gamma_1);
                else
                    h_val = Pcluster*(1-chi*exp(-Tr/gamma_rise))*exp(-
Tr/gamma_1) ...
                        *(gamma+gamma_rise)/gamma/(gamma+gamma_rise*(1-
chi));
                end
            else
                % equation (19)
                h_val = Pcluster/gamma*exp(-
Tr/gamma)/(beta*lambda_1+(1-beta)*lambda_2+1);
            end
            path_ix = path_ix + 1; % row index of this ray
            if path_ix > h_len,
                % grow the output structures to handle more paths as
needed
                tmp_h = [tmp_h; zeros(ngrow,1)];
                tmp_t = [tmp_t; zeros(ngrow,1)];
```

```
                h = [h; zeros(ngrow,num_channels)];
                t = [t; zeros(ngrow,num_channels)];
                h_len = h_len + ngrow;
            end
            tmp_h(path_ix) = h_val;
            tmp_t(path_ix) = t_val;
            % if lambda_mode == 0
            % Tr = Tr + (std_lam*randn)^2 + (std_lam*randn)^2;
            if lambda_mode == 1
                if rand < beta
                    Tr = Tr + (std_lam_1*randn)^2 + (std_lam_1*randn)^2;
                else
                    Tr = Tr + (std_lam_2*randn)^2 + (std_lam_2*randn)^2;
                end
            elseif lambda_mode == 2
                Tr = Tr + ts;
            else
                error('lambda mode is wrong!')
            end
            % generate log-normal distributed nakagami m-factor
            m_mu = m0 - Km*t_val;
            m_std = sigma_m0 - sigma_Km*t_val;
            nak_m = [nak_m, lognrnd(m_mu, m_std)];
        end
        Tc = Tc + (std_L*randn)^2 + (std_L*randn)^2;
        %%%%%%%%%%%%%%%%%%%%%%%%%%%%%%%%%%%%%%%%%%%%%%%%
        if Kgamma ~= 0 & nlos == 0
            Tc = Tc_cluster(1,ncluster+1);
        end
        %%%%%%%%%%%%%%%%%%%%%%%%%%%%%%%%%%%%%%%%%%%%%%%%
    end

    % Aircraft code
    if(cm_num == 10)
        Kr = 17.47 - 10*(0.36)*log10(d(k)) + 1.34*randn;
        Kr = 10^(Kr/10);
        tmp_h(1) = tmp_h(1)*Kr; % h stays in power units until Nakagami
distribution is applied.
    end

    % change m value of the first multipath to be the deterministic
value
    if sfading_mode == 1
        nak_m(cluster_index(1)) = m0_sp;
    elseif sfading_mode == 2
        nak_ms(cluster_index) = m0_sp;
    end

    % apply nakagami
    for path = 1:path_ix
        h_val = (gamrnd(nak_m(path), tmp_h(path)/nak_m(path))).^(1/2);
        tmp_h(path) = h_val;
    end
    np(k) = path_ix; % number of rays (or paths) for this realization
    [sort_tmp_t,sort_ix] = sort(tmp_t(1:np(k))); % sort in ascending
time order
    t(1:np(k),k) = sort_tmp_t;
```

```
    h(1:np(k),k) = tmp_h(sort_ix(1:np(k)));
    % now impose a log-normal shadowing on this realization
    % fac = 10^(std_shdw*randn/20) / sqrt( h(1:np(k),k)' *
h(1:np(k),k) );
    % h(1:np(k),k) = h(1:np(k),k) * fac;
end

return
```

Below is one of the four subscripts for the modified IEEE 802.15.4a channel impulse response simulator: uwb_sv_params_15_4a.m.

```
%% Written by Sun Xu, Kim Chee Wee, B. Kannan & Francois Chin on
22/02/2004
%% Return modified S-V model parameters for standard UWB channel models
%% ------------------------------
%% Lam Cluster arrival rate (clusters per nsec)
%% Lmean Mean number of Clusters
%% lambda_mode Flag for Mixture of poission processes for ray arrival
times
%% 1 -> Mixture of poission processes for the ray arrival times
%% 2 -> tapped delay line model
%% lambda_1 Ray arrival rate for Mixture of poisson processes (rays per
nsec)
%% lambda_2 Ray arrival rate for Mixture of poisson processes (rays per
nsec)
%% beta Mixture probability
%% ------------------------------
%% Gam Cluster decay factor (time constant, nsec)
%% gamma0 Ray decay factor (time constant, nsec)
%% Kgamma Time dependence of ray decay factor
%% sigma_cluster Standard deviation of normally distributed variable
for cluster energy
%% nlos Flag for non line of sight channel
%% 0 -> LOS
%% 1 -> NLOS with first arrival path starting at t ~= 0
%% 2 -> NLOS with first arrival path starting at t = 0 and diffused
first cluster
%% gamma_rise Ray decay factor of diffused first cluster (time constant,
nsec)
%% gamma_1 Ray decay factor of diffused first cluster (time constant,
nsec)
%% chi Diffuse weight of diffused first cluster
%% ------------------------------
%% m0 Mean of log-normal distributed nakagami-m factor
%% Km Time dependence of m0
%% sigma_m0 Standard deviation of log-normal distributed nakagami-m
factor
%% sigma_Km Time dependence of sigma_m0
%% sfading_mode Flag for small-scale fading
%% 0 -> All paths have same m-factor distribution
%% 1 -> LOS first path has a deterministic large m-factor
%% 2 -> LOS first path of each cluster has a deterministic
%% large m-factor
%% m0_sp Deterministic large m-factor
%% ------------------------------
%% std_shdw Standard deviation of log-normal shadowing of entire
impulse response
%% ------------------------------
%% kappa Frequency dependency of the channel
%% ------------------------------
%% fc Center Frequency
%% fs Frequency Range
%%
%% modified by I2R
```

```
function
[Lam,Lmean,lambda_mode,lambda_1,lambda_2,beta,Gam,gamma_0,Kgamma, ...

sigma_cluster,nlos,gamma_rise,gamma_1,chi,m0,Km,sigma_m0,sigma_Km, ...
    sfading_mode,m0_sp,std_shdw,kappa,fc,fs] =
uwb_sv_params_15_4a( cm_num, configuration )

if cm_num == 1, % Residential LOS
    % MPC arrival
    Lam = 0.047; Lmean = 3;
    lambda_mode = 1;
    lambda_1 = 1.54; lambda_2 = 0.15; beta = 0.095;
    %MPC decay
    Gam = 22.61; gamma_0 = 12.53; Kgamma = 0; sigma_cluster = 2.75;
    nlos = 0;
    gamma_rise = NaN; gamma_1 = NaN; chi = NaN; % dummy in this
scenario
    % Small-scale Fading
    m0 = 0.67; Km = 0; sigma_m0 = 0.28; sigma_Km = 0;
    sfading_mode = 0; m0_sp = NaN;
    % Large-scale Fading - Shadowing
    std_shdw = 2.22;
    % Frequency Dependence
    kappa = 1.12;
    fc = 6; % GHz
    fs = 8; % 2 - 10 GHz

elseif cm_num == 2, % Residential NLOS
    % MPC arrival
    Lam = 0.12; Lmean = 3.5;
    lambda_mode = 1;
    lambda_1 = 1.77; lambda_2 = 0.15; beta = 0.045;
    %MPC decay
    Gam = 26.27; gamma_0 = 17.5; Kgamma = 0; sigma_cluster = 2.93;
    nlos = 1;
    gamma_rise = NaN; gamma_1 = NaN; chi = NaN; % dummy in this
scenario
    % Small-scale Fading
    m0 = 0.69; Km = 0; sigma_m0 = 0.32; sigma_Km = 0;
    sfading_mode = 0; m0_sp = NaN;
    % Large-scale Fading - Shadowing
    std_shdw = 3.51;
    % Frequency Dependence
    kappa = 1.53;
    fc = 6; % GHz
    fs = 8; % 2 - 10 GHz

elseif cm_num == 3, % Office LOS
    % MPC arrival
    Lam = 0.016; Lmean = 5.4;
    lambda_mode = 1;
    lambda_1 = 0.19; lambda_2 = 2.97; beta = 0.0184;
    %MPC decay
    Gam = 14.6; gamma_0 = 6.4; Kgamma = 0; sigma_cluster = 3; %
assumption
    nlos = 0;
```

```
    gamma_rise = NaN; gamma_1 = NaN; chi = NaN; % dummy in this
scenario
    % Small-scale Fading
    m0 = 0.42; Km = 0; sigma_m0 = 0.31; sigma_Km = 0;
    sfading_mode = 2; m0_sp = 3; % assumption
    % Large-scale Fading - Shadowing
    std_shdw = 0; %1.9;
    % Frequency Dependence
    kappa = 0.03;
    fc = 6; % GHz
    fs = 8; % 3 - 6 GHz

elseif cm_num == 4, % Office NLOS
    % MPC arrival
    Lam = 0.19; Lmean = 3.1;
    lambda_mode = 1;
    lambda_1 = 0.11; lambda_2 = 2.09; beta = 0.0096;
    %MPC decay
    Gam = 19.8; gamma_0 = 11.2; Kgamma = 0; sigma_cluster = 3; %
assumption
    nlos = 2;
    gamma_rise = 15.21; gamma_1 = 11.84; chi = 0.78;
    % Small-scale Fading
    m0 = 0.5; Km = 0; sigma_m0 = 0.25; sigma_Km = 0;
    sfading_mode = 0; m0_sp = NaN; % assumption
    % Large-scale Fading - Shadowing
    std_shdw = 3.9;
    % Frequency Dependence
    kappa =0.71;
    fc = 6; % GHz
    fs = 8; % 3 - 6 GHz

elseif cm_num == 5, % Outdoor LOS
    % MPC arrival
    Lam = 0.0448; Lmean = 13.6;
    lambda_mode = 1;
    lambda_1 = 0.13; lambda_2 = 2.41; beta = 0.0078;
    %MPC decay
    Gam = 31.7; gamma_0 = 3.7; Kgamma = 0; sigma_cluster = 3; %
assumption
    nlos = 0;
    gamma_rise = NaN; gamma_1 = NaN; chi = NaN; % dummy in this
scenario
    % Small-scale Fading
    m0 = 0.77; Km = 0; sigma_m0 = 0.78; sigma_Km = 0;
    sfading_mode = 2; m0_sp = 3; % assumption
    % Large-scale Fading - Shadowing
    std_shdw = 0.83;
    % Frequency Dependence
    kappa = 0.12;
    fc = 6; % GHz
    fs = 8; % 3 - 6 GHz

elseif cm_num == 6, % Outdoor NLOS
    % MPC arrival
    Lam = 0.0243; Lmean = 10.5;
    lambda_mode = 1;
```

```
    lambda_1 = 0.15; lambda_2 = 1.13; beta = 0.062;
    %MPC decay
    Gam = 104.7; gamma_0 = 9.3; Kgamma = 0; sigma_cluster = 3; %
assumption
    nlos = 1;
    gamma_rise = NaN; gamma_1 = NaN; chi = NaN; % dummy in this
scenario
    % Small-scale Fading
    m0 = 0.56; Km = 0; sigma_m0 = 0.25; sigma_Km = 0;
    sfading_mode = 0; m0_sp = NaN; % assumption
    % Large-scale Fading - Shadowing
    std_shdw = 2; % assumption
    % Frequency Dependence
    kappa = 0.13;
    fc =6; % GHz
    fs = 8; % 3 - 6 GHz

elseif cm_num == 7, % Industrial LOS
    % MPC arrival
    Lam = 0.0709; Lmean = 4.75;
    lambda_mode = 2;
    lambda_1 = 1; lambda_2 = 1; beta = 1; % dummy in this scenario
    %MPC decay
    Gam = 13.47; gamma_0 = 0.615; Kgamma = 0.926; sigma_cluster = 4.32;
    nlos = 0;
    gamma_rise = NaN; gamma_1 = NaN; chi = NaN; % dummy in this
scenario
    % Small-scale Fading
    m0 = 0.36; Km = 0; sigma_m0 = 1.13; sigma_Km = 0;
    sfading_mode = 1; m0_sp = 12.99;
    % Large-scale Fading - Shadowing
    std_shdw = 6;
    % Frequency Dependence
    kappa = -1.103;
    fc = 6; % GHz
    fs = 8; % 2 - 8 GHz

elseif cm_num == 8, % Industrial NLOS
    % MPC arrival
    Lam = 0.089; Lmean = 1;
    lambda_mode = 2;
    lambda_1 = 1; lambda_2 = 1; beta = 1; % dummy in this scenario
    %MPC decay
    Gam = 5.83; gamma_0 = 0.3; Kgamma = 0.44; sigma_cluster = 2.88;
    nlos = 2;
    gamma_rise = 47.23; gamma_1 = 84.15; chi = 0.99;
    % Small-scale Fading
    m0 = 0.3; Km = 0; sigma_m0 = 1.15; sigma_Km = 0;
    sfading_mode = 0; m0_sp = NaN; % m0_sp is assumption
    % Large-scale Fading - Shadowing
    std_shdw = 6;
    % Frequency Dependence
    kappa = -1.427;
    fc = 6; % GHz
    fs = 8; % 2 - 8 GHz
```

```
elseif cm_num == 9, % Open Outdoor Environment NLOS (Fram, Snow-Covered
Open Area)
    % MPC arrival
    Lam = 0.0305; Lmean = 3.31;
    lambda_mode = 1;
    lambda_1 = 0.0225; lambda_2 = 1; beta = 1;
    %MPC decay
    Gam = 56; gamma_0 = 0.92; Kgamma = 0; sigma_cluster = 3; %
sigma_cluster is assumption
    nlos = 1;
    gamma_rise = NaN; gamma_1 = NaN; chi = NaN;
    % Small-scale Fading
    m0 = 4.1; Km = 0; sigma_m0 = 2.5; sigma_Km = 0;
    sfading_mode = 0; m0_sp = NaN; % m0_sp is assumption
    % Large-scale Fading - Shadowing
    std_shdw = 3.96;
    % Frequency Dependence
    kappa = -1; % Kappa is assumption
    fc = 6; % GHz
    fs = 8; % 2 - 8 GHz

elseif cm_num == 10, % Aircraft headrest (LOS)
    % MPC arrival
    Lam = 0.089; Lmean = 1;
    lambda_mode = 2;
    lambda_1 = 1; lambda_2 = 1; beta = 1; % dummy in this scenario
    %MPC decay
    Gam = 5.83; gamma_0 = 0.3; Kgamma = 0.44; sigma_cluster = 0;
    nlos = 2;
    gamma_rise = 0; gamma_1 = 0; chi = 0;
    % Small-scale Fading
    m0 = []; Km = 0; sigma_m0 = -5.33; sigma_Km = 0;
    sfading_mode = 1; m0_sp = 0;
    % Large-scale Fading - Shadowing
    std_shdw = 6;
    % Frequency Dependence
    kappa = 0.25;
    fc = 6; % GHz
    fs = 8; % 2 - 8 GHz

elseif cm_num == 11, % Aircraft armrest and footrest (NLOS a and b)
    % MPC arrival
    Lam = 0.089; Lmean = 1;
    lambda_mode = 2;
    lambda_1 = 1; lambda_2 = 1; beta = 1; % dummy in this scenario
    %MPC decay
    Gam = 5.83; gamma_0 = 0.3; Kgamma = 0.44; sigma_cluster = 0;
    nlos = 2;
    gamma_rise = 0; gamma_1 = 0; chi = 0; % generated with distance
dependence in uwb_sv_model_ct_15_4a.m

    if configuration == 1
        % Small-scale Fading
        m0 = 0; Km = 0; sigma_m0 = -5.30; sigma_Km = 0;
        sfading_mode = 0; m0_sp = 0;
        % Large-scale Fading - Shadowing
        std_shdw = 6;
```

```
        % Frequency Dependence
        kappa = 0.59;
    elseif configuration == 2
        % Small-scale Fading
        m0 = 0; Km = 0; sigma_m0 = -5.21; sigma_Km = 0;
        sfading_mode = 0; m0_sp = 0;
        % Large-scale Fading - Shadowing
        std_shdw = 6;
        % Frequency Dependence
        kappa = 0.79;
    end

    fc = 6; % GHz
    fs = 8; % 2 - 8 GHz
else
    error('cm_num is wrong!!')
end

return
```